

2013

Interactions of Organic and Biomolecules with Solid Surfaces Probed by Atomic Force Microscopy

Kyle Wagner
Lehigh University

Follow this and additional works at: <http://preserve.lehigh.edu/etd>

 Part of the [Chemistry Commons](#)

Recommended Citation

Wagner, Kyle, "Interactions of Organic and Biomolecules with Solid Surfaces Probed by Atomic Force Microscopy" (2013). *Theses and Dissertations*. Paper 1659.

This Dissertation is brought to you for free and open access by Lehigh Preserve. It has been accepted for inclusion in Theses and Dissertations by an authorized administrator of Lehigh Preserve. For more information, please contact preserve@lehigh.edu.

**Interactions of Organic and Biomolecules with Solid Surfaces Probed
by Atomic Force Microscopy**

by

Kyle Wagner

A Dissertation
Presented to the Graduate and Research Committee
of Lehigh University
in Candidacy for the Degree of
Doctor of Philosophy

in
Chemistry

Lehigh University
May 2013

Copyright by Kyle Wagner

May 2013

Approved and recommended for acceptance as a dissertation in partial fulfillment of the requirements for the degree of Doctor of Philosophy in Chemistry.

“Interactions of Organic and Biomolecules with Solid Surfaces probed by Atomic Force Microscopy”

Kyle Wagner

Date

Dmitri Vezenov
Dissertation Advisor

Accepted Date

David Moore
Committee Member

Jim Roberts
Committee Member

Anand Jagota
Committee Member

Table of Contents

List of Figures	vii
List of Tables	xiii
Abstract	1
Chapter 1 Introduction to Force Spectroscopy and Properties of Carbon Nanotubes and DNA	3
1.1 Synopsis	3
1.2 Force Spectroscopy	4
1.3 Force Calibration	9
1.4 Dynamic Force Experiments.....	10
1.5 Friction Force Microscopy and Contact Mechanics Models	16
1.6 Introduction to DNA Structure and Modeling	22
1.7 Introduction to the Structure and Properties of Carbon Nanotubes	26
1.8 Scope of the Dissertation	29
Chapter 2 Noncontact Method for Calibration of Lateral Forces in Scanning Force Microscopy	32
2.1 Introduction.....	32
2.2 Approach.....	34
2.3 Methods.....	40
2.4 Results and Discussion	43
2.4.1 Noncontact Calibration of the Normal Cantilever Sensitivity	46
2.4.2 Noncontact Calibration of the Normal Cantilever Sensitivity in Liquids	49
2.4.3 Noncontact Calibration of the Normal Cantilever Sensitivity at Elevated Temperature	52
2.4.4 Noncontact Calibration of the Lateral Cantilever Sensitivity.....	53
2.4.5 Noncontact Calibration of the Lateral Cantilever Sensitivity in Liquids	56
2.4.6 Noncontact Calibration of the Lateral Cantilever Sensitivity at Elevated Temperature	58
2.5 Conclusions.....	58
2.6 Appendix.....	60
2.6.1 Thermal Spectrum Baseline Instrumental Noise	60
2.6.2. Example Calculation for Wedge Calibration Method	61
2.6.3 Calculation of the Cantilever Thickness from the Natural Frequency	64
2.6.4. Lateral sensitivity measured using stiction portion of friction loops	65

Chapter 3 Yield Strength of Glued Langmuir-Blodgett Films Determined by Friction Force Microscopy **67**

3.1. Introduction.....	67
3.2. Methods.....	71
3.2.1 Preparation of LB Films.....	71
3.2.2 Film Thickness Measurements by Ellipsometry.....	73
3.2.3 Film Yield Strength Determination Using Force Spectroscopy	73
3.2.4 Force Calibration	74
3.2.5 Determination of the Tip Radius.....	75
3.3. Results and Discussion	75
3.3.1 Choosing Experimental Conditions for AFM Scratch Tests	75
3.3.2 Friction <i>versus</i> Load Experiments on LB Bilayer Films	77
3.3.3 Measurement of Yield Strength of LB Films	84
3.4. Conclusions.....	91
3.5 Appendix.....	92
3.5.1. Set Point Ramping Code.....	92
3.5.2. Surface Roughness.....	92
3.5.3. Measurement of the Tip Radius.....	93
3.5.4. Determination of the Tabor Parameter	94
3.5.5. Pseudo 2-D Height Images of Film Damage	96
3.5.6. Film Indentation Curves.	97
3.5.7 Nanolithography Experiments	97

Chapter 4 Peeling Single Stranded DNA from Graphite to Model Interactions between DNA and Carbon Nanotubes **100**

4.1 Introduction.....	100
4.2 Methods.....	102
4.2.1 Materials	102
4.2.2 Probe Functionalization	103
4.2.3 Monolayer Preparation.....	104
4.2.4 Force Calibration and Force Curve Capture	104
4.3 Results and Discussion	106
4.3.1 Equilibrium Peeling Model.....	106
4.3.2 DNA Chain Length and Directional Effects on Peeling.....	110
4.3.3 The Contribution of Hydrophobic Interactions to Peeling Forces.	111
4.3.4 Interaction Strength of Purines on Graphite	113
4.4 Conclusions.....	117
4.5 Appendix.....	119
4.5.1 Correlation between binding free energy per base and non-polar molecular area.	119
4.5.2 Stretching Behavior of poly(dG)	120

Chapter 5 Measuring the Interaction Strength of DNA Oligomers on Suspended Carbon Nanotubes – A Comparison to 2D Substrates	121
5.1 Introduction.....	121
5.2 Methods.....	125
5.2.1 Probe Functionalization	125
5.2.2 Force Calibration and Force Curve Capture	126
5.2.3. Preparation of Acid Modified Carbon Nanotubes	127
5.2.4. Substrate Preparation	128
5.3 Results and Discussion	130
5.3.1. Preparation of Suspended CNT Substrate.....	130
5.3.2. Oligomer Peeling on Suspended Tubes	133
5.4 Conclusions.....	142
5.5 Appendix.....	143
5.5.1 Measurement of Slack in Suspended CNTs.....	143
References	145
Curriculum Vitae	156

List of Figures

- Figure 1.1.** Scanning electron micrographs of a typical contact mode AFM probe. (a) Image showing the bottom surface of the cantilever. The bright spot at the end of the cantilever is the tip (shown from the side in (b)). 6
- Figure 1.2.** Schematic of laser spot position on the photodiode detector with cantilever deflections. Here, a laser spot is reflected off the backside of the cantilever to a quadrant photodiode detector. The normal deflection may be calculated by subtracting the voltage signal of the quadrants such that $(A+B) - (C+D)$. Photo credit to Ryan Fuierer.⁹ 7
- Figure 1.3.** (a) Example of a typical force curve displaying cantilever deflection as a function of tip-sample distance and (b) diagram of the cantilever deflection at each stage of the force curve.⁹ 9
- Figure 1.4.** Morse potential of a covalent bond (solid line) under an applied external force (light grey dashed line) in comparison to the unperturbed potential (dark grey dashed curve). The distance at the minimum of the unperturbed energy well is the equilibrium bond distance and V_0 is the energy of equilibrium dissociation. Addition of an external force extends the minimum outward and decreases the energy barrier to dissociation. Figure from Hanke and Kreuzer.¹⁹ 13
- Figure 1.5.** (a) Histogram of experimentally measured rupture forces of 10 base pair long double stranded DNA. The higher force rate causes the measured rupture force distribution to broaden and shifts to a higher average rupture force. (b) Experimentally measured logarithmic dependence of the force rate to the rupture force (most probably force from histograms shown in (a)) of double stranded DNA (also a linear dependence to the number of base pairs). From this plot, $\Delta x \ddagger$ is determined from the slope of the linear fit and k_{off} is determined by the intercept at zero force. The x -axis may be converted from velocity to force rate by multiplication of the force probe spring constant. Experimental data was published by Strunz *et al.*²³ 15
- Figure 1.6.** Example of friction response of a force probe using FFM. Here, the probe is scanned at a scan angle of 90° over a flat surface. Two materials with different friction coefficients can be identified without differences in height by changes in the lateral deflection of the cantilever. The friction force is calculated by half of the difference between the trace and retrace lateral deflection, removing the detector offset (dashed line) in the raw signal. 17
- Figure 1.7.** Interaction force profile as used in Hertz, JKR, and DMT contact mechanics with a cartoon of the adhesive contact area for each model.⁶ 20
- Figure 1.8.** Contact area *versus* load curves plotted for Hertz, JKR, and DMT contact mechanics models with $K = 1$ GPa, $R = 1$ nm, and $\pi W = 1$ J/m². The contact area *versus* load curves approach the Hertz curve as $W \rightarrow 0$ (*i.e.* no adhesion).³¹ 21

- Figure 1.9.** DNA is composed of four different nucleobases, adenine, guanine, cytosine, and thymine. Their structures consist of substituted purine and pyrimidine structures. **23**
- Figure 1.10.** (a) A thymine nucleotide is made of three basic components: the thymine nucleobase, a deoxyribose sugar, and a phosphate group. (b) A polynucleotide with bases A, C, and G is formed when a phosphate group covalently bonds to the C3' atom of a sugar on another nucleotide. **23**
- Figure 1.11.** (a) Structures of hydrogen bonded base pairs of A-T and C-G. For simplification, only the nucleobases are shown. (b) Polynucleotides with complementary base pairs form a right handed double helix. The grey ribbon is the phosphodiester-sugar backbone of the polynucleotide. Here, one strand of polynucleotides orients in the 5' to 3' direction and the other strand is in the 3' to 5' direction. **24**
- Figure 1.12.** A free-jointed chain random walk polymer with identical, rigid Kuhn segments of length, b , connected by flexible joints. R is the end-to-end distance of the polymer. **26**
- Figure 1.13.** (a) Diagram of the roll-up vector, \vec{C} , used to produce various types of CNTs. A sheet of graphene is wrapped along the roll-up vector to produce a CNT such that the roll-up vector is perpendicular to the long axis of the nanotube. \vec{C} for a (2,4) CNT is shown above. (b) Structure of the three types of CNTs (armchair, zigzag, and chiral). Figure published by Belin and Epron.³⁷ **27**
- Figure 2.1.** (a) Example of the flexural thermal noise spectrum showing the first three resonances and (b) torsional thermal noise spectrum obtained in air for a rectangular silicon cantilever (Probe #1, Table 2.1). **34**
- Figure 2.2.** Fitting of the flexural thermal noise spectrum (grey) to the SHO (solid line), Lorentzian (dashed line), and fluid-structure interaction (dotted line) models for a rectangular silicon cantilever in water (a) and ethylene glycol (b) (Probe #1, Table 2.1) **39**
- Figure 2.3.** (a) Schematic view showing cantilever plan view dimensions for an ideal rectangular cantilever, (b) and (c) are the cantilever side view images using an optical microscope (40× objective) and SEM, respectively, and (d) and (e) are the top view images using an optical (10× objective) microscope and SEM, respectively. Inset to (d) shows a top-view image with lighting at an oblique angle to illuminate the trapezoidal cross-section (20× objective). (Probe #5, Table 2.1). **41**
- Figure 2.4.** Flexural noise spectrum (a) and torsional noise spectrum (b) of a rectangular silicon cantilever (Probe #1, Table 2.1) in air. The dashed lines correspond to the fit to Equation 2.2. **47**
- Figure 2.5.** Flexural noise spectrum (a) and torsional noise spectrum (b) of a rectangular silicon cantilever (Probe #9, Table 2.1) in water 25-80°C. The dramatic shift in the amplitude of the resonance peak at 80°C is due to optical realignment of the laser spot on the cantilever (a change in the alignment effects the optical path).. **52**

Figure 2.6. Example of a torsional noise spectrum of a rectangular silicon cantilever (Probe #4, Table 2.1) in water. Dashed line corresponds to the fit to Equation 2.9.	57
Figure 2.7. Thermal spectrum background noise for the flexural response (a) and torsional response (b) in air (Probe #7, Table 2.1). The black curves are due to background noise and the red curves are experimentally measured cantilever noise.	61
Figure 2.8. Sample images of the Z-sensor (a), lateral trace (b) and retrace (c) channels with their accompanying cross-sectional plots. For the lateral images, the area inside of the green squares were used for calculations.	63
Figure 2.9. Friction force and friction offset as a function of applied normal load. Error bars correspond to the standard deviation at each load.....	64
Figure 2.10. Correlation between experimentally determined spring constants and corresponding values calculated based on material properties and dimensions of the cantilevers.	65
Figure 2.11. An example of a friction loop displaying the stick-slip turnaround point (fitted with a dashed green line) for a rectangular silicon cantilever on mica (probe 4).....	66
Figure 3.1. (a) Production of a Langmuir-Blodgett bilayer film. First, an organized layer of surfactant molecules are formed on the surface of water in a trough. As a hydrophobic substrate is dipped into the liquid, the hydrophobic tails of the surfactant interacts with the substrate through hydrophobic and van der Waals interactions. Upon removal, the top layer is formed through ionic interactions through the charged head groups. Charges are not drawn in this figure. (b) Chemical structure of poly(sodium 4-styrenesulfonate) (PSS, average molecular weight of ~70,000 g/mol) that served as a poly-ionic glue.....	69
Figure 3.2. Chemical structures of the LB film bilayers prepared on OTS modified silicon wafers. 1 Bilayer of polymeric surfactant; 2 Glued bilayer of polymeric surfactant; 3 Amphiphilic bilayer; 4 Glued amphiphilic bilayer; and 5 Polymeric base layer with a PSS gluing layer and a perfluorinated amphiphilic capping layer. The degree of polymerization, n , of films 1, 2, and 5 exceeds 50. (film thicknesses are not drawn to scale)	69
Figure 3.3. (a) Expanded view of a trench formed on film 5 with areas for use in step height calculations outlined by dotted lines. Areas around the scratch region where considerable debris from removal of the film is observed were avoided during film thickness measurements. (b) Histogram of the heights within the outlined regions. (c) Comparison of LB film thicknesses measured by AFM and ellipsometry. The errors for the AFM thicknesses are from the widths of the Gaussian fits (full width at half-maximum). The errors of the ellipsometry thicknesses are standard deviations from measurements at three different locations on the sample. The slope of the line fit is 0.97 ± 0.04	76

Figure 3.4. (a) A typical friction *versus* load curve for film 4. The three regions of deformation (labeled A, B, and C) are shown schematically in (b) (not drawn to scale). L is the total load (external load plus adhesion force). L_C and F^* are the normal and lateral forces, respectively, when the bilayer is damaged..... 78

Figure 3.5. (a) Four friction *versus* load curves for film 3 displaying consistency between trials. Different line patterns correspond to a different location on the same sample. (b) Friction *versus* load curves comparing the friction coefficients of methyl and fluorinated capping layers for films 2 (dashed) and 5 (solid). 80

Figure 3.6. (a) Effect due to the addition of a PSS interlayer for film 1 (dashed) and 2 (solid). and (b) for film 3 (dashed) and 4 (solid). 81

Figure 3.7. Comparison between glued bilayer films with and without cross-linked layers for film 2 (dashed) and 4 (solid). 84

Figure 3.8. Orientation of probe with respect to the sample surface. The probe is scanned in the x -direction, therefore the cantilever is measuring forces and the x and z -directions. The calculation of the von Mises stress is simplified since there are only normal stresses in the z -direction and shear stress in the x - y plane. 84

Figure 3.9. (a) Diagram of a probe with radius, R , indenting a distance, δ , into a thin film. The contact area, r_c , between the probe and film increase non-linearly with load. (b) Example of the quality of the fit to Equation 3.9 (dotted black line) for film 1 and 2. Since the point of contact with the film is ambiguous, an offset to the indentation of ± 0.5 nm was required to provide good fits. 88

Figure 3.10. (a) Height image of an ultra-sharp spike on a TGT01 calibration grating, (b) Line profiles of the tip image fitted with a sphere equation (dark lines) at the apex of the peak, (c) 3-D shape of the tip..... 94

Figure 3.11. Fitting of an friction *versus* load curve of a silicon probe on an OTS surface with equations for the COS, DMT, and JKR models. The intermediate model with $\alpha=0.7$ provides the best fit to our data. 95

Figure 3.12. (a) Height image of continually increasing applied set point (set point increases from bottom of the image to the top). (b) Dotted line corresponds to calculated friction along the indicated line in the height image against the total average friction *versus* load curve (solid line). 96

Figure 3.13. Averaged indentation curves for LB bilayer films..... 97

Figure 3.14. Lithography patterns (each pattern consists of separate, horizontal lines with increasing applied normal load) for three different AFM probes with spring constants ranging from 0.1 N/m to 3 N/m performed on Film 4. The Veeco silicon nitride contact mode probe produces damage at high applied normal loads, while showing no damage at low normal loads. The Budget Sensors Multi75 probe showed uncontrollable damage even at a low normal load and a Budget Sensors ContAl probe showed no damage even at high applied normal loads. Without calibration, the applied set point is proportional to applied normal load (the maximum experimentally accessible set point range is ± 10 V). 99

- Figure 4.1.** (a) Idealized cartoon (not drawn to scale) of frictionless peeling of a ssDNA homopolymer, attached to a gold coated force probe, from a graphite surface. Due to the frictionless nature of the substrate, the adsorbed bases slide freely on the surface and ssDNA detachment occurs perpendicular to the surface. (b) Typical force-distance curve for peeling 5'-poly(dT₁₀₀) ssDNA from the surface of graphite with illustration of oligomers adsorbed to the surface and steady-state peeling of a single oligomer. Orange boxes highlight areas that were used for averaging to determine the peeling force. Red curve is approach, blue is retraction. 102
- Figure 4.2.** (a) Peeling forces of 5'-poly(dT₁₀₀) on graphite from 25 to 40°C. (b) Adhesion forces of a silicon probe and teflon thin film in water in the temperature range of 25 to 50°C. Error bars are the standard deviation of the forces. 113
- Figure 4.3.** Force-distance curves obtained for probes functionalized with 5'-poly(dG₁₀₀) displaying peeling at separation longer than the oligomer contour length, (a), and short-ranged, high force peeling, (b). Orange boxes highlight areas that were used for averaging to determine the peeling force. 114
- Figure 4.4.** Proposed mechanisms to describe the possible reasons for observing: (A) force curves with small forces at separations larger than the ssDNA's contour length, (B) large forces at short separations, (C) and (D) both peeling and stretching of secondary structures. Red circles highlight areas of potential poly(dG) secondary structures. 115
- Figure 4.5.** (a) Peeling force *versus* separation distance scatter plot for several probes functionalized with 5'-poly(dG₁₀₀) and (b) Histogram of the peeling forces for the same series of 5'-poly(dG₁₀₀) probes displaying several peeling regimes. We assume that the peak at 63.8 ± 14.3 pN corresponds to the steady-state peeling a single poly(dG) oligomer. Higher forces are due to peeling of poly(dG) secondary structures. 116
- Figure 4.6.** Dependence of binding free energy per nucleotide on non-polar molecular area of a nucleobase. The dotted line is a fit to the data. 120
- Figure 4.7.** Typical force-distance curves obtained for probes functionalized with 5'-poly(dG₁₀₀) (200 nm/s retraction velocity, 10 mM phosphate buffer with 100 mM NaCl) showing peeling (a) and stretching (b). 120
- Figure 5.1.** Simulation results displaying stable barrel formation of three hydrogen bonded anti-parallel ATTTATTTATTT strands on the surface of a (8,4) CNT.⁴⁴ 123
- Figure 5.2.** Schematic representation of perpendicular peeling of DNA from horizontally suspended CNTs (left) and parallel peeling from vertically oriented CNTs (right). Each peeling type may occur with or without wrapping around the CNT. Figures are not drawn to scale. 124
- Figure 5.3.** Chemical modification of CNT by sonication in strong acid. Acid-modified CNTs were suspended with SDS and applied to an APTES modified surface. The acid group at the terminus of the CNT produces an ionic bond (likely stabilized with hydrogen bonding) with the APTES surface. Figure not drawn to scale. .. 127

- Figure 5.4.** Photolithography procedure to produce 1 μm wide and ~ 300 nm deep trenches on thermally grown silicon oxide. Figure not drawn to scale. **129**
- Figure 5.5.** Varying substrate tube densities based on the deposition procedure, (a) soaking in CNT suspension for 2 hours, (b) dip coating from CNT suspension, and (c) drop casting of CNT suspension. Images were captured using tapping mode imaging in air. The blurriness in the images is likely due to the CNTs swinging due to contact from the probe during imaging. **131**
- Figure 5.6.** (a) Representative image of the reconstructed height from a 32x32 force map of 5'-poly(dG₁₀₀) peeling on a suspended CNT sample. (b) Areas highlighted in red indicate force curves with peeling plateaus. Note that peeling plateaus are typically not isolated. Some of the highlighted force curves did not display plateaus long enough to calculate the peeling force. **134**
- Figure 5.7.** Representative force curves displaying (a) MHA coated probe interacting with a suspended CNT sample and (b) 3'-poly(dT₁₀₀) stretching on an APTES surface treated with SDS. Red curve is extension and blue curve is retraction.. **136**
- Figure 5.8.** Example force curves of (a) 5'-poly(G₁₀₀) and (b) 5'-poly(dT₁₀₀) peeling on suspended CNTs. Extension curves display variability due to interactions with swinging CNTs. Red curve is extension and blue curve is retraction. **137**
- Figure 5.9.** Examples of complex, periodic features during retraction in force curves for 5'-poly(dTdAdTdT)₂₀. Red curve is extension and blue curve is retraction. **139**
- Figure 5.10.** Typical force curve for 5'-poly(dTdAdTdT)₂₀ peeling on graphite. The large adhesion peak was excluded to show details of the peeling plateau. Red curve is extension and blue curve is retraction. Force curve was recorded by Suresh Manohar. **140**
- Figure 5.11.** (a) Isolated force *versus* distance data from the retraction region of force distance curve displayed in Figure 5.9a. Blue line is a smoothed curve to eliminate noise for FFT analysis. (b) Magnitude power spectrum density (PSD) of the stretching forces displays several peeling modes. **141**
- Figure 5.12.** An example of a force curve displaying stretching features during retraction with visualization of the associated AFM cantilever response and CNT bending. The stretching peak is due to taking up of slack within the suspended CNT and eventual removal. The red curve is extension and the blue curve is retraction. Cartoon is not drawn to scale. **144**

List of Tables

Table 2.1. List of cantilevers used in the calibration experiments with their measured dimensions and theoretical spring constants. All probes are fabricated from crystalline silicon, with probes 3-9 having a reflective aluminum coating.	45
Table 2.2. List of fit parameters in SHO model for flexural calibration of AFM cantilevers in air (viscosity $\eta_{\text{air}}=1.86\times 10^{-5}$ Pa·s, and density $\rho_{\text{air}}=1.18$ kg m ⁻³). $\text{OLS}_z^{\text{contact}}$ was calculated using Equation 2.6 ($\chi_z = 1.19$).....	47
Table 2.3. Flexural OLS determined in various fluids using a Lorentzian fit for a rectangular silicon cantilever (Probe # 1, Table 2.1). $\text{OLS}_z^{\text{contact}}$ was calculated using Equation 2.6a ($\chi_z = 1.19$).	49
Table 2.4. Flexural sensitivity determined in water between 25-80°C using a Lorentzian fit for a rectangular silicon cantilever (Probe #9, Table 2.1). $\text{OLS}_z^{\text{contact}}$ was calculated using Equation 2.6 ($\chi_z = 1.19$).	51
Table 2.5. List of fit parameters in SHO model for lateral calibration of AFM cantilevers in air ($\chi_\theta = 1$, $\eta_{\text{air}}=1.86\times 10^{-5}$ Pa·s, and $\rho_{\text{air}}=1.18$ kg m ⁻³).....	55
Table 2.6. List of fit parameters to Lorentzian model (in liquids) and SHO model (in air) for lateral calibration of AFM cantilevers in liquids. ($\chi_\theta = 1$)	59
Table 2.7. Lateral sensitivity determined in water between 25-80°C using a Lorentzian fit for a rectangular silicon cantilever (Probe # 9, Table 2.1). Refer to Table 2.4 for water viscosities and densities ($\chi_\theta = 1$).	59
Table 2.8. Results of example calculation of the lateral sensitivity using the wedge calibration procedure (Probe #5, Table 2.1).	64
Table 2.9. Comparison of OLS_x from friction loops and lateral thermal spectra.	66
Table 3.1. Applied normal and lateral forces at damage (L_c and F^* , respectively), adhesion forces (L_{ad}) measured from force curves, total normal load at damage, L^* (i.e. L_c+L_{ad}), and the film thickness, t_{AFM} and t_{ellip} , measured by imaging trenches via AFM and by ellipsometry, respectively.....	77
Table 3.2. The $S_y/K^{2/3}$ ratio, the Young's modulus of the film (E), yield strength (S_y), and the estimated indentation depth of the film at damage using E (δ^*_{calc}).	90
Table 3.3. Roughness values (5 μm \times 5 μm) for LB films measured by AFM.....	93
Table 4.1. Summary of all SMFS measurements of binding affinity between DNA homopolymers and graphite (\pm 95% confidence). The calculated binding energy was determined using equation 4.3.	117
Table 5.1. Summary of mean homopolymer oligomer peeling forces on suspended CNTs. Reported error is the standard deviation.	138

Abstract

Force spectroscopy has become a valuable tool to measure physical and chemical interactions at the molecular level through a variety of techniques. This dissertation focuses on applications of friction force microscopy and single molecule force spectroscopy to measure surface interactions of thin films and single molecules in a quantitative manner. Since the force microscope is capable of distinguishing very small forces (piconewton level), a precise and accurate calibration procedure is required. We present a rapid calibration procedure using the thermal noise spectrum of the cantilever to determine the normal and lateral force sensitivity without contacting any surfaces. Calibration without contacting a surface is advantageous because many experiments may require the force probe to be functionalized with molecules that may be damaged or removed during experiments.

The interactions between DNA and carbon nanotubes provide many potential applications in nanotube sorting and purification and therapeutic treatment of diseases. Fundamental knowledge of interactions between DNA and the surface of carbon nanotubes through simulations and experiments is essential in guiding the development of biomolecule complexes with nanomaterials. In order to model the interaction of DNA with a carbon nanotube, single molecule force spectroscopy was used to remove DNA from graphite. The removal of single-stranded DNA from a graphite surface resulted in steady-state peeling forces for each DNA homopolymer oligomer. The peeling forces for homopolymer oligomers on graphite produced the ranking $T \geq A > G \geq C$. However, it is fundamentally more interesting to directly measure the interaction through force

experiments between DNA and individual carbon nanotubes. Horizontally suspended carbon nanotubes were prepared through a simple, self-assembly method for use in DNA peeling experiments. The peeling forces of the DNA homopolymer oligomers on suspended carbon nanotubes decreased compared to graphitic substrates and produced the ranking $A \geq T \geq G > C$. For oligomers where tube wrapping and 3-dimensional structures are important for formation of stable complexes, force curves on suspended CNTs displayed a higher peeling force than force curves measured on flat surfaces. Oligomers having a “special sequence” motif capable of structural identification of CNTs based on size and chirality displayed periodic stretching features in peeling curves indicating the presence of intrastrand interactions.

Additionally, lateral force spectroscopy was used to detect differences in the yield strength of Langmuir-Blodgett bilayer films supported on solid substrates. We were able to damage Langmuir-Blodgett bilayer films controllably by a slow increase in the normal load, resulting in complete film removal. Film damage was detectable by abrupt changes in the friction forces of the films. This procedure enabled us to demonstrate the dramatic increase in the yield strength of Langmuir-Blodgett films due to addition of a poly-ionic interlayer that acted like a glue within the films.

Chapter 1 Introduction to Force Spectroscopy and Properties of Carbon Nanotubes and DNA

1.1 Synopsis

We are all familiar with the sensation and measurement of forces in our everyday lives, whether it's the force of gravity keeping you in your chair as you read this dissertation or the force required to propel a bicycle up a hill, for example. However, here, we are more interested in measuring the forces of microscopic processes rather than the macroscopic forces mentioned above. With current instrumentation we are capable of applying and measuring (small) forces at the molecular and atomistic scale. In the same way that we can clear a thin coating of fresh snow from a sidewalk with a shovel, we can also remove nanometer thick films (*i.e.* films so thin and pristine they are completely imperceptible to your eye) from a surface. We can also measure the forces required to detach a single molecular chain from a surface, just as we can peel off a piece of masking tape from a wall. This dissertation will discuss the application of forces to measure the strength of processes at these molecular levels. The results of the following experiments provide us with insight in how to strengthen thin films through the addition of molecules (in strategic locations) and provide understanding on the strength biomolecule complexes. The implementation of these results could have broad impact in applications ranging from ultra-efficient gas filters to new forms of therapeutic drug delivery systems and treatment of diseases. The remainder of this chapter will provide an introduction into the world of force spectroscopy and the measurement of forces at the molecular (even atomic) level to build an understanding for the experiments in the following chapters.

1.2 Force Spectroscopy

Force spectroscopy is an analytical technique that provides quantitative measurement of the mechanical properties of single cells or molecules as well as surface-surface interactions. Force spectroscopy of single cells or molecules provides detailed information not detectable by ensemble spectroscopic techniques, such as detection of intermediate pathways of protein folding. Many force spectroscopy experiments have provided valuable information on the mechanics of single molecule processes (*e.g.* polymer chain mechanics, protein unfolding, DNA unzipping, sequencing, and peeling) and the bond strength (*e.g.* covalent bonds, antibody-antigen binding) as well as the nature of nonspecific interactions (*e.g.* van der Waals forces, electrostatic forces, hydrophobic interactions).

The general specifications of a force spectroscopy system require measurement of piconewton level forces and sub-nanometer level displacements. Force spectroscopy experiments are generally completed by attaching a target molecule to a solid surface and pulling on the opposite end of the molecule with an applied force. There are several commonly used techniques to complete force spectroscopy experiments such as: optical and magnetic tweezers, electrophoretic techniques (*i.e.* electrophoresis and dielectrophoresis), fluid flow, surface forces apparatus, and scanning probe techniques.¹ Each of the mentioned force spectroscopy techniques have inherent advantageous and disadvantages depending on the scope of the experiment. In order for a molecule to experience a force in an optical, magnetic, or electrical field, the molecule must have contrasting dielectric or magnetic properties compared to the medium (this is usually accomplished by attaching a magnetic or dielectric particle to the end of a target

molecule). Performing force spectroscopy experiments with a specialized probe in an applied force field is often very attractive for applications for highly scalable processes (*i.e.* forces may be applied to a collection of many molecules simultaneously over the applied field), but the accessible forces are usually limited (< 200 pN).¹ Scanning probe microscopy allows for a much broader range of force measurement (10 pN - 100 nN) and also has the ability to apply and measure torsional forces. Overall, scanning probe microscopy is a more versatile force spectroscopy technique since it may be used in single molecule experiments as well as experiments measuring forces with a solid sample surface.

Scanning probe microscopy (SPM) systems are an imaging technique (invented in the mid 1980's) that can operate with a wide variety of samples (hard and soft materials, conductors and insulators, *etc.*), in a variety of imaging modes, and environments (gases or liquids, room or elevated temperature, controlled humidity, *etc.*). Modern commercial SPMs provide resolution in the range of several angstroms in the z -direction and nanometer resolution laterally. The advantages of SPM over optical and scanning electron microscopies are the ability to image (with simultaneous collection of physical and chemical properties) delicate samples in biological conditions with resolution below the diffraction limit. Recently, the use of SPM systems as an analytical instrument to map physical, chemical, and electrical properties at the nanometer scale has garnered much attention.² The technique for these various applications can typically be accomplished by simply modifying the force probe (*i.e.* adding chemical functionality) used in the experiment, biasing the tip with respect to the sample, or changing the scan direction (*i.e.* scanning perpendicular or parallel to the sample surface). Moving the force probe in the

z -direction (with a flat sample surface lying in the x - y plane) and measuring the cantilever deflection as the probe applies load to a sample or moves away from the surface can provide information on the surface adhesion or sample modulus.³⁻⁵ Scanning in the plane of the sample can provide information on the frictional properties of the sample or identify chemically different domains within the sample.⁶⁻⁸

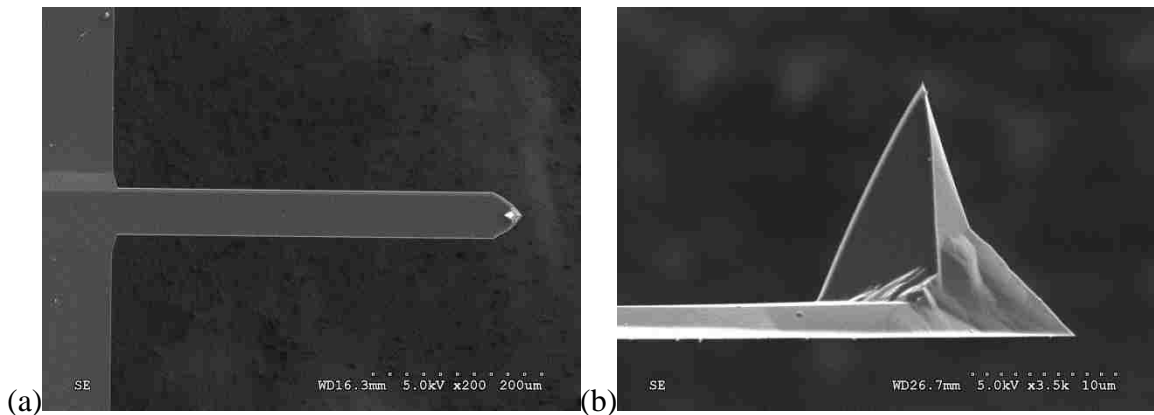


Figure 1.1. Scanning electron micrographs of a typical contact mode AFM probe. (a) Image showing the bottom surface of the cantilever. The bright spot at the end of the cantilever is the tip (shown from the side in (b)).

In this dissertation an atomic force microscope (AFM) was used, which operates using tips attached to small cantilevers with dimensions typically 20-50 μm in width and 200-500 μm in length (Figure 1.1). The force probe and sample are manipulated using piezo actuators to control the positioning and applied forces in all three dimensions. The AFM produces images or measures forces by gauging the deflection of the cantilever due to forces induced by the sample surface. The deflections can be measured through simple optics by reflecting a laser spot off the backside of the cantilever to be recorded on a quadrant photodiode. Figure 1.2 shows a simplified scheme of the laser-detector light path. The extent of deflection in the normal or torsional directions may be determined by

analyzing the linear combinations of the voltages in the individual quadrants of the photodiode. In Figure 1.2, the quadrants are labeled (A through D) clockwise from the top left. The calculation of the normal deflection may be found by taking the difference between the voltages on the upper and lower halves of the quadrant (*i.e.* $(A+B) - (C+D)$). Similarly, lateral deflections may be calculated by taking the difference between the left and right halves of the quadrant (*i.e.* $(A+C) - (B+D)$). The reference position of the laser spot within the quadrant (corresponding to zero force) may be centered or offset during experiments, since we are interested in the changes in deflection.

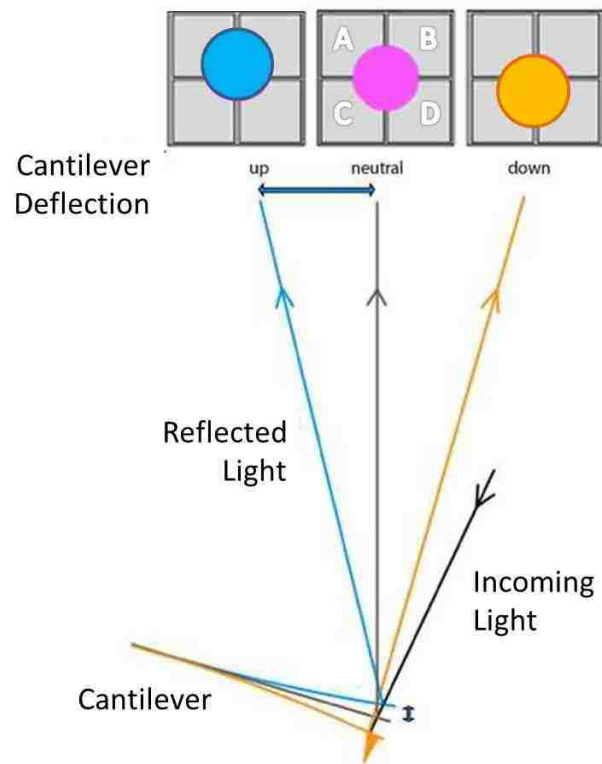


Figure 1.2. Schematic of laser spot position on the photodiode detector with cantilever deflections. Here, a laser spot is reflected off the backside of the cantilever to a quadrant photodiode detector. The normal deflection may be calculated by subtracting the voltage signal of the quadrants such that $(A+B) - (C+D)$. Photo credit to Ryan Fuierer.⁹

Force curves are a commonly used measurement in force spectroscopy that can provide information on the Young's modulus, chemical nature, or adhesion of a surface. Force curves are generated by moving the force probe in the z -direction (at a typical rate of ~ 100 - 1000 nm/s) to apply a load on the sample, followed by retraction from the surface. Often, we record force maps, which are arrays of force curves over a specified area, to determine a representative estimate of the surface interactions over a sample area (with varying expectations whether the sample is homogeneous or heterogeneous).

Figure 1.3 displays an example of a force curve, with the important regions of interest labeled. In regions A and F, the force probe has no deflection if no long range forces are present. In region B the force probe suddenly snaps into contact with the surface due to short range attractive van der Waals forces. In region C, the force probe is applying compressive forces on the sample. The slope of the deflection of region C is dependent on the sample stiffness. If the sample is soft, the slope will be reduced due to indentation into the sample. Furthermore, if the sample is a linear elastic material, the approach and retraction curves of the cantilever deflection in region C should overlap. The approach and retraction curves in region C do not overlap for viscoelastic materials. In region D, the force probe is still in contact with the sample at negative loads due to adhesion. The contact is abruptly broken in region E. The tip-sample adhesion force is then calculated from the difference between the minimum deflection (force) value from region D and the zero deflection in region F. However, in order to convert these cantilever deflections into forces, one needs a calibration procedure.

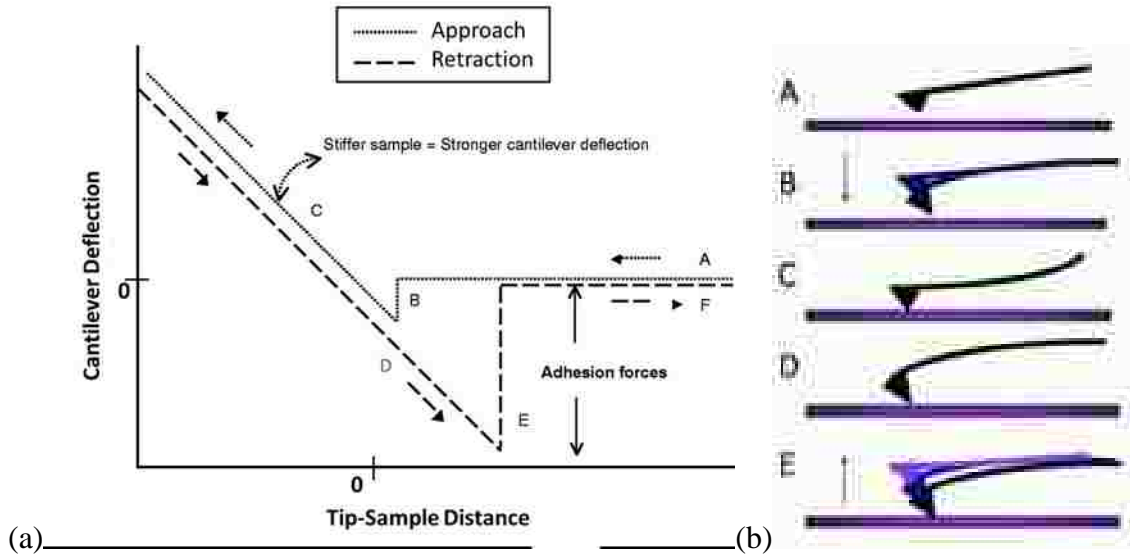


Figure 1.3. (a) Example of a typical force curve displaying cantilever deflection as a function of tip-sample distance and (b) diagram of the cantilever deflection at each stage of the force curve.⁹

1.3 Force Calibration

For force spectroscopy experiments on an AFM, there are two key components that need calibration – the optical detector (optical lever sensitivity, OLS) and the spring constant of the cantilever (k). The deflection measured by the detector, in units of volts, can be converted to force using the following relationship:

$$\text{deflection (V)} \cdot \text{OLS (nm/V)} \cdot k \text{ (nN/nm)} = \text{Force (nN)} \quad (1.1)$$

Each cantilever's spring constant requires individual calibration due to minor differences during production that results in different cantilever dimensions (the normal and torsional spring constants are largely dependent on the cantilever dimensions, see Equation 2.15 and 2.16).¹⁰ The actual spring constant can differ significantly from the average spring constant reported by the manufacturer. In order to determine the cantilever spring constant, we may estimate the theoretical spring constant based on the cantilever material and dimensions,¹¹ but this approach can prove problematic due to oversimplified

cantilever geometry (cantilevers are usually trapezoidal and not rectangular), large sensitivity to small errors in thickness (due to a cubic dependence), and inexact estimates of the Young's modulus and Poisson's ratio of the cantilever. However, a robust determination of the cantilever spring constant may be found by assuming the cantilever behaves like a harmonic oscillator. Then it is possible to determine the spring constant through analysis of the cantilever power spectrum (*i.e.* added mass procedure,¹² Sader method,¹⁰ or by the equipartition theorem¹³).

The final component requiring calibration is the response of the optical detector, typically called the optical lever sensitivity (OLS). The relationship of OLS requires a known cantilever deflection and the photodiode signal (*i.e.* voltage change within the photodiode quadrant). A unique OLS must be determined for every optical alignment of the laser-cantilever-detector optical path and is unique for each fluid used during the experiment (*e.g.* air, water, buffer, *etc.*) due to refraction of the laser beam at interfaces along the laser path. Determination of the OLS is typically straightforward for calibration of normal forces (*i.e.* slope of region C in Figure 1.3 if the sample is incompressible), but is often difficult to obtain without additional apparatuses or specifically designed calibration standards for the lateral calibration.^{14, 15} Correct calibration of the normal and lateral spring constants and OLS are discussed in further detail in Chapter 2.

1.4 Dynamic Force Experiments

Due to the ability of AFM to measure piconewton forces and ability to manipulate a force probe with angstrom precision, AFM has become the standard instrument to perform single molecule force spectroscopy (SMFS) experiments. It is possible to carry

out single molecule experiments with an AFM by careful consideration during the force probe/sample preparation (*i.e.* low density of a target molecule so that only forces of a single molecule are measured). AFM probes typically are made of silicon or silicon nitride and can be purchased with a variety of metal coatings (*e.g.* gold) allowing for the functionalization of the probe with common self-assembled monolayers (*i.e.* using silane or thiol chemistry). If a target molecule is sufficiently spaced on the force probe (and/or the substrate), it is possible to directly measure forces exerted on individual molecules. As described in Chapters 4 and 5, typically spacing of the molecules is achieved through deposition of target molecules with sub-monolayer concentrations and dilution with inert spacer molecules. However, in order to use experimental, dynamic force measurements to describe molecular processes (*e.g.* polymer chain entanglement, protein folding, *etc.*) or derive bonding energies, a proper theoretical model is required.

Evans and Ritchie extended Bell's model¹⁶ for describing dynamic force spectroscopy and relating the force of bond rupture to bond energy.¹⁷ It is possible to predict the change in the kinetics of bond dissociation with an added external mechanical force. As an example, this section discusses the dissociation of a covalently bonded diatomic molecule under a mechanical load. Traditionally, the dissociation of a diatomic molecule can be represented by a potential energy diagram with a local minimum corresponding to the equilibrium bond distance. The reaction coordinate of the potential energy well is the one-dimensional atomic separation, which is assumed to be the lowest energy pathway to dissociation (Figure 1.4). The shape of the potential well depends on the specific diatomic process being measured (*e.g.* covalent bond, weak van der Waals, or ionic interactions, *etc.*), however, it has been shown that for covalent bonds, a Morse

potential is an appropriate one-dimensional analytical representation.¹⁷⁻¹⁹ For a non-covalent interaction, a Leonard-Jones potential is often used. Bond breaking is a time-dependent thermally driven process where the lifetime of the bond depends on the depth of the potential well (activation energy), V_0 . Therefore, it is possible to calculate the first-order dissociation rate constant, k_0^{off} , via an Arrhenius equation:

$$k_0^{\text{off}} = Ae^{-\frac{V_0}{k_B T}} \quad (1.2)$$

and the probability that the bond is intact at time, t :

$$\frac{dP}{dt} = -Ae^{-\frac{V_0}{k_B T}}P(t) \quad (1.3)$$

The Arrhenius prefactor, A , contains information about changes in entropy from bond dissociation and internal energy redistribution within the molecule, k_B is Boltzmann's constant, and T is temperature. If an external force, f , is applied that shifts the unperturbed potential, $V(x)$, to a modified potential, $V_{\text{eff}}(x)$, by $V_{\text{eff}}(x) = V(x) - f(x_0 - x)$ (where x_0 is the equilibrium bond distance and x is the direction of the applied force), then the activation energy, V_0 , is reduced to:

$$\Delta V(f) = V_0 - f\Delta x^\ddagger \quad (1.4)$$

where Δx^\ddagger is the distance between the energy minimum and the transition state. Experimentally, it is difficult to apply a constant force (one needs to implement force feedback). Recently, Julio Fernandez developed a force-clamp force spectroscopy (*i.e.* applied force with a feedback loop to maintain a relatively constant force, rather than applying a constant force rate) procedure to measure the unfolding of proteins.^{20, 21} Under a constant applied force, it was shown that the unfolding rate during protein unfolding decays exponentially with time and increases exponentially with an increase in applied force.^{18, 21} Instead, forces are typically applied with a constant force rate:

$$\Delta V(f) = V_0 - \frac{df}{dt} t \Delta x^\ddagger \quad (1.5)$$

To derive the values of Δx^\ddagger and k_0^{off} , we must measure the bound rupture force over a large range of force rates. Equations 1.2 and 1.3 can be modified to include applied force at a constant rate:

$$k^{\text{off}}(f) = A e^{-\frac{V_0 - \frac{df}{dt} t \Delta x^\ddagger}{k_B T}} = k_0^{\text{off}} e^{\frac{\frac{df}{dt} t \Delta x^\ddagger}{k_B T}} \quad (1.6)$$

$$\frac{dP}{dt} = -A e^{-\frac{V_0 - \frac{df}{dt} t \Delta x^\ddagger}{k_B T}} P(t) \quad (1.7)$$

From Equation 1.6, it is clear that the addition of an external force reduces the lifetime of the bound state (due to an increase in the dissociation rate constant). In this example, it is assumed that rebinding of the molecule does not occur ($k^{\text{on}} = 0$). Figure 1.4 displays the change of a Morse potential with an applied force.

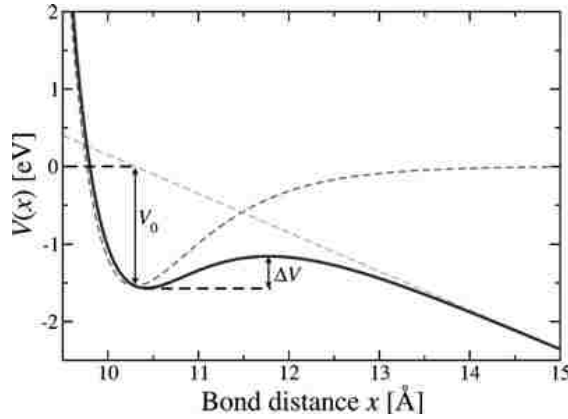


Figure 1.4. Morse potential of a covalent bond (solid line) under an applied external force (light grey dashed line) in comparison to the unperturbed potential (dark grey dashed curve). The distance at the minimum of the unperturbed energy well is the equilibrium bond distance and V_0 is the energy of equilibrium dissociation. Addition of an external force extends the minimum outward and decreases the energy barrier to dissociation. Figure from Hanke and Kreuzer.¹⁸

We may determine the probability that the bond still exists at a given force, f , by integrating equation 1.7 and substituting $(df/dt)*t$ by f .

$$P(f) = \exp \left[\frac{Ak_BT}{\frac{df}{dt}\Delta x^\ddagger} e^{\frac{V_0}{k_BT}} \left(1 - e^{-\frac{f\Delta x^\ddagger}{k_BT}} \right) \right] \quad (1.8)$$

The first derivative of equation 1.8 with respect to f provides the probability density distribution of force to rupture the bond in a given system (Figure 1.5(a) displays an example of distribution of experimentally measured bond rupture events, *i.e.* $\frac{\partial P(f)}{\partial f}$ vs. f).

Setting the second derivative of equation 1.8 to zero $\left(\frac{\partial}{\partial f} \left(\frac{\partial P(f)}{\partial f} \right) = 0 \right)$ provides the most probable force, f_{mp} , for bond rupture.

$$f_{mp} = \frac{V_0}{\Delta x^\ddagger} + \frac{k_BT}{\Delta x^\ddagger} \ln \left(\frac{\frac{df}{dt}\Delta x^\ddagger}{A} \right) = \frac{k_BT}{\Delta x^\ddagger} \ln \left(\frac{\frac{df}{dt}\Delta x^\ddagger}{k_BTk_0^{off}} \right) \quad (1.9)$$

As a result, the most probable bond rupture force increases logarithmically with the force rate.

This observation has been verified through simulations and experiments for several systems. For example, Strunz *et al.* showed the force rate dependence for unzipping double stranded DNA, and found very good agreement with the theory discussed above.²² Figure 1.5(a) displays the experimental dependence of unzipping 10 base pair long double stranded DNA over a wide range of force rates. Clearly, at higher force rates, the average rupture force increases. Strunz *et al.* also observed a logarithmic dependence of force rate to the rupture forces for several lengths of DNA duplexes, Figure 1.5(b). Fitting equation 1.9 to the data in Figure 1.5(b) allows for determination of the Arrhenius prefactor and the activation energy of bond dissociation. Beyer and

Clausen-Schaumann published a detail review outlining the experimentally measured rupture forces for several covalent bonds.²³

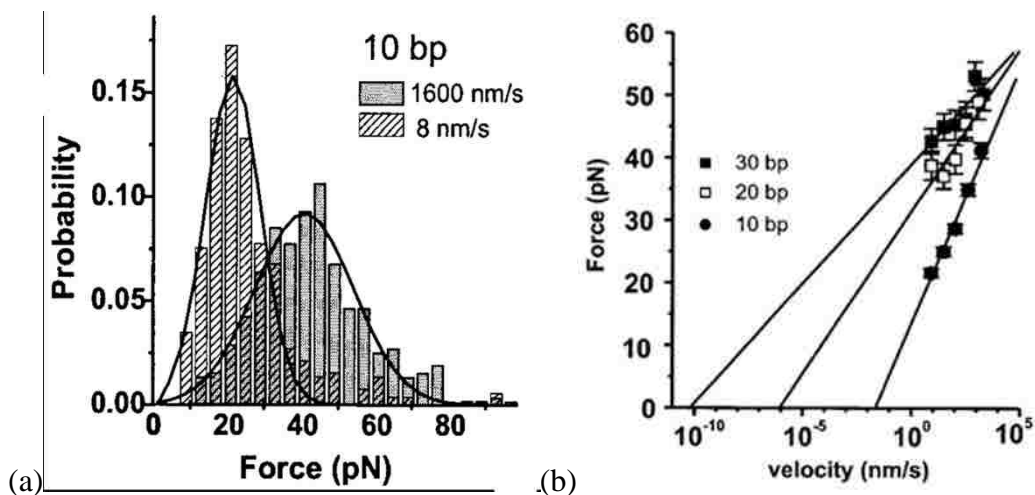


Figure 1.5. (a) Histogram of experimentally measured rupture forces of 10 base pair long double stranded DNA. The higher force rate causes the measured rupture force distribution to broaden and shifts to a higher average rupture force. (b) Experimentally measured logarithmic dependence of the force rate to the rupture force (most probably force from histograms shown in (a)) of double stranded DNA (also a linear dependence to the number of base pairs). From this plot, Δx^\ddagger is determined from the slope of the linear fit and k_0^{off} is determined by the intercept at zero force. The x -axis may be converted from velocity to force rate by multiplication of the force probe spring constant. Experimental data was published by Strunz *et al.*²²

The single-stranded DNA peeling experiments discussed in Chapter 4 are very different than the models and experiments discussed above. Foremost, instead of having a single dissociation event, peeling ssDNA from a surface has a multi-well energy landscape (for each adsorbed base) for dissociation. Furthermore, the adsorption rate (k_{on}) is not negligible. Statistical-mechanical models were created to calculate the binding energy per base of ssDNA.^{24, 25} The model assumes that the peeling of ssDNA from a surface is an equilibrium process in the sense that, at the peeling junction, individual bases of the molecule have sufficient time to sample all conformations in contact and free

from the surface. Since the experiments described in Chapter 4 do not use a force-clamp type of experiment, mentioned above (and due to fluctuations from the force probe), we do not observe base-by-base ratcheting as ssDNA is peeled from the surface.²⁶ Therefore, experiments display a constant force plateau that is punctuated by an abrupt jump to zero force upon removal of the final base (a non-equilibrium process). Manohar *et al.* experimentally determined that the peeling force of ssDNA from graphite is independent of the force rate over several orders of magnitude.²⁵ Simulations by Iliafar *et al.* suggest that force rates of the non-equilibrium peeling regime (where viscous drag dominates the pull-off force) are several orders of magnitude greater than what is experimentally accessible in force spectroscopy experiments (m/s vs. $\mu\text{m/s}$).²⁶ A model to describe the interaction between DNA and the graphite surface is discussed further in Chapter 4.

1.5 Friction Force Microscopy and Contact Mechanics Models

One mode of force spectroscopy discussed in detail in Chapter 3 is friction force microscopy (FFM). The friction forces can be measured on an AFM if the force probe is scanned in contact with the sample with a scan angle perpendicular to the long axis of the cantilever (*i.e.* a scan angle of 90°). An AFM creates an image by rastering back and forth (fast scan) over several scan lines (slow scan) to produce an image. Therefore, when referring to the scan angle, the angle is the fast scan direction with respect to the long axis of the cantilever. Friction forces are measured with a scan angle of 90° because the (lateral) cantilever deflection is only caused by friction forces experienced by the tip. It is known that there is coupling between both friction forces and sample topography when scanning in contact with a scan angle of 0° – both friction and height variations cause changes in cantilever deflection.²⁷

Besides providing friction forces of homogenous surfaces, FFM can also be used to distinguish two materials with different friction coefficients without any height differences. While producing an image, every scan line (in the fast scan direction) is imaged twice – in a trace (left-to-right) and retrace (right-to-left) direction. Resulting in the same lateral deflection magnitude but with opposite sign (direction) of the friction force. A friction trace and retrace of a single scan line is commonly referred to as a friction loop, and allows calculation of the friction force. Figure 1.6 shows an example of a force probe scanning over a sample with two different domains. The lateral deflection is recorded in both the trace and retrace directions as the probe moves across the fast scan direction. The lateral deflection is converted to friction force by $|trace - retrace|/2$ (along with a calibration constant to convert deflection to force, as described in Equation 1.1).

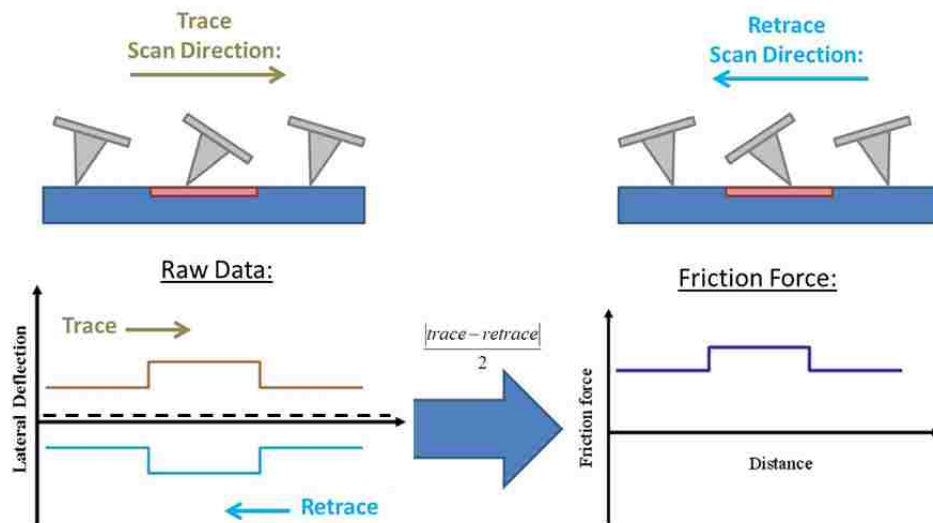


Figure 1.6. Example of friction response of a force probe using FFM. Here, the probe is scanned at a scan angle of 90° over a flat surface. Two materials with different friction coefficients can be identified without differences in height by changes in the lateral deflection of the cantilever. The friction force is calculated by half of the difference between the trace and retrace lateral deflection, removing the detector offset (dashed line) in the raw signal.

In order to quantitatively interpret many force spectroscopy experiments (*i.e.* work of adhesion, indentation, yield strength, *etc.*), the contact area between the force probe and the sample must be known. However, a measurement of the contact area is not directly accessible due to the size of the contact area. While it is possible to measure the tip radius via calibration gratings or scanning electron microscopy imaging, the probe contact area must be assessed during the force experiments, especially for soft samples, where the actual contact area changes significantly with the applied normal load. Therefore, we must adopt a contact mechanics model to estimate the actual tip-sample contact area.

The most commonly used contact mechanics models are Hertz,²⁸ Johnson-Kendall-Roberts (JKR),²⁹ and Derjaguin-Muller-Toporov (DMT)³⁰ contact mechanics. Hertzian contact mechanics was the first proposed contact mechanics model, but is still widely used today in many applications. Hertz theory assumes smooth contact between a sphere and a flat surface with isotropic, linear elastic materials with no adhesion forces. However, quantitative application of Hertz mechanics to microscopic experiments is usually not possible due to the lack of consideration for adhesion, which can play a large role in microscopic contact. Hertz derived that the circular contact area with a radius, a , depended on the applied load, P , such that:

$$a = \left(\frac{PR}{K}\right)^{1/3} \quad (1.10)$$

R is the radius of the spherical force probe and K is the elastic modulus of constant of the system given by:

$$K = \frac{4}{3} \left(\frac{1-\nu_1^2}{E_1} + \frac{1-\nu_2^2}{E_2} \right)^{-1} \quad (1.11)$$

E and ν are the Young's modulus and Poisson ratio of the sphere and the flat substrate, respectively.

Both JKR and DMT contact mechanics are improvements to Hertzian contact mechanics and account for tip-sample adhesion (Figure 1.7). Improved contact mechanics models were motivated by experimental observations with measured contact areas larger than what was predicted by the Hertz theory and experimental measurement of a finite contact area with zero applied load. The JKR theory considers the effect of contact pressure and adhesion within the area of contact, providing a modified equation for the contact area:

$$a^3 = \frac{R}{K} \left(P + 3W\pi R + \sqrt{6W\pi R + (3W\pi R)^2} \right) \quad (1.12)$$

where W is the work of adhesion. The JKR model yields a critical tensile load, P_c , (*i.e.* adhesion force) where a spherical probe and flat surface are separated.

$$P_c = -\frac{3}{2}W\pi R \quad (1.13)$$

In general, the JKR contact mechanics model is considered to be more applicable for soft samples (*i.e.* large sphere radius with strong, short-range adhesion forces).

DMT contact mechanics assumes the same contact area as the Hertzian model, but includes the adhesion arising from long-ranged forces around the contact area, such that:

$$a^3 = \frac{R}{K} (P + 2W\pi R) \quad (1.14)$$

yielding an adhesion force of:

$$P_c = -2W\pi R \quad (1.15)$$

Experimentally, it is found that the DMT contact mechanics model is generally applicable for hard samples (*i.e.* small sphere radius with weak, long-range adhesion forces).³¹

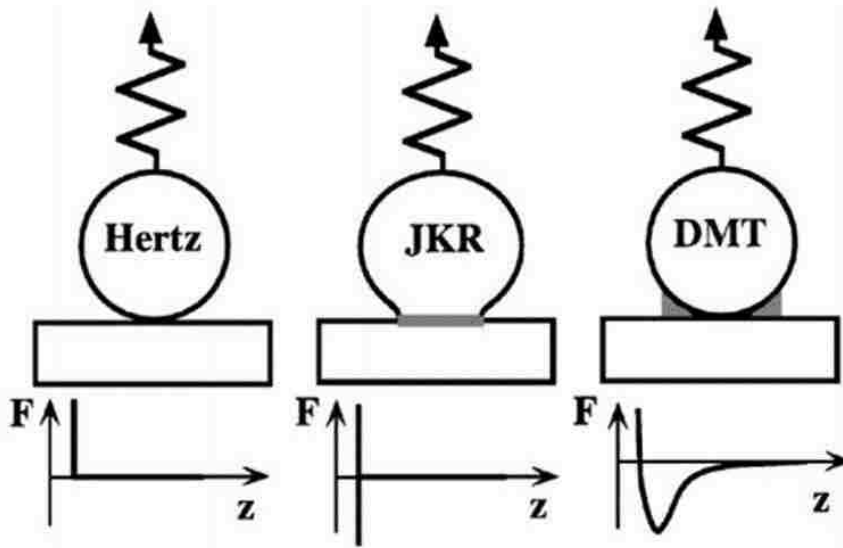


Figure 1.7. Interaction force profile as used in Hertz, JKR, and DMT contact mechanics with a cartoon of the adhesive contact area for each model.⁶

Overall, the differences between the contact mechanics models are due to considerations of the geometry of the contact area and adhesion forces. Experimentally, the contact mechanics regime in scanning probe microscopy is typically in an intermediate region between JKR and DMT models of contact mechanics. However, it is possible to apply an intermediate contact mechanics model to fit actual experimental results.³²

Since friction is expected to scale with the contact area between the tip and the sample, the predicted friction forces will depend on the selected contact mechanics model (Figure 1.8). One can adopt a more complex contact mechanics model based on the sample structure (especially in the case of a compliant film on a rigid substrate),^{3, 33} but the practice of fitting complex models to experimental data is not straightforward. In Chapter 3, I will discuss the application of an intermediate contact mechanics model^{32, 34} to interpret nanoscopic scratch tests for ultra-thin films in order to estimate the Young's modulus to determine the yield strength of the film.

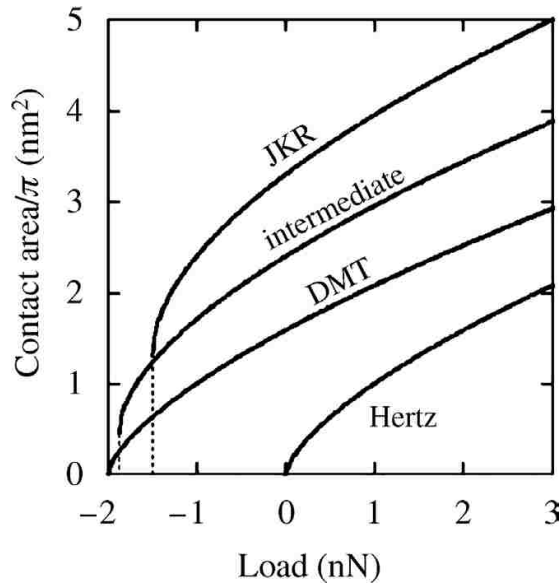


Figure 1.8. Contact area *versus* load curves plotted for Hertz, JKR, and DMT contact mechanics models with $K = 1$ GPa, $R = 1$ nm, and $\pi W = 1$ J/m². The contact area *versus* load curves approach the Hertz curve as $W \rightarrow 0$ (*i.e.* no adhesion).³¹

1.6 Introduction to DNA Structure and Modeling

Deoxyribonucleic acid (DNA) is the one of the largest and most complex self-assembled polymer that serves as the fundamental building blocks of life. DNA codes and transmits the essential genetic components that determine the design of an organism. DNA is made of four nucleobases that are derivatives of purine (*i.e.* adenine (A) and guanine (G)) and pyrimidine (*i.e.* cytosine (C) and thymine (T)), see Figure 1.9. These nucleobases can form a nucleic acid with the addition of a sugar and a phosphate group, see Figure 1.10(a). Although this description focuses on DNA, ribonucleic acid (RNA) has a similar structure with the substitution of uracil for thymine bases and a ribose sugar rather than the deoxyribose sugar. Numbering the cyclic rings of the bases and sugar, a nucleoside is formed by covalent binding between the C1' atom of the sugar and the N1 atom of a pyrimidine base (N9 atom for a purine base). A nucleotide is formed when a phosphate group covalently attaches to the C5' atom of the sugar. Then, nucleotides can link together to form a chain of single-stranded DNA (ssDNA) by connection between the phosphate group in the C5' location of one deoxyribose sugar ring to the C3' location of another deoxyribose sugar ring. Figure 1.10(b) shows an example of a short ssDNA polynucleotide with a phosphodiester backbone and side groups made of nucleobases. In solution at a neutral pH, the phosphate-sugar backbone gives the nucleotide a negative charge. In nature, polynucleotides can be millions of bases in length.

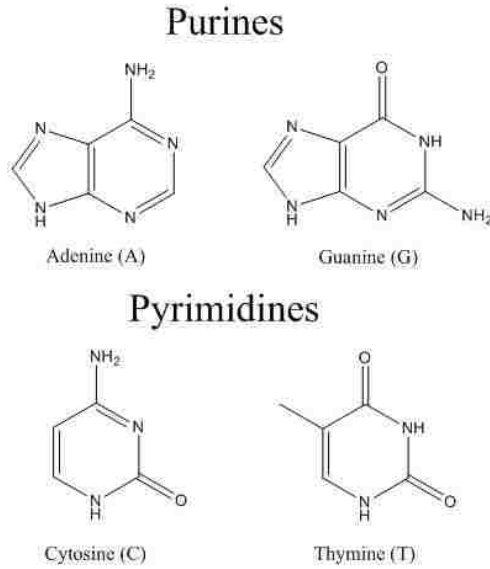


Figure 1.9. DNA is composed of four different nucleobases, adenine, guanine, cytosine, and thymine. Their structures consist of substituted purine and pyrimidine structures.

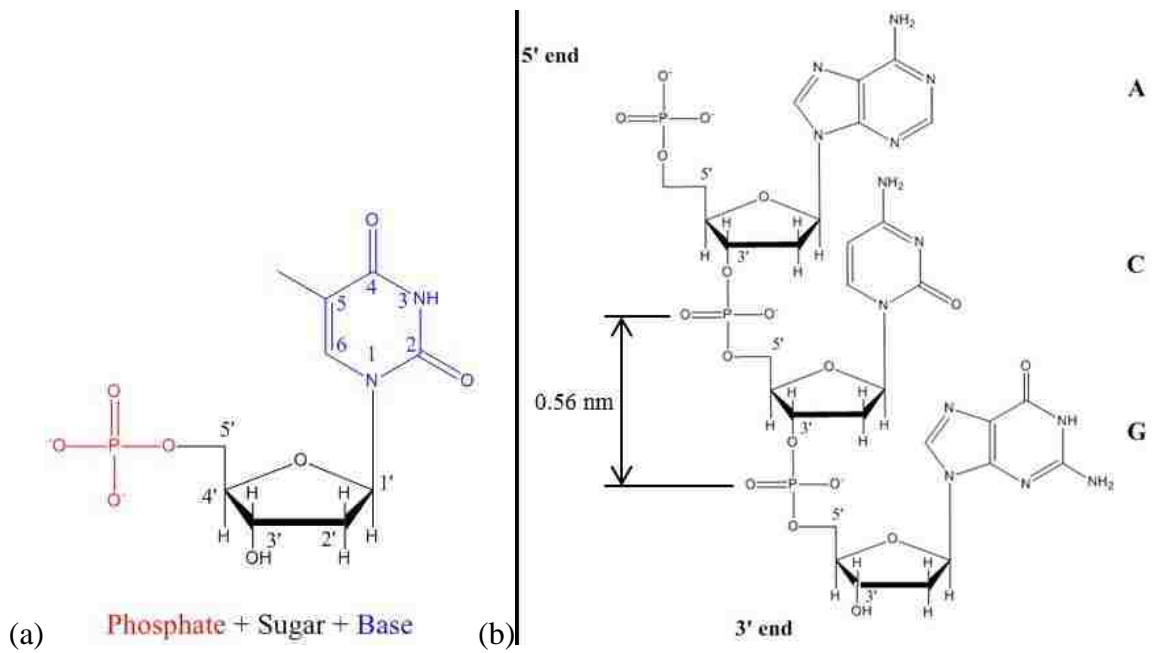


Figure 1.10. (a) A thymine nucleotide is made of three basic components: the thymine nucleobase, a deoxyribose sugar, and a phosphate group. (b) A polynucleotide with bases A, C, and G is formed when a phosphate group covalently bonds to the C3' atom of a sugar on another nucleotide.

In order to name the sequence of a polynucleotide, listing of the nucleobases begins at the end of the strand with a free phosphate group (5' end) and terminates at the end with a free hydroxyl group (3' end). The most stable base pairs are formed through hydrogen bonding of A with T and C with G, Figure 1.11(a), which are defined as complementary. Two complementary polynucleotides form double-stranded DNA (dsDNA) with a double helix conformation with a diameter of ~2 nm and 0.38 nm/base in length, Figure 1.11(b). In order to form dsDNA, the two polynucleotides orient so that the ssDNA strands run in the opposite direction (*i.e.* a 3' end of one strand and a 5' end of the other strand are attached at each end). The bases organize in the double helix such that the bases are bonded in the center of the helix and the negatively charged hydrophilic phosphodiester-sugar backbone is facing outward (grey ribbon in Figure 1.11(b)).

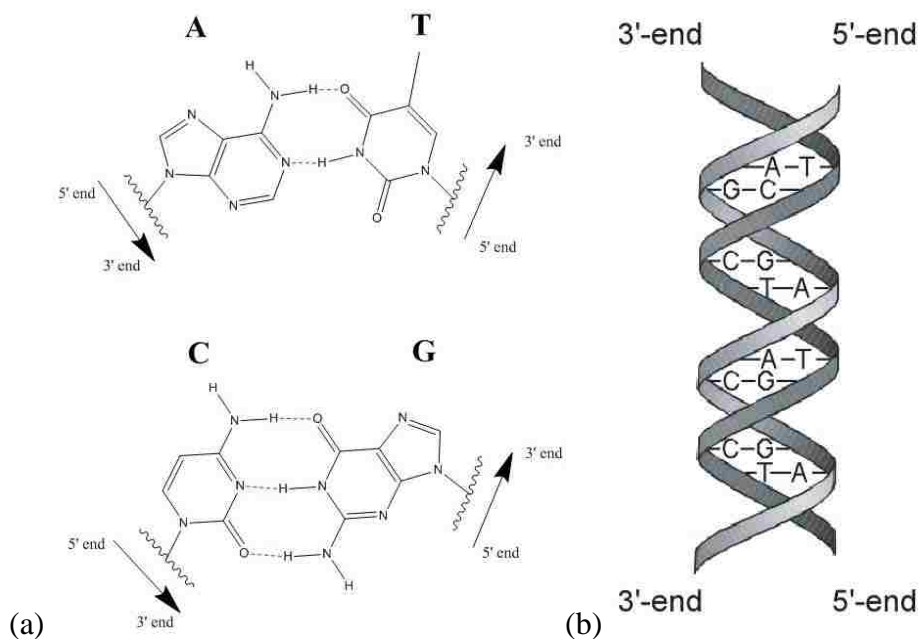


Figure 1.11. (a) Structures of hydrogen bonded base pairs of A-T and C-G. For simplification, only the nucleobases are shown. (b) Polynucleotides with complementary base pairs form a right handed double helix. The grey ribbon is the phosphodiester-sugar backbone of the polynucleotide. Here, one strand of polynucleotides orients in the 5' to 3' direction and the other strand is in the 3' to 5' direction.

When DNA is placed under a mechanical load, the response can be estimated by polymer chain models. Although the freely-jointed (FJC) chain model is perhaps the simplest model to describe a polymer (since all monomer interactions are ignored), the FJC model generally predicts the behavior of ssDNA quite well. A worm-like chain model (WLC) is generally more applicable for dsDNA. The FJC model consists of a random walk polymer chain with rigid segments (Kuhn segments) connected by flexible joints (Figure 1.12). For ssDNA, there are N total segments that have a fixed length (Kuhn length), b , of ~ 0.6 nm. Since the FJC model does not account for any interactions or bending energies within the polymer chain, it is often possible to experimentally fit for the value of b under exact experimental conditions (accounting for salt concentration, steric hindrance within the chain, *etc.*). The contour length of the polymer chain, L , is given by $L=N \times b$. If no force is applied to the polymer chain, the chain is free to assume a random orientation where the average end-to-end distance is $\langle R^2 \rangle = Nb^2$. The elasticity of a FJC chain can be determined by force *versus* extension curves. When the polymer chain is subjected to an external force, f , the segments will tend to align parallel to the force direction and the average end-to-end distance will become:

$$\langle R \rangle = N b \left[\coth \left(\frac{fb}{k_B T} \right) - \frac{k_B T}{fb} \right] \quad (1.16)$$

The FJC model takes into account that the extension of the molecule under force may not exceed the contour length and the elasticity of a FJC is entropic in nature and is a thermally driven process. In Chapter 4 we discuss the application of the FJC model in relation to the quasi-equilibrium peeling of ssDNA from graphite. We use an improved FJC model to account for the chain elasticity.

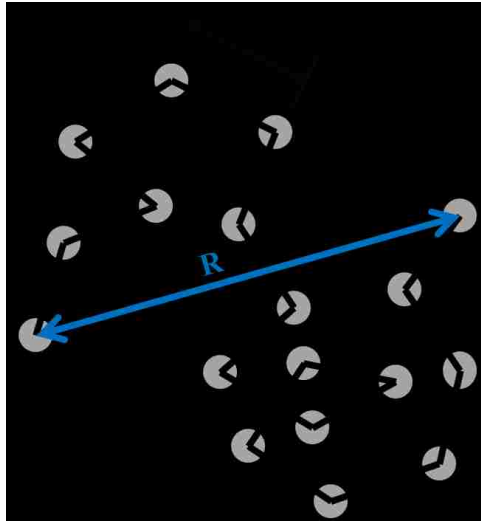


Figure 1.12. A free-jointed chain random walk polymer with identical, rigid Kuhn segments of length, b , connected by flexible joints. R is the end-to-end distance of the polymer.

1.7 Introduction to the Structure and Properties of Carbon Nanotubes

This section will briefly introduce the nomenclature and properties of carbon nanotubes. Carbon nanotubes (CNTs) were initially brought to large scale attention in 1991 by Iijima,³⁵ and since then, have been an active subject of research due to their unusual electronic, chemical, optical, and mechanical properties. CNTs are typically synthesized by arc discharge, laser ablation, or chemical vapor deposition, which largely produces a random assortment of single and multi-walled CNTs with various tube lengths, diameters, and chiralities with contamination of other graphitic species and catalyst.³⁶ A CNT may have three possible tube chiralities (armchair, zigzag, and chiral) that can determine the electronic properties of the CNT. To visualize the CNT chirality, we may create a CNT by rolling a 2-D graphene sheet into a cylinder using various vectors on a lattice of carbon atoms. The roll-up vector (or chiral vector), \vec{C} , is defined

by the hexagonal unit vectors of graphene (Figure 1.13), \vec{a}_1 and \vec{a}_2 , such that $\vec{C} = n\vec{a}_1 + m\vec{a}_2$ (m and n are integers). A zigzag CNT is produced by the roll-up vector $n\vec{a}_1 + 0$, and an armchair CNT is produced by the roll-up vector $n\vec{a}_1 + n\vec{a}_2$. A chiral CNT is produced by any other combination $n\vec{a}_1 + m\vec{a}_2$.³⁷ For a given (n, m) CNT, a tube is metallic in nature if $n=m$ (i.e. armchair) or if the difference of n and m is a multiple of three. Thus, as-synthesized CNTs consist of a mixture of 33% metallic tubes and 66% semiconducting tubes.³⁶ The roll-up vector, \vec{C} , also determines the diameter of the CNT (~0.4–5 nm, CNTs with a diameter larger than 5 nm are expected to collapse).³⁸ The tube diameter is important in the case of semiconducting CNTs, where the band gap is inversely proportional to the tube diameter.

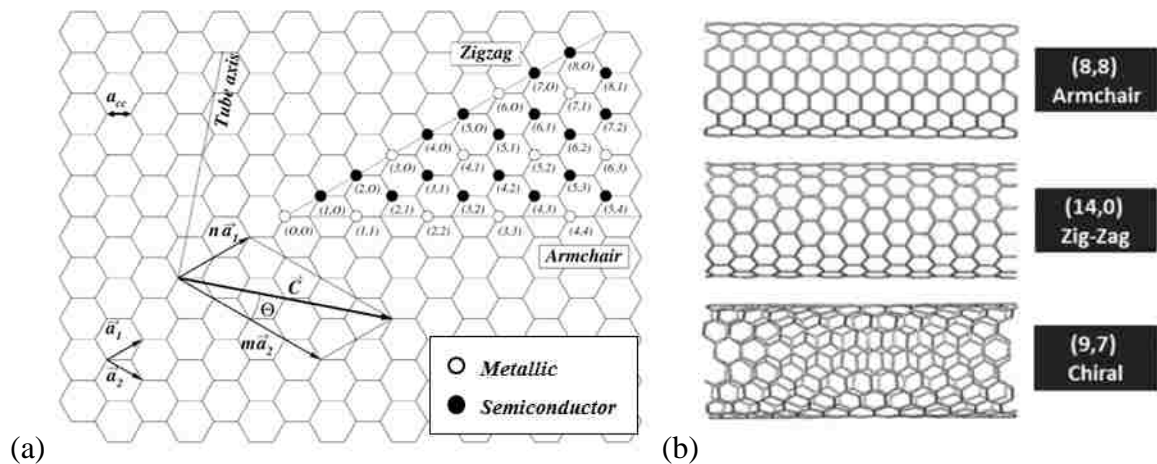


Figure 1.13. (a) Diagram of the roll-up vector, \vec{C} , used to produce various types of CNTs. A sheet of graphene is wrapped along the roll-up vector to produce a CNT such that the roll-up vector is perpendicular to the long axis of the nanotube. \vec{C} for a (2,4) CNT is shown above. (b) Structure of the three types of CNTs (armchair, zigzag, and chiral). Figure published by Belin and Epron.³⁷

The unique characteristics of CNTs are promising for future applications in nanoelectronic devices, composite reinforcement, sensors, and solar cells. The Young's modulus of a CNT (~1 TPa) is much greater than that of steel (~200 GPa). The CNTs can withstand high longitudinal strains (~20%), not typical of most materials.³⁹ The properties CNTs are advantageous for the production of sensors since the electronic properties of CNTs vary with strain.^{40, 41} However, the extremely high aspect ratio of the CNT dimensions, which make CNTs a unique material, also makes the processing of individual CNTs in bulk difficult. CNTs are known to spontaneously produce bundles due to van der Waals interactions.³⁶ Breaking up the CNT bundles for bulk single tube processing (which is a requirement for most applications) is paramount in the furthering of future CNT applications. Furthermore, in many applications, individual CNTs must be treated without modification of the chemical, electronic, or mechanical properties of the CNT.

It has been shown that dispersion of individual CNTs can be accomplished in solution through formation of stable complexes with surfactants and biomolecules.^{36, 38} High resolution imaging⁴² and simulations⁴³⁻⁴⁶ revealed that ssDNA wraps around the outside of a CNT in a helical fashion (similar to the dsDNA helix displayed in Figure 1.11(b), but without a complementary polynucleotide). The helical DNA-CNT complex orients such that the bases interact with the surface of the CNT (through hydrophobic and electrostatic interactions) and the phosphate backbone is exposed to the solution. The outward facing negative charge of the phosphodiester backbone allows for electrostatic repulsion of CNTs in solution, reducing bundle formation. Chapters 4 and 5 discuss the

measurement of the interaction forces of DNA with carbon surfaces to help understand the driving forces for the formation of DNA-CNT complexes.

1.8 Scope of the Dissertation

This dissertation discusses two applications of force spectroscopy: yield strength measurements of ultra-thin organic films on solid substrates and direct measurement of the interaction strength between single-stranded DNA and carbon surfaces. Since accurate and quantitative results are essential for the experiments described above, methods for force calibration are discussed in Chapter 2. We have shown that the cantilever may be fully calibrated (normal and lateral sensitivities) with only the use of the cantilever dimensions and the cantilever oscillations from thermal noise. Complete force calibration can be accomplished without contacting any surfaces, which is useful for experiments in which the force probe may be functionalized with delicate molecules or films. Furthermore, this procedure is applicable for use in a variety of fluids and at temperatures common to force spectroscopy experiments.

Thin films have become popular in functionalizing surfaces with unique properties useful for protective coatings and lubricants,⁴⁷ sensors,^{48, 49} and molecular filters.⁵⁰ Ultra-thin films deposited by the Langmuir-Blodgett method⁵¹ (LB) typically rely on weak interactions between the film and the supporting substrate, thus limiting their applicability for everyday use. It was hypothesized that the overall stability of a LB bilayer film could be increased by adding additional crosslinking within the film to serve as a molecule “glue”.⁵² Previously, measurements of the mechanical stability were completed through indirect methods (surface viscosities and pressure-area isotherms), but

a direct, mechanical experiment is the ideal measure of the film robustness. Chapter 3 describes a new, rapid measurement of thin film yield strength for several LB bilayer films. Our method improves on other procedures by capturing many applied loads within a single image (about 4 minutes) with statistical averaging at each individual load. The film yield strength was interpreted from critical normal and lateral force points during scanning. Overall, it was determined that inclusion of a molecular “gluing” layer increases the stability of LB films. The thin film yield procedure described in Chapter 3 is not only unique to LB films, but applicable for other organic and inorganic thin films.

The second application of this dissertation uses single molecule force spectroscopy to probe the interactions between DNA and carbon nanotubes. Recently, there has been an increased interest in interactions between DNA and nanomaterials. Specifically, we are interested in the interaction between DNA and carbon nanotubes (CNTs), which have displayed promise in applications for tube purification, sorting, and positioning,⁴³ optical sensing,⁵³ and drug delivery.⁵⁴ However, the mechanism behind the helical wrapping of DNA around CNTs is poorly understood, and it is not clear why certain DNA sequences are capable of structural recognition of CNTs.⁴⁴ In Chapter 4 we have determined the ranking of the interaction strength for all four DNA homopolymer oligomers on graphite. Graphite was used as an analogous substrate to the surface of a CNT – the DNA predominantly interacts with the top surface layer of graphite (*i.e.* graphene). It was determined that the interaction between DNA and graphite is largely hydrophobic in nature, but we were not able to individually distinguish all four homopolymer oligomers. Since DNA is not able to orient in a reproducible 3-dimensional conformation on a flat surface, as seen on CNTs through high resolution imaging and

simulations,^{42-46, 55} it is possible that the oligomer interaction strengths may differ between flat surfaces and CNTs.

In Chapter 5, we describe the creation of a substrate with suspended CNTs to measure the interaction strength between DNA and CNTs rather than flat substrates, so the natural, 3-dimensional wrapping conformation of DNA on a CNT may be probed. A different ranking of peeling forces was found when the DNA interacts with suspended CNTs and is potentially free to wrap around CNTs. More importantly, peeling forces on suspended CNTs show complex structure beyond steady state peeling for ‘special’ sequences that strongly interact with specific CNT chiralities.^{42, 44} Peeling DNA from suspended CNTs allows us to probe the DNA-CNT interactions as well as the intrastrand interactions of DNA that were not accessible experimentally until now, but are known to play a role in CNT wrapping.⁴⁶

Chapter 2 Noncontact Method for Calibration of Lateral Forces in Scanning Force Microscopy

Most of the work described in this chapter has been published in Wagner, K.; Cheng, P.; Vezenov, D., Noncontact Method for Calibration of Lateral Forces in Scanning Force Microscopy, Langmuir, 2011, 27, 4635-4644.

2.1 Introduction

Lateral force microscopy (LFM, or friction force microscopy) is a valuable tool for nanoscopic characterization of friction at the interface between various materials. The LFM setup provides a well-defined single asperity contact amenable to theoretical treatment in describing chemical⁵⁶ and atomic scale⁵⁷ effects in nanotribology. The application of LFM is highly relevant for fundamental studies of friction^{31, 58-61} as well as for applications such as microelectromechanical devices.⁶²⁻⁶⁴ Calibration of forces in LFM, however, often requires extra experiments using additional hardware or specialized calibration gratings. Recently, two extensive reviews have summarized a complete compendium of calibration procedures for normal and lateral sensitivities for scanning force microscopy.^{14, 15}

For quantitative force measurements, one usually calibrates the sensitivity of the force microscope to convert the photodiode detector raw signal (Volts) to forces (Newtons) exerted on the cantilever due to interactions operating in the tip-sample contact (k is the cantilever spring constant and OLS is the Optical Lever Sensitivity):

$$Force (N) = Sensitivity (N/V) \cdot Detector Signal (V) \quad (2.1a)$$

$$Force (N) = [k (N/m)/OLS(V/m)] \cdot Detector Signal (V) \quad (2.1b)$$

This calibration can be readily done for normal forces (flexural bending of the cantilever) by establishing the OLS for a particular experimental arrangement in a given instrument

(keeping the same mechanical parameters of the cantilever, optical properties of cantilever material, and cantilever/laser-beam alignment). The OLS is the magnitude of the detector response due to the displacement of the tip. Using OLS, the spring constants can be found from the thermal noise spectra of the cantilevers on the basis of the equipartition theorem (*i.e.* $k = \frac{k_B T}{\langle z^2 \rangle}$, k_B is Boltzmann's constant, T is temperature, and $\langle z^2 \rangle$ is the mean squared cantilever fluctuations),^{13, 65} resulting in a fully calibrated setup (Equation 2.1b).

The OLS for normal forces is easily derived from the contact part of the force-distance curves measured on rigid substrates, where the sample indentation is negligible. If the sample is compliant or soft (*e.g.* surface of a cell or organic polymer) with stiffness comparable to the cantilever spring constant, a separate calibration step will have to be carried out on a different, rigid sample. For the torsional mode, finding a correct OLS from similar lateral force-distance curves (stiction part of friction loops, *i.e.* static friction *versus* lateral tip movement) is not straightforward for standard integrated tips, because the tip-sample contact stiffness is often comparable to the lateral spring constant of the cantilevers and, therefore, tip-sample deformations cannot be ignored (unlike the indentation for the same sample).⁶⁶ The problem is typically resolved by using a calibration grating presenting a surface with a well-defined slope and acquiring the friction response at a series of applied loads (wedge calibration method).^{67, 68} The wedge calibration is clearly not an *in situ* method (unlike the case of the thermal noise method for calibration of normal sensitivities) and requires specially designed calibration

samples. Quantitative analysis of friction taken with each specific probe and/or instrument alignment requires a unique calibration.

Here, we present an alternative, simple, and rapid lateral calibration that uses the thermal noise spectrum of the free cantilever in a fluid as the only experimental input required calibration. The method is based on the observation that OLS (along with the cantilever stiffness) determines the raw amplitude of the detected noise spectra.^{10, 69-71} If the cantilever spring constants are known independently, then the thermal noise spectra can be used to derive OLS from Equation 2.1b as demonstrated by Higgins *et al.*^{72,73}

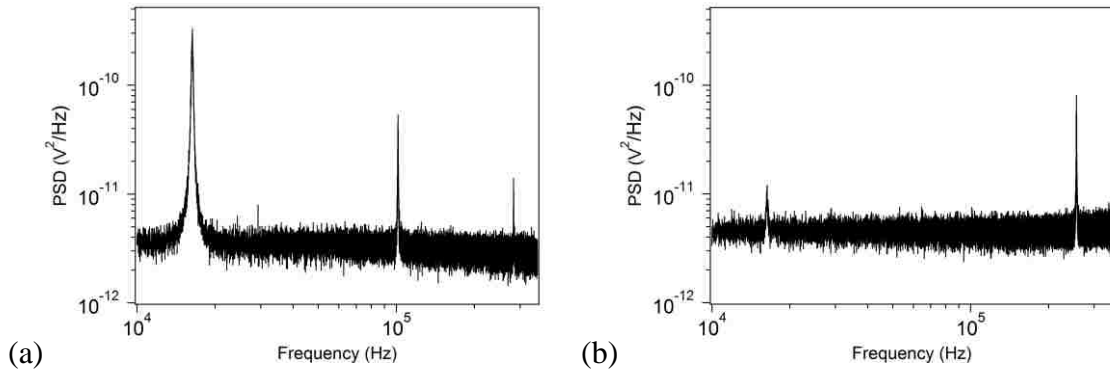


Figure 2.1. (a) Example of the flexural thermal noise spectrum showing the first three resonances and (b) torsional thermal noise spectrum obtained in air for a rectangular silicon cantilever (Probe #1, Table 2.1).

2.2 Approach

Previously, Green *et al.* have used the torsional and flexural thermal noise spectra of a free cantilever in a fluid to determine the normal and torsional spring constants.⁷⁴ Figure 2.1 shows examples of flexural and torsional thermal noise spectra of a rectangular-shaped silicon cantilever in air obtained with a commercial microscope. Experimentally, the flexural and torsional resonance peaks can be measured separately by changing the method the quadrant photodiode detector measures the amplitude of the

power spectrum (*i.e.* mathematical calculation of normal or torsional deflections on the quadrant photodiode detector as described in Section 1.3). There is good separation between the flexural and torsional resonance peaks and both peaks have high quality factors (Q) in air ($Q_{\text{normal}}=65$, $Q_{\text{torsional}}=290$). The resonance peaks in the power spectral density (PSD, in units of V^2/Hz) of thermally excited cantilevers can be fitted well by a simple harmonic oscillator (SHO) model, Equation 2.2, for both flexural (z) and torsional (θ) modes in air (here, $A_{SM}(v)$ is the single mode signal amplitude from the detector at frequency v , A_{DC}^2 (units of V^2/Hz) is the power at DC and is the parameter that incorporates detector sensitivity (the amplitudes at DC and at resonance are related by $A_{res}=A_{DC}Q$), Q is the quality factor, v_0 is the natural (\approx resonance) frequency, and A_0^2 is the overall system noise floor (assumed to be white noise here) and includes the DC power from higher order modes):⁶⁹

$$A_{SM}^2(v) = A_{DC}^2 \frac{v_0^4}{(v_0^2 - v^2)^2 + \left(\frac{v_0 v}{Q}\right)^2} + A_0^2 \quad (2.2)$$

The PSD of the detected thermal noise signal relates to PSD of z deflection (or torsional angle θ) via OLS (in V/m for S_z or V/rad for S_θ) as $PSD_{(v^2/\text{Hz})} = OLS^2 \cdot PSD_{(m^2/\text{Hz})}$.

Integration of Equation 2.2 ($\langle A^2 \rangle - \langle A_0^2 \rangle = \int_0^\infty A_{SM}^2(v) dv$) provides the power of the

fundamental mode. The flexural optical lever sensitivity is then expressed by:

$$OLS_z^{free} = \sqrt{\frac{\langle A^2 \rangle - \langle A_0^2 \rangle}{\langle z^2 \rangle}} = \sqrt{\frac{(\langle A^2 \rangle - \langle A_0^2 \rangle) k_z}{k_B T}} = \sqrt{\frac{\pi A_{DC}^2 Q v_0}{2} \frac{k_z}{k_B T}} \quad (2.3a)$$

or for the torsional OLS:

$$OLS_{\theta}^{free} = \sqrt{\frac{\langle A^2 \rangle - \langle A_0^2 \rangle}{\langle \theta^2 \rangle}} = \sqrt{\frac{(\langle A^2 \rangle - \langle A_0^2 \rangle) k_{\theta}}{k_B T}} = \sqrt{\frac{\pi A_{DC}^2 Q v_0}{2} \frac{k_{\theta}}{k_B T}} \quad (2.3b)$$

We will show that the result of Equation 2.3b is valid for the determination of the torsional OLS.

The calibration procedure requires knowledge of the cantilever spring constants, which may be determined from the same thermal noise spectra. The normal and torsional spring constants for rectangular cantilevers can be calculated based on the cantilever dimensions and the shape of PSD using Sader's equations:^{10, 74}

$$k_{z,Sader} = 7.525 \rho b^2 L Q v_{0,z}^2 \Gamma_i^z(v_{0,z}) \quad (2.4)$$

and

$$k_{\theta,Sader} = 6.285 \rho b^4 L Q v_{0,\theta}^2 \Gamma_i^{\theta}(v_{0,\theta}), \quad (2.5)$$

ρ is the fluid density (kg/m³), b and L are the width and length of the cantilever (m), respectively, and $\Gamma_i(v)$ is the imaginary component of the hydrodynamic function (dimensionless).⁷⁴ Since the detector effectively measures changes in the slope of the cantilever at the location of the laser spot rather than absolute displacements, as an improvement to Equation 2.3, typically a correction factor, $\chi_z = 1.19$, is included to account for the differences between flexural response (shape) of a free-loaded and end-loaded cantilever.⁷⁵⁻⁷⁷

$$OLS_z^{contact} = \sqrt{\frac{\chi_z (\langle A^2 \rangle - \langle A_0^2 \rangle) k_{z,Sader}}{k_B T}} = \sqrt{\frac{\pi A_{DC}^2 Q v_0}{2} \frac{\chi_z k_{z,Sader}}{k_B T}} \quad (2.6a)$$

The same considerations lead to analogous relationship for lateral parameters:

$$OLS_{\theta}^{contact} = \sqrt{\frac{\chi_{\theta} (\langle A^2 \rangle - \langle A_0^2 \rangle) k_{\theta,Sader}}{k_B T}} = \sqrt{\frac{\pi A_{DC}^2 Q v_0}{2} \frac{\chi_{\theta} k_{\theta,Sader}}{k_B T}} \quad (2.6b)$$

We will use $\chi_\theta = 1$ in calculations of S_θ below. This assumption appears plausible given that the torsional mode shape for the cantilever (dependence of the rotation angle θ of the cantilever on the distance x from clamped end for mode n) is given by $\theta(x) = C_0 \sin(\beta x)$, where $\beta = (2n-1)\pi/(2L)$ and C_0 is a constant. Thus, torsional angle θ is maximum at $x=L$ as is the case for the torsion induced by the tip placed at $x=L$.⁷⁸ According to Equations 2.1a and 2.1b, the overall cantilever sensitivity is then given by:

$$S_z = \frac{k_{z,Sader}}{OLS_z^{contact}} = \sqrt{\frac{2}{\pi A_{DC}^2 Q \nu_0} \frac{k_{z,Sader}}{\chi_z} k_B T} \quad (2.7)$$

with a similar equation for S_θ .

The presented calibration method assumes that the cantilever has a rectangular shape. It is clear from the scanning electron microscopy (SEM) images (see Figure 2.3), that the cantilevers used in our experiments do not have a rectangular cross-section nor shape (but rather a trapezoidal cross-section and a picket shape). It has been shown that a picket shaped cantilever with the added mass of a tip does not significantly differ from the behavior of an ideal, tipless rectangular cantilever.⁷⁹ For a practical experimental procedure, we would like to measure the cantilever dimensions using only an optical microscope. Figure 2.3d shows that the dimensions of the trapezoidal cross-section are readily evident using optical micrographs with oblique illumination, whereas the widest dimension is easily determined using either reflected or transmitted light observations. Use of a trapezoidal cross-section improves the estimates of the spring constants from cantilever dimensions,¹¹ although assumption of the negligible thickness in Sader's model implies that the widest dimension dominates the behavior described with Equation 2.4 and 2.5. Empirically, we found a close agreement between k_z values calculated in

Sader's approach using the greatest dimension for width and determined using the conventional approach based on the equipartition theorem.

Additionally, for LFM, one is interested in the friction (lateral) forces rather than torques. Therefore, one must find the lateral sensitivity factor, S_x , to convert the signal read from the split photodiode to forces. Since the torsional angle, θ , of the cantilever is imposed by the lateral force acting on a lever arm of length H (tip height + $\frac{1}{2}$ of the cantilever thickness, Figure 2.3a), the force microscope sensitivity due to lateral displacement of the tip, S_x , is related to the torsional sensitivity, detected as twisting of the cantilever, as:

$$k_x = \frac{k_\theta}{H^2} \quad \text{and} \quad S_x = \frac{S_\theta}{H} \quad (2.8)$$

In liquids, the SHO model represents the experimental thermal noise spectrum poorly, causing systematic errors in the spring constant calculation.⁸⁰ The thermal spectrum can be described correctly with a fluid-structure interaction model,^{81, 82} but the fitting procedure is often problematic or inaccurate in practice.⁸³ Pirzer and Hugel have shown that a Lorentzian:

$$A_{SM}^2(\nu) = \left(\frac{A_{DC}}{2} \right)^2 \frac{\nu_0^2}{(\nu - \nu_0)^2 + \left(\frac{\nu_0}{2Q} \right)^2} + A_0^2 \quad (2.9)$$

describes the shape of the PSD of cantilevers in viscous fluids (up to ~ 7 centipoise) quite well.⁷⁶ Although a Lorentzian fit is an empirical approach, fits of the experimental thermal noise spectrum of highly damped cantilevers display excellent agreement with fit results from a fluid-structure interaction model for cantilevers in liquids. Figure 2.2 shows a comparison of the fits to the SHO, Lorentzian, and fluid-structure interaction

models for a cantilever in water and ethylene glycol. In fact, a Lorentzian fit is almost indistinguishable from a fit to the physically sensible, but complex, fluid-structure interaction model. In order to calculate the cantilever deflection, the Lorentzian model may be integrated analytically, and the mean-squared thermal amplitude can be calculated using the fit parameters:

$$\langle A^2 \rangle - \langle A_0^2 \rangle = \frac{A_{DC}^2 Q v_0}{2} \left[\frac{\pi}{2} + \arctan(2Q) \right] \quad (2.10)$$

Whenever the SHO model breaks down, one can use this integrated intensity in place of the corresponding SHO values in formulas expressing OLS (Equation 2.6).

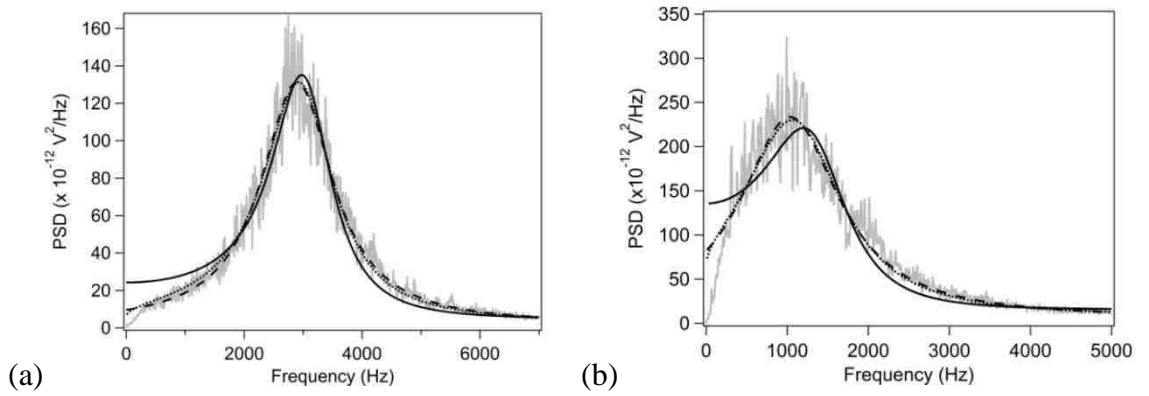


Figure 2.2. Fitting of the flexural thermal noise spectrum (grey) to the SHO (solid line), Lorentzian (dashed line), and fluid-structure interaction (dotted line) models for a rectangular silicon cantilever in water (a) and ethylene glycol (b) (Probe #1, Table 2.1)

Since the spring constants determined using Sader’s method have been shown to be quite close to those determined by a commonly accepted added mass method,¹² Equation 2.7 should be sufficient to fully calibrate forces in the microscope in air using thermal spectra only. We verified this conjecture with several cantilevers in different fluids at different temperatures by comparing the values of the S_z and S_x derived using the

method outlined above and values of the S_z and S_x found using commonly reported procedures.

2.3 Methods

The cantilevers used in the following experiments consist of a collection of rectangular silicon cantilevers, both with and without a metal reflective coating. The Cont and Cont Al model cantilevers are produced by Budget Sensors (Sofia, Bulgaria), CLR and FMR cantilevers are manufactured by Vista Probes (Phoenix, AZ), CSG10 cantilevers are made by NT-MDT (Moscow, Russia), and large radius probes with a nominal tip radius of 250 nm, LRCH-15, are produced by Team Nanotec GmbH (Phoenix, AZ).

All experiments were carried out on an MFP-3D-BIO atomic force microscope (AFM) retrofitted with an Enhanced LFM Head Option upgrade (Asylum Research, Santa Barbara, CA) either in an empty or liquid-filled fluid cell. The gaps between the quadrants (labeled clockwise A, B, C, and D from the upper left) in the photodiode detector of MFP-3D-BIO are aligned with the normal and lateral deflection axes in such a way that signal due to normal deflection is $(A+B)-(C+D)$ and signal due to lateral deflection is $(A+D)-(B+C)$. Cantilever plan view dimensions were measured using an Olympus CX-41 Microscope and a Hitachi 4300 (Krefeld, Germany) scanning electron microscope (SEM).^a The canonical normal force calibration procedure was completed by capturing force curves against a solid, incompressible surface (glass) in order to

^a Peng Cheng captured SEM images

determine the deflection sensitivity (OLS_z) followed by acquisition of a thermal noise spectrum.^{69, 84, 85} The thermal noise spectra were captured over the full frequency range of

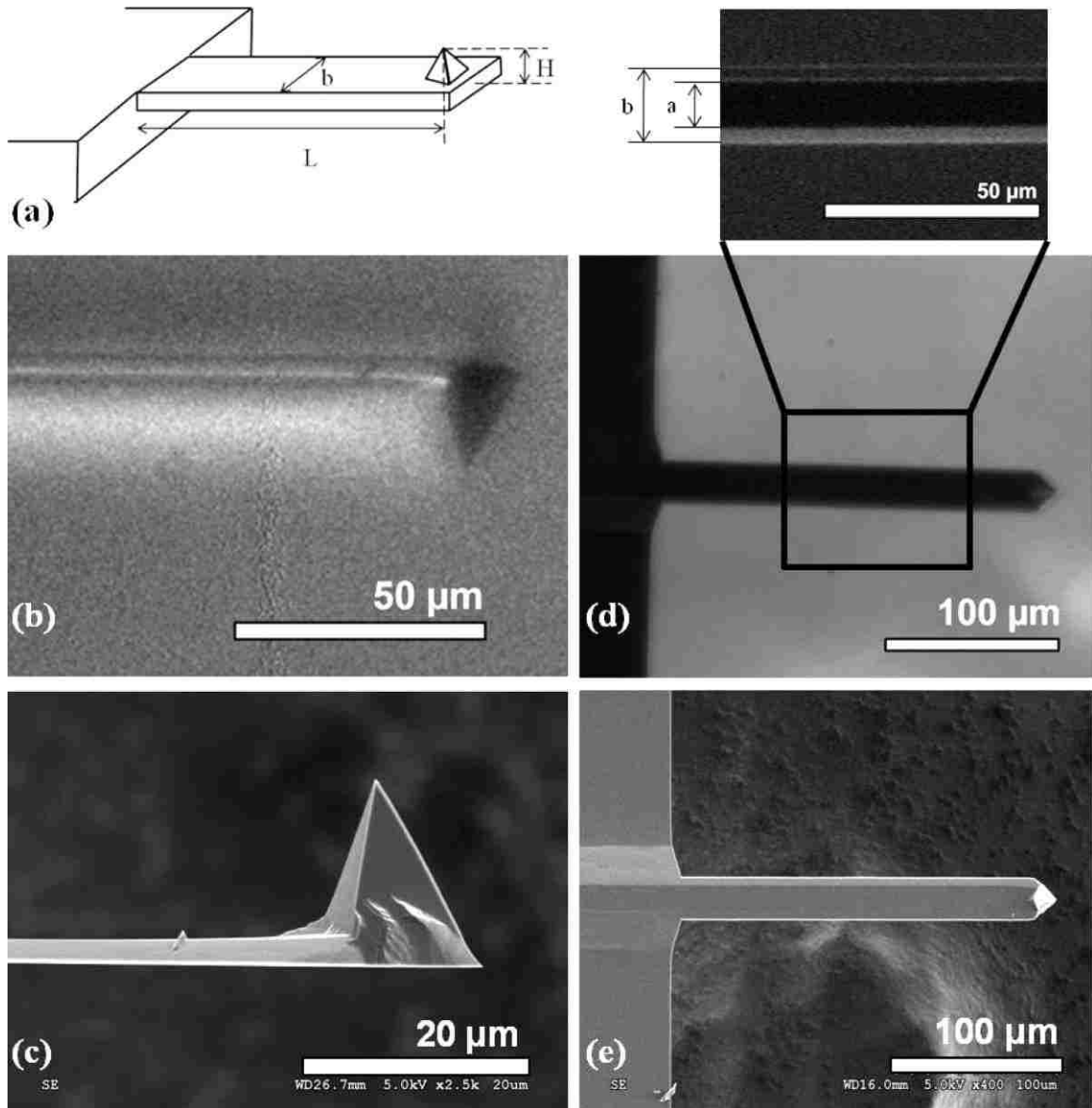


Figure 2.3. (a) Schematic view showing cantilever plan view dimensions for an ideal rectangular cantilever, (b) and (c) are the cantilever side view images using an optical microscope ($40\times$ objective) and SEM, respectively, and (d) and (e) are the top view images using an optical ($10\times$ objective) microscope and SEM, respectively. Inset to (d) shows a top-view image with lighting at an oblique angle to illuminate the trapezoidal cross-section ($20\times$ objective). (Probe #5, Table 2.1).

the AFM head/controller electronics (10 Hz to 2.5 MHz, although reliable data at the low frequency was limited to 300-400 Hz due to insufficient number of points for averaging at the long time intervals). The instrumental background noise was also measured on an immobile surface to ensure that correct values for background noise are found in the course of the fitting procedure (see section 2.6.1).

The value of OLS_z was found from the slope of the linear portion of the retraction force curve corresponding to tip-surface hard contact. The sensitivities determined from extension and retraction parts of the force curve agreed within <1% (*i.e.* axial friction effects were negligible). The PSD in air was fitted to a SHO model. The spring constant was calculated by inverting Equation 2.6:

$$k_z = \frac{2\chi_z OLS_z^2 k_B T}{A_{DC}^2 \pi Q v_0} \quad (2.11)$$

We compared our lateral thermal calibration method to the wedge calibration technique presented by Ogletree, Carpick, and Salmeron.⁶⁷ This method requires scanning an AFM probe across a sloped sample (we used a TGG01 calibration grating with a slope of $\pm 55^\circ$, MikroMasch, San Jose, CA). The lateral trace and retrace images ($4 \mu\text{m} \times 4 \mu\text{m}$ scan size with the slow axis scan disabled) were captured over a range of applied normal loads, L , to measure the changes in the friction loop width, W' , and friction loop offset, Δ' . The lateral sensitivity, S_x , was calculated according to the following equations:⁶⁷

$$S_x = \frac{(1 + \mu^2) \sin \varphi \cos \varphi}{\cos^2 \varphi - \mu^2 \sin^2 \varphi} \frac{1}{\Delta'} \quad (2.12)$$

or

$$S_x = \frac{\mu}{\cos^2 \varphi - \mu^2 \sin^2 \varphi} \frac{1}{W'} \quad (2.13)$$

where:

$$\mu + \frac{1}{\mu} = \frac{2\Delta'}{W' \sin 2\varphi} \quad (2.14)$$

μ is the friction coefficient, φ is the inclination angle of the surface (measured from the horizontal plane), and $\Delta' = \frac{\partial \Delta}{\partial L}$ and $W' = \frac{\partial W}{\partial L}$ are the rate of change of the friction force and friction offset with applied normal load, respectively. Details of the wedge calibration are shown in the Appendix.

2.4 Results and Discussion

To demonstrate broad applicability of the method, we carried out calibration experiments with several commercially available cantilevers that had a rectangular shape (silicon cantilevers, both with and without metal reflective coatings). Table 2.1 lists the cantilevers used and dimensions of their geometry. Several types of cantilevers were calibrated using multiple chips to show the reproducibility between experiments, different alignments, and different cantilevers. The selected cantilevers for this experiment are in common use for contact mode imaging and friction measurements. The cantilever length, width, and tip height (see Figure 2.3) were measured with an optical microscope using a 10 \times , 20 \times , or 40 \times magnification objective. For comparison, the same parameters as well as the cantilever thickness were measured using SEM. For most cantilevers, we found that the factory reported average dimensions for the cantilevers and tips provide reasonable estimates for calibration. On average, the measured probe

dimensions differed from the factory values by 2%, 7%, and 10% for the length, width, and tip height, respectively; however, the differences between the measured and reported dimensions can be significant for some cantilever models.

As a point of comparison, Table 2.1 also displays the theoretically calculated spring constants using the following equations:⁸⁶

$$k_z = \frac{3EI}{L^3} \quad I_{rect} = \frac{t^3 b}{12} \quad I_{trap} = I_{rect} \frac{1+a/b}{2} \left(1 - \frac{1}{3} \left(\frac{1-a/b}{1+a/b} \right)^2 \right) \quad (2.15)$$

and

$$k_\theta = k_z \frac{2L^2}{3(1+\gamma)} \quad (2.16)$$

I is the moment of inertia of the cantilever beam (having either rectangular or trapezoidal cross-section), E is Young's modulus of silicon (169 GPa for Si₁₁₀),⁸¹ t is the cantilever thickness, a and b are the widths of the two faces of the cantilever, and γ is Poisson's ratio of silicon (0.25).^{11, 87} In order to provide the most appropriate estimation of the theoretical k values, the SEM dimensions were used in the calculation presented in Table 2.1. If the a/b ratio does not deviate too much from 1, the correction due to the trapezoidal shape is small and, for most cantilevers used here, accounts for ~10-15% change from the k_z value of a rectangular beam. On the other hand, we found that thickness values determined from the SEM images are accurate to within 5-10% (see two different trials for SEM imaging in Table 2.1), thus, having the error that could translate into 15-30 % uncertainty in k_z . Alternatively, one can use the resonant frequency in air to estimate the total mass and, therefore, the thickness of the cantilever (see section 2.6.3). These two independent estimates of the cantilever thickness agree well and values of k_z

Probe	Model	L μm	a μm	b μm	H μm	L μm	a μm	b μm	t _{final1} μm	t _{final2} μm	H μm	V ₀ kHz	(from v ₀) μm	k _z N/m	k _θ nN m rad ⁻¹	Material/ Coating
1	Cont	453	44	52	15	- ^a	43.2	53.5	1.93	2.11	- ^a	12.40	1.91	0.154	16.8	Si / none
2	Cont	453	44	51	16	454	43.1	52.9	2.11	2.05	16.9	12.14	1.88	0.144	15.8	Si / none
3	ContAl	450	40	47	14	454	39.8	48.5	1.82	1.77	15.9	11.40	1.76	0.109	12.0	Si / Al
4	ContAl	451	40	46	15	453	37.8	47.6	1.71	1.85	15.7	11.31	1.74	0.103	11.2	Si / Al
5	FMR	222	14	23	16	220	13.6	23.8	1.80	2.08	15.4	46.37	1.87	0.470	12.1	Si / Al
6	CLR	451	25	36	15	442	26.2	34.0	1.68	1.70	15.8	8.58	1.30	0.0321	3.35	Si / Al
7	CSG10	220	27	30	12	220	28.9	31.3	0.71	0.87	11.6	15.01	0.58	0.0238	0.615	Si / Al
8	LRCH	457	- ^b	17	18	458	16.2	18.2	3.90	- ^b	18.7	21.56	3.50	0.325	36.4	Si / Al
9	ContAl	449	36	52	16							9.84	1.52	0.103	11.1	Si / Al

^a Probe #1 was partially damaged before SEM images could be captured.

^b Probe # 8 was damaged before the second trial of thickness determination.

obtained using either SEM or resonance derived thickness showed an excellent correlation with those derived from Sader's or equipartition theorem methods (see Table 2.1 and Table 2.2). The values for the torsional spring constant found from Equation 2.16 generally agreed well with values from Sader's method (Table 2.5) with only two probes (#1 and # 8) showing significant deviations.

2.4.1 Noncontact Calibration of the Normal Cantilever Sensitivity

As shown in Figure 2.1, we routinely observed good isolation and low cross-talk between the flexural and torsional thermal noise spectra for rectangular cantilevers. First, we demonstrated excellent agreement for the determination of the OLS_z obtained from the noncontact method (using Equation 2.6) and from direct measurements using force-distance curves in air. Figure 2.4a shows a typical flexural noise spectrum of a rectangular silicon cantilever and includes a fit to Equation 2.2. The fit parameters for all cantilevers and the resulting flexural spring constant determined from the Sader calculation, k_{Sader} , are shown in Table 2.2 along with the flexural spring constant, k_z , determined through the standard calibration method (*i.e.* recording force curves, finding OLS, and analyzing the thermal noise spectrum by Equation 2.11) for comparison.

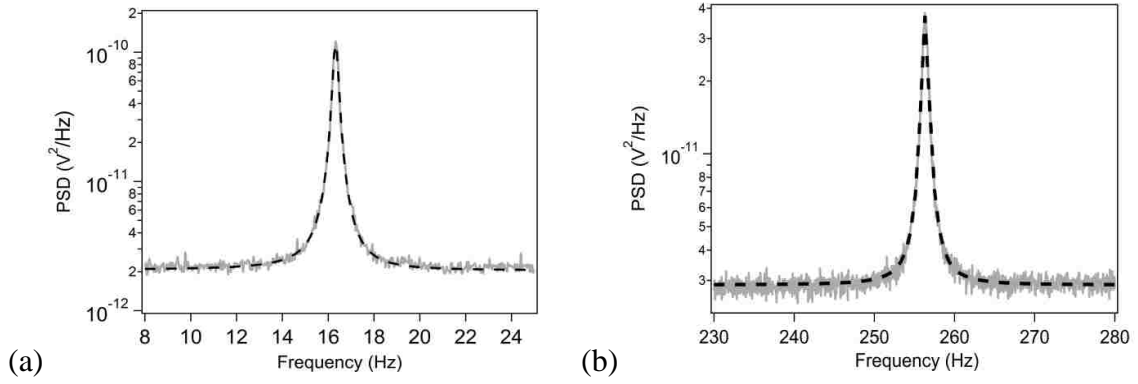


Figure 2.4. Flexural noise spectrum (a) and torsional noise spectrum (b) of a rectangular silicon cantilever (Probe #1, Table 2.1) in air. The dashed lines correspond to the fit to Equation 2.2.

Table 2.2. List of fit parameters in SHO model for flexural calibration of AFM cantilevers in air (viscosity $\eta_{\text{air}}=1.86\times 10^{-5}$ Pa·s, and density $\rho_{\text{air}}=1.18$ kg m⁻³). $\text{OLS}_z^{\text{contact}}$ was calculated using Equation 2.6 ($\chi_z = 1.19$).

Probe	A_{DC}^2 $\times 10^{-14}$ V ² /Hz	ν_0 kHz	Q	k_{Sader} N/m	k_z N/m	$\text{OLS}_z^{\text{contact}}$ mV/nm	OLS_{FC} mV/nm	S_z nN/V	$S_{z,\text{FC}}$ nN/V
1	23.20	12.40	51.9	0.167	0.161	3.35	3.27	49.9	49.2
2	15.31	12.14	48.5	0.146	0.152	2.45	2.50	59.6	60.8
3	156.7	11.40	42.0	0.107	0.108	6.02	6.12	17.8	17.6
4	297.7	11.31	42.4	0.0861	0.0804	7.45	7.89	11.6	10.2
5	12.47	46.37	96.3	0.493	0.449	11.1	10.6	44.4	42.4
6	1743	8.583	24.2	0.0352	0.0401	7.60	7.94	4.63	5.05
7	3468	15.01	24.3	0.0321	0.0283	13.2	12.9	2.43	2.19
8	9.054	21.56	119	0.371	0.368	6.24	6.23	59.5	59.1

Overall, the experimental spring constants in Table 2.2 are in reasonable agreement with the theoretical values displayed in Table 2.1. Differences between the experimental and theoretical values may be a result of the cantilever geometry (*i.e.* the cantilever has a trapezoidal and picket shape instead of a rectangular shape).⁸⁶ Table 2.2 also compares the $OLS^{contact}$ of the cantilevers measured in air using k_{Sader} and Equation 2.6 to the $OLS^{contact}$ directly measured from force curves, OLS_{FC} . The OLS determined using the noncontact method agreed well with values obtained using force-distance curves (within 3% on average, although up to 6% difference could be observed for individual cantilevers). Corresponding S_z sensitivities derived with noncontact and contact methods were also very close (5% average error). Our results have a greater agreement between these two approaches than previously reported by Higgins *et al* (within 13% on average) likely due to the use of measured cantilever dimensions rather than nominal factory cantilever dimensions in the calculation of the spring constant. The presence of a thin, reflective metal coating on the backside of the cantilever has little or no effect on skewing the cantilever sensitivity from the expected values. Others have shown the effects of a reflective coating on the cantilever by considering the added layer mass and density, but the correction factor is small.⁸⁷ We found that the thermal spectra in air could also be fitted with the Lorentzian model and both the SHO and Lorentzian fits provide very similar values for the resonance frequency, Q-factor, and peak area (as expected for high Q systems).

Table 2.3. Flexural OLS determined in various fluids using a Lorentzian fit for a rectangular silicon cantilever (Probe # 1, Table 2.1). OLS_z^{contact} was calculated using Equation 2.6a ($\chi_z = 1.19$).

Fluid		η $\times 10^{-5}$ Pa·s	ν_0 kHz	Q	A_{DC}^2 $\times 10^{-10}$ V ² /Hz	OLS_z^{contact} V/nm	OLS_{FC} mV/nm	S_z nN/V	$S_{z, FC}$ nN/V
Air		1.86	12.4	51.9	-	3.35	3.27	49.9	49.2
Water	Ethylene Glycol								
1	0	89	2.89	1.98	0.231	3.05	2.89	54.8	55.7
0.75	0.25	150	2.51	1.54	0.314	2.88	2.71	58.0	59.5
0.50	0.50	280	2.11	1.15	0.968	3.95	3.53	42.3	45.6
0.25	0.75	683	1.57	0.835	1.96	4.01	3.82	41.6	42.2
0	1	1400	1.00	0.619	4.17	3.92	3.83	42.6	42.0

2.4.2 Noncontact Calibration of the Normal Cantilever Sensitivity in Liquids

Force spectroscopy experiments are often carried out in a liquid environment rather than air, and, therefore, we evaluated the performance of this calibration technique in viscous fluids using a Lorentzian fit to calculate $\langle z^2 \rangle$. As shown in Figure 2.2, the SHO model begins to break down in viscous liquids and the shape of the thermal noise spectrum is approximated by a Lorentzian fit much better than by a SHO fit. In liquids, the resonance frequency shifts to lower frequencies due to the added mass of the liquid dragged by the cantilever.⁸⁸ Table 2.3 shows the effect of strong damping on the resonance frequency and the Q factor in various mixed two-component liquids composed of ethylene glycol and water. The Sader technique for the calibration of spring constants is accurate if the Q-factor is $\gg 1$, but in liquids the Q-factors for typical cantilevers are

decreased to near or below 1. The strong damping may be accounted for on the thermal spectrum by incorporating a more detailed model of the cantilever-fluid interaction (*i.e.* fluid-structure interaction model).

We opted to modify our procedure for experiments in liquids by first determining the spring constant in air followed by a measurement of the OLS in fluid. The exchange of liquid in the fluid cell only changes the OLS due to changes in alignment (*i.e.* changes in conditions for laser beam refraction at interfaces between the fluid and walls of the cell), whereas the cantilever spring constant should not be affected. Therefore, we can measure a thermal noise spectrum of the cantilever in air to calculate an appropriate spring constant value (since the resonance frequency is close to the natural frequency and $Q \gg 1$), followed by a second measurement of the thermal noise spectrum in liquid to determine the actual OLS for a given setup (since only the integrated power is needed for the second step). The second thermal noise spectrum accounts for any adjustments in the optical alignment encountered due to new conditions along the beam path in the fluid cell. Table 2.3 shows the effectiveness of our two-step calculation to determine the OLS_z with a comparison to OLS_{FC} from forces curves. In Table 2.3, we used a fixed k_{Sader} (found from the thermal PSD in air) for the OLS_z calculation in all other fluids. Agreement between the S_z values determined using the two methods is within 3 % on average for this system.

[REDACTED]

°C	$\times 10^{-5}$ Pa•s	kg/m ³	kHz	Q	$\times 10^{-6}$ V ² /Hz	mN/m	mN/m	mV/nm	mV/nm	mV/nm	nN/V	nN/V
25	89.0	997	2.45	1.71	4.28	85.2	92.8	10.3	11.2	11.2	8.30	8.26
30	79.8	996	2.51	1.85	4.50	89.9	91.2	10.7	11.3	11.3	8.38	8.08
40	65.3	992	2.60	1.94	5.17	88.5	92.3	11.2	11.9	11.9	7.89	7.73
50	54.7	988	2.68	2.20	5.10	95.2	96.5	11.4	11.9	11.9	8.36	8.11
60	46.6	983	2.75	2.23	5.90	91.5	93.2	11.8	12.4	12.4	7.74	7.53
70	40.4	978	2.79	2.44	5.83	94.8	97.5	11.8	12.4	12.4	8.05	7.89
80	35.5	972	2.86	2.58	2.07	97.2	96.6	7.01	7.2	7.2	13.9	13.4

[REDACTED]

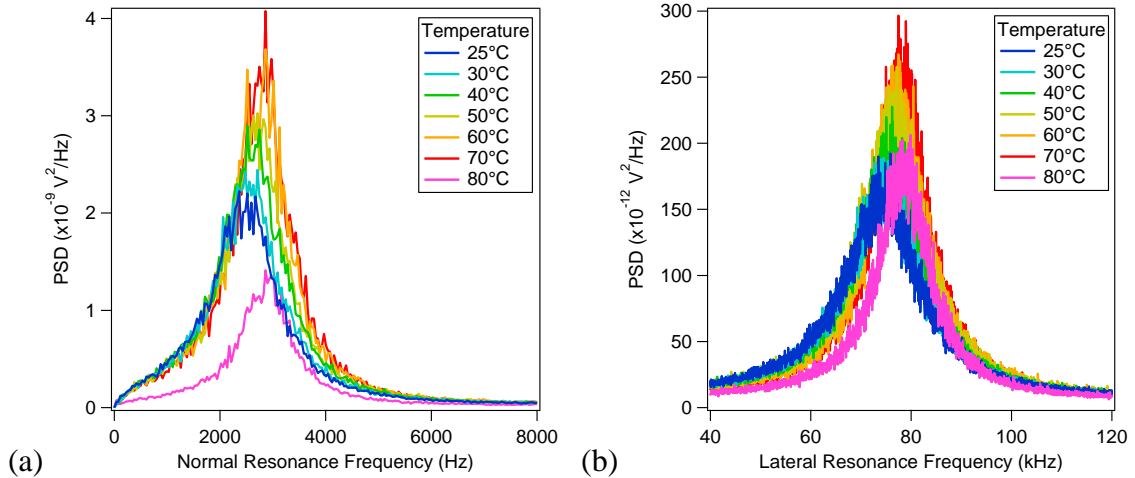


Figure 2.5. Flexural noise spectrum (a) and torsional noise spectrum (b) of a rectangular silicon cantilever (Probe #9, Table 2.1) in water 25-80°C. The dramatic shift in the amplitude of the resonance peak at 80°C is due to optical realignment of the laser spot on the cantilever (a change in the alignment effects the optical path).

2.4.3 Noncontact Calibration of the Normal Cantilever Sensitivity at Elevated Temperature

From the equipartition theory, it is clear that the mean cantilever fluctuations are dependent upon the thermal energy (*i.e.* temperature of the surrounding fluid). Using a thermally controlled fluid cell, we verified that the calculation of the spring constant (using Equation 2.4) and normal sensitivity (using Equation 2.6 and 2.10) is consistent in water between 25-80°C. In order to correctly calculate the spring constant and normal sensitivity, one must also account for the changes in fluid density and viscosity over this temperature range (Table 2.4). Figure 2.5 shows the shift in the flexural resonance peak as a function of temperature. As expected, an increase in temperature increases the resonance frequency and Q. It should be noted that the change in magnitude of the thermal resonance at 80°C is strictly due to optical realignment of the laser position on the cantilever due to thermal drift in the optical path (however, this optical realignment

did not affect the calculation of the spring constant, but the OLS and sensitivity is expected to change). Table 2.4 displays the measured values of the spring constant and normal sensitivity and compares our noncontact calibration procedure to the thermal calibration procedure using Equation 2.11. It is possible for the flexural sensitivity to change with temperature due to changes in the optical beam path due to thermal expansion of the tip holder, however, k_z will remain constant over this temperature range. Within error, the normal sensitivity of both methods closely agreed, showing that our noncontact normal calibration procedure is valid over a large range of temperatures commonly used in force spectroscopy experiments.

2.4.4 Noncontact Calibration of the Lateral Cantilever Sensitivity

Next, we applied a similar approach to the calibration of lateral forces. Figure 2.4b shows a typical torsional thermal tune for a rectangular silicon cantilever in air, where a SHO model (Equation 2.2) still maintains a good fit for the torsional resonance peak. As mentioned above, our noncontact calibration procedure using Equation 2.7 results in the value for the torsional sensitivity, S_θ , but we are interested in obtaining the lateral sensitivity, S_x . It is possible to convert between the two sensitivity factors by using the tip height (Equation 2.8), therefore, knowledge of the precise tip height is the principle source of error in the determination of the lateral sensitivity. We measured the tip height for each cantilever using an optical microscope and compared the measurements to SEM images (Table 2.1). We found that the measured SEM tip height typically differs by ~10% from nominal factory values, but optical microscope measurements are typically within 5% from SEM dimensions, and, therefore, are quite

adequate for the majority of situations found in LFM. Table 2.5 shows the lateral sensitivities for several probes compared to the lateral sensitivity determined by the wedge calibration method.

We noted a greater agreement between the two methods of the lateral sensitivities measured for cantilevers with a lower lateral spring constant (*i.e.* <30 N/m) than for probes with high spring constants. For stiffer cantilevers, large differences between the two sides were observed or the negative slope of the wedge did not provide useable data (*i.e.* friction offset did not decrease with increased load as expected for $\varphi < 0^\circ$, see Equation 2.14).⁶⁷ We also observed that repeated scanning of the wedge caused damage to the tip as noted by irregular or rough images after several wedge calibration experiments. Typically, worn or damaged tips could not produce data for negative slopes of the wedge that were amenable to use with Equation 2.14.

Overall, we found fair agreement between the sensitivities determined from thermal resonance and the wedge methods, with the values obtained with the two approaches differing by 36% on average (although sensitivities for some individual cantilevers could disagree by as much as a factor of two). Use of theoretical (Equations 2.15 and 2.16) lateral spring constants calculated from cantilever dimensions (Table 2.1) produced similar results for S_x (36% average error). For cantilevers of different type, sensitivity factors found in the noncontact method followed trends observed with results from the wedge method very closely. For the same probe, complete realignment and repeated calibration (denoted in the Table 2.5 as trials A and B for Probes #1 and #3) were within 14 % in both cases. The uncertainty in the wedge calibration has been estimated at approximately a 15% error.¹⁴ Given that the reproducibility of the lateral

calibration with either contact or noncontact method is worse than for the corresponding flexural sensitivities, it is not surprising to see a much poorer agreement between the two calibration methods for lateral forces than for normal forces discussed above. More importantly, the steep slope of the commercial wedge standard (tips with typical half-angle of 20-25° moving on 55° slope) could have rendered some assumptions behind the wedge model invalid. Indications of this potential problem come from variable friction force while moving on the nominally uniformly sloped surface and from our inability to obtain meaningful wedge calibration data for tips on downward slopes. Use of custom made calibration samples^{67, 89} having much smaller slope angles could result in better agreement. Additionally, we confirmed that, as expected at low loads, the lateral OLS obtained from the stiction portion of the friction loops (50 nm scans on mica) was lower by 30-50% than the values determined using this noncontact method.

Table 2.5. List of fit parameters in SHO model for lateral calibration of AFM cantilevers in air ($\chi_\theta = 1$, $\eta_{\text{air}} = 1.86 \times 10^{-5} \text{ Pa}\cdot\text{s}$, and $\rho_{\text{air}} = 1.18 \text{ kg m}^{-3}$).

Probe	Trial	ν_0 kHz	Q	A_{DC}^2 $\times 10^{-14} \text{ V}^2/\text{Hz}$	$k_{\theta, \text{Sader}}$ nN·m/rad	$k_{x, \text{Sader}}$ N/m	$S_{x, \text{Thermal}}$ nN/V	S_{Wedge}	S_{Wedge}
								+55° nN/V	-55° nN/V
1	A	256.3	299.3	0.1250	25.0	104	1690	966	-
1	B	256.3	289.0	0.1702	24.2	101	1450	1020	-
2	A	201.1	206.8	0.1569	11.4	47.5	1380	652	1130
3	A	200.0	188.1	2.552	8.09	40.1	331	153	-
3	B	200.0	187.8	2.433	8.08	40.1	339	174	67.1
4	A	198.1	185.9	3.345	7.77	34.5	271	197	-
5	A	897.6	311.5	0.3351	7.41	28.2	281	369	273
6	A	243.5	138.9	15.71	3.72	17.0	91.6	112	54.8
7	A	227.4	80.40	73.22	0.603	4.48	29.6	38.8	48.0
8	A	636.5	606.1	0.06070	8.72	26.6	546	673	581

2.4.5 Noncontact Calibration of the Lateral Cantilever Sensitivity in Liquids

Many force spectroscopy experiments are carried out in water and other fluids, so a calibration technique that is useful and accurate in air and fluid is important for proper calibration. In general, lateral sensitivity calibration is difficult in fluid and often not seen in practice using traditional wedge calibration methods,⁹⁰ therefore, a direct, fast, and encompassing lateral sensitivity calibration method for all fluids will be a valuable tool for friction force microscopy. Figure 2.6 shows an example of the torsional thermal noise PSD of a rectangular silicon cantilever (Probe #4, Table 2.1) in water. As observed for the flexural noise spectra in water, the fluid causes the fundamental resonance to be shifted to a lower frequency and the peak to broaden significantly (Q drops by almost two orders of magnitude). In order to accurately determine the torsional spring constant, a torsional thermal spectrum in air was used to calculate the torsional and lateral spring constants using Sader's method (Equation 2.5). Table 2.6 shows the results of the lateral calibration for several cantilevers in water. Similar to the flexural calibrations above, the Lorentzian model in liquids does not provide physically meaningful parameters for determination of the spring constants from Sader's calculation and we used thermal spectra in air to derive the most appropriate parameters (ν_0 and Q) for estimation of the torsional spring constants from Equation 2.5. Overall, the lateral sensitivities in air shown in Table 2.5 track quite reasonably to those determined using the wedge or noncontact method as shown in Table 2.6, but it is difficult to make a direct comparison of the final sensitivities since these two sets of measurements were not carried out within the same experiment (*i.e.* used different optical alignments).

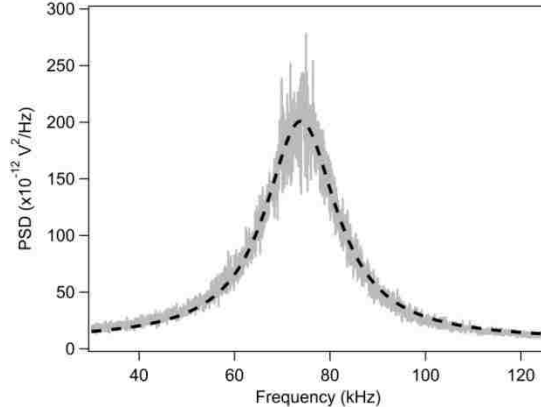


Figure 2.6. Example of a torsional noise spectrum of a rectangular silicon cantilever (Probe #4, Table 2.1) in water. Dashed line corresponds to the fit to Equation 2.9.

As seen from the data in Table 2.6, the lateral sensitivity drops noticeably when a liquid is introduced into the system. To date, the best attempt to account for calibration differences in air and fluid was presented by Tocha *et al.*, in which a ray-tracing model was developed to account for the refraction of the beam at the fluid/glass/air interfaces for calibrations of normal and lateral sensitivities.⁹⁰ The relationship obtained in that work for adjustment of the lateral sensitivity due to the presence of a liquid was:

$$\frac{S_{x,air}}{S_{x,fluid}} = \frac{n_{fluid}}{n_{air}} \quad (2.17)$$

Here, n_{fluid} and n_{air} are the refractive indices of the fluid (*i.e.* water $n=1.33$ and ethanol $n=1.36$) and air ($n=1.00$). As predicted by Equation 2.17, we observed that the addition of the fluid medium (water or ethanol) did decrease the lateral sensitivities; in our case, experimentally, $S_{x,air}/S_{x,fluid}$ was approximately 1.6 ± 0.3 . Using our sloped calibration grating in liquids, however, we were not able to obtain robust friction data amenable to numerical treatment in the wedge calibration method.

2.4.6 Noncontact Calibration of the Lateral Cantilever Sensitivity at Elevated Temperature

Finally, we measured the lateral spring constant in water at temperatures ranging from 25-80°C. Similar to our observations of the flexural spring constant and sensitivity, we found that the calculated lateral spring constant was consistent over the measured temperature range, but the lateral sensitivity varied with temperature. Figure 2.5b displays the effects of temperature on the torsional resonance peak – the torsional resonance and Q increase with temperature. Table 2.7 displays the calculated lateral sensitivity values in water. The consistency in these results show that our calibration method is robust in most experimental conditions used in force spectroscopy experiments.

2.5 Conclusions

We described a convenient one-step *in situ* AFM cantilever calibration procedure that is applicable for the calibration of the lateral forces for rectangular cantilevers in air. Furthermore, calibration in liquids uses a similar two-step procedure (the extra step determines the spring constant) that is rapid, easy to implement on most current commercial AFMs, and does not require contact with the sample, therefore, avoiding the use of specialized calibration gratings. We showed applicability of this calibration technique for experiments in viscous fluids by using a thermal spectrum in air to determine k and a Lorentzian fit to approximate the shape of the spectra in liquid to calculate $\langle z^2 \rangle$ or $\langle \theta^2 \rangle$. The main source of error in the flexural and lateral sensitivity calibration arises from inaccurate knowledge of the cantilever dimensions and the tip

Table 2.6. List of fit parameters to Lorentzian model (in liquids) and SHO model (in air) for lateral calibration of AFM cantilevers in liquids. ($\chi_\theta = 1$)

Probe	Fluid	ν_0 kHz	Q	A_{DC}^2 $\times 10^{-13} \text{ V}^2/\text{Hz}$	$k_{\theta, \text{Sader}}$ nN·m/rad	k_x, Sader N/m	$S_x, \text{Thermal}$ nN/V
4	Water	73.9	4.16	1920	8.06	35.8	169
4	Air	198	193	0.316			279
6	Water	113	3.44	1450	4.98	22.7	114
6	Air	280	154	0.431			179
7	Water	67.3	2.49	8910	0.606	4.50	22.9
7	Air	227	80.8	4.34			38.5
7	Ethanol	70.9	2.10	3960	0.707	5.25	33.4
7	Air	227	84.3	4.86			38.5
8	Ethanol	447	5.98	108	9.07	28.0	306
8	Air	637	631	5.70×10^{-4}			566

Table 2.7. Lateral sensitivity determined in water between 25-80°C using a Lorentzian fit for a rectangular silicon cantilever (Probe # 9, Table 2.1). Refer to Table 2.4 for water viscosities and densities ($\chi_\theta = 1$).

Temperature °C	ν_0 kHz	Q	A_{DC}^2 $\times 10^{-12} \text{ V}^2/\text{Hz}$	$k_{\theta, \text{Sader}}$ nN·m/rad	k_x, Sader N/m	$S_x, \text{Thermal}$ nN/V
25	74.1	4.13	8.80	10.0	37.6	6170
30	74.6	4.28	8.46	9.92	37.3	6180
40	75.5	4.69	8.04	10.0	37.6	6140
50	76.4	5.07	7.94	10.1	38.0	6020
60	77.1	5.40	7.28	10.0	37.6	6120
70	77.8	5.93	6.63	10.4	39.1	6300
80	78.5	6.26	4.39	10.4	39.1	7600

height. Use of the manufacturer specifications for probe dimensions can be a reasonable approximation for the calibration of most cantilevers, but could cause errors in some cases when the actual cantilever/tip dimensions are much different than the nominal values. We found that actual dimensions for the cantilever and tip can be obtained with sufficient accuracy using an optical microscope readily accessible in most research laboratories. The aforementioned calibration technique should also be suitable for cantilevers carrying colloidal probes.

The method has few limitations; calibration can only be performed on relatively compliant cantilevers with a low torsional resonance frequency (*i.e.* the torsional resonance must fall within the available bandwidth of the instrument). Cantilever dimensions should be suitable for application of Sader's method, *i.e.* the cantilever must have a high length-to-width aspect ratio. Typical cantilevers used in force spectroscopy and friction measurements fall into this category. The ease of implementation of this lateral calibration should allow its wide-spread adoption in quantitative measurements of friction forces with an AFM.

2.6 Appendix

2.6.1 Thermal Spectrum Baseline Instrumental Noise

In order to determine the baseline noise level of the thermal noise spectrum, we captured thermal spectra with the AFM laser spot centered on the backside of the cantilever chip. It is assumed that the thick cantilever chip is a stiff, reflective substrate that has no thermally excited oscillations. Since the chip is more reflective than the cantilever arm, the change in the measured detector sum was accounted for by dividing

the chip PSD spectra by the ratio of the sum value of the reflected diode from the chip and the cantilever, *i.e.*:

$$PSD_{chip}^{corrected} = PSD_{chip}^{raw} \left(\frac{Sum_{cantilever}}{Sum_{chip}} \right)^2 \quad (2.18)$$

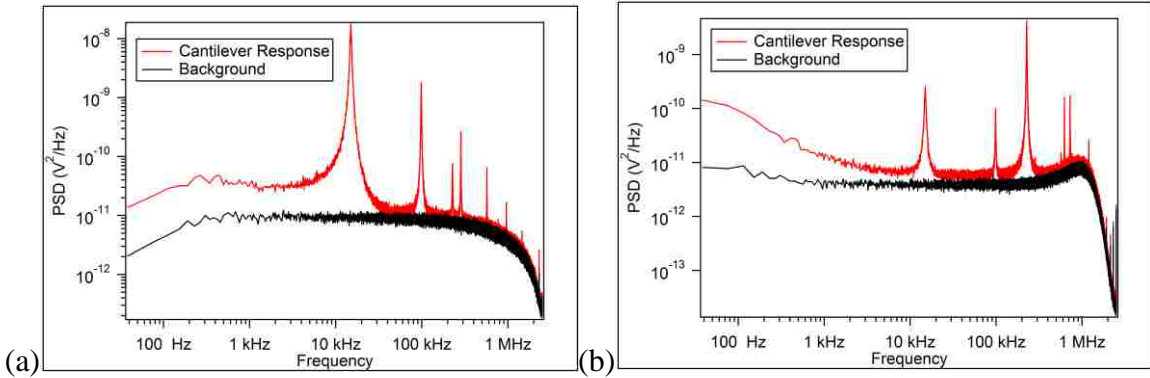


Figure 2.7. Thermal spectrum background noise for the flexural response (a) and torsional response (b) in air (Probe #7, Table 2.1). The black curves are due to background noise and the red curves are experimentally measured cantilever noise.

Figure 2.7 displays the background noise with the measured thermal noise for the flexural and lateral spectra in air of Probe #7 (Table 2.1). We found excellent agreement between experimental noise floor values and those obtained from fitting.

2.6.2. Example Calculation for Wedge Calibration Method

We followed the wedge calibration procedure originally proposed by Carpick, Ogletree, and Salmeron.⁶⁷ For the wedge calibration method we imaged calibration standard TGG01 produced by MikroMasch USA (San Jose, CA) in contact mode with a scan angle of 90 degrees under several applied normal loads. Each captured image corresponded to one applied normal load on the sample, and 5 images were captured to

create the plot of the lateral response as a function of load. For every image, the trace and retrace directions were recorded for the height, Z-sensor, deflection, and lateral channels with no data offsets or modifications. The Z-sensor channel was used to determine the slope of the wedge surface (54.9° on the left hand side and -53.7° on the right hand side). Figure 2.8 shows a sample image obtained for a Probe #5 (Table 2.1) with an applied normal load of 65.2 nN.

From Figure 2.8, we measured the friction force ($W=[F_x(\text{trace}) - F_x(\text{retrace})]/2$) and the friction offset ($\Delta=[F_x(\text{trace}) + F_x(\text{retrace})]/2$) at each load. Figure 2.9 plots the resulting friction force, W , and offset, Δ , as a measure of the lateral detector response (each data point corresponds to the averaged lateral response over all scan lines at each load and the error bars corresponds to the standard deviation). The slope of the friction force, W' , and friction offset, Δ' , is then used to determine the lateral sensitivity, S_x :

$$S_x = \frac{(1+\mu^2) \sin \varphi \cos \varphi}{\cos^2 \varphi - \mu^2 \sin^2 \varphi} \cdot \frac{1}{\Delta'} \quad (2.19)$$

and

$$S_x = \frac{\mu}{\cos^2 \varphi - \mu^2 \sin^2 \varphi} \cdot \frac{1}{W'} \quad (2.20)$$

where μ is the friction coefficient:

$$\mu + \frac{1}{\mu} = \frac{2\Delta'}{W' \sin 2\varphi} \quad (2.21)$$

and φ is the inclination angle of the surface (measured from the horizontal plane). Table 2.8 displays the calculated values from the above equations for Probe #5.

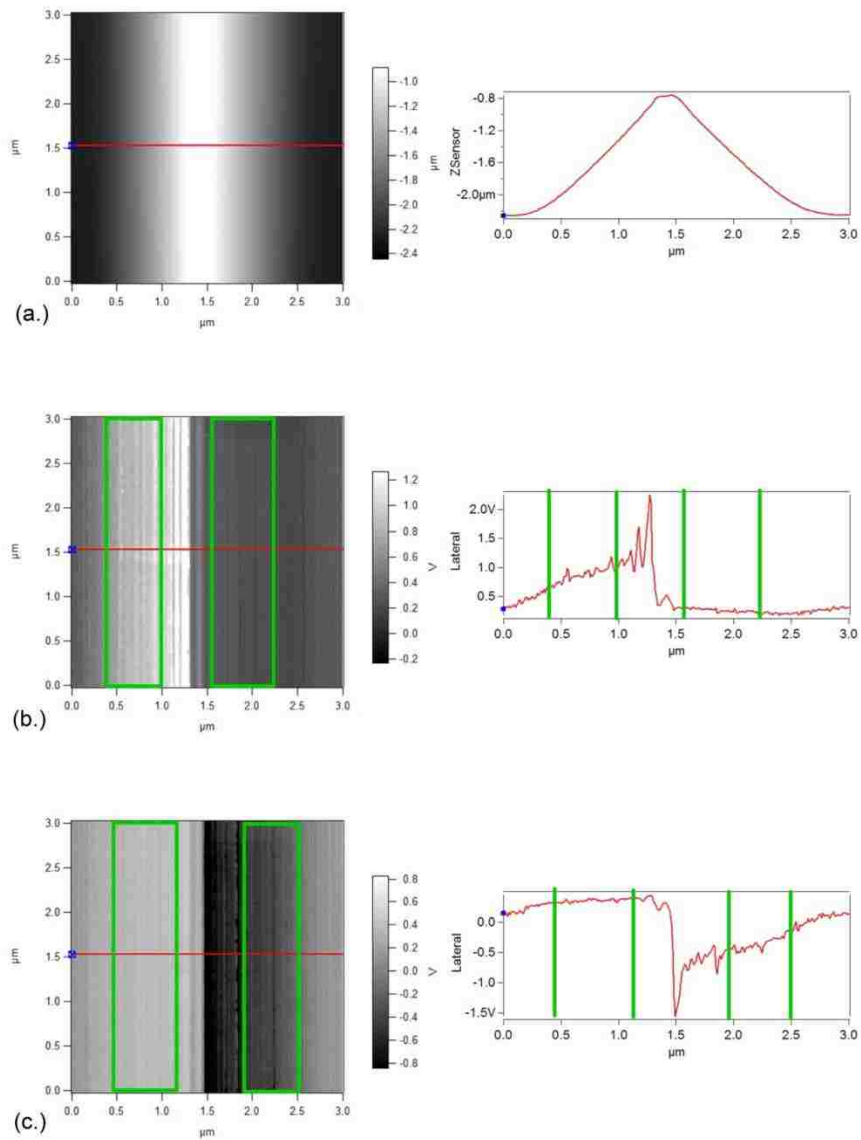


Figure 2.8. Sample images of the Z-sensor (a), lateral trace (b) and retrace (c) channels with their accompanying cross-sectional plots. For the lateral images, the area inside of the green squares were used for calculations.

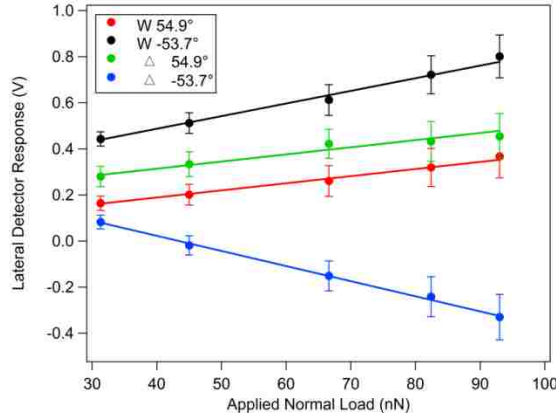


Figure 2.9. Friction force and friction offset as a function of applied normal load. Error bars correspond to the standard deviation at each load.

Table 2.8. Results of example calculation of the lateral sensitivity using the wedge calibration procedure (Probe #5, Table 2.1).

Parameter	Slope = 54.9°	Slope = -53.7°
W' (nN/V)	0.00285	0.00242
Δ' (nN/V)	0.00503	-0.00569
μ	0.289	0.212
S_x (Equation 2.19) (nN/V)	370	273
S_x (Equation 2.20) (nN/V)	369	273

2.6.3 Calculation of the Cantilever Thickness from the Natural Frequency

The thickness of the cantilever can be found from the natural frequency ν_0 (approximated as the resonance frequency in air) as:

$$\nu_0 = \frac{1}{2\pi} \sqrt{\frac{k_z}{(3/\alpha_i^4)m_{cantilever} + m_{tip}}} \quad (2.22)$$

$\alpha_1=1.875$, $\alpha_2=4.694$, ... $\alpha_i=(i-1/2)\pi$ for i -th mode. Depending on the dimensions of the cantilever, the contribution of the tip mass to the total effective mass ranged between 7%

and 30% for the cantilevers we used. Approximating the tip as a cone with half-angle φ ($\varphi = 20^\circ - 25^\circ$ reported by most manufacturers), we obtain:

$$\frac{1}{(2\pi\nu)^2} = \frac{L^3}{3EI} \rho_{cantilever} \left(\frac{3}{\alpha_t^4} L \frac{a+b}{2} t + \frac{\pi}{3} H^3 \tan^2 \varphi \right) \quad (2.23)$$

which is a cubic equation that one can solve numerically for thickness t . Experimental k_z values found in both equipartition and Sader approaches correlated closely with the theoretical values found from Equation 2.15 and thickness values found using Equation 2.23 (Figure 2.10).

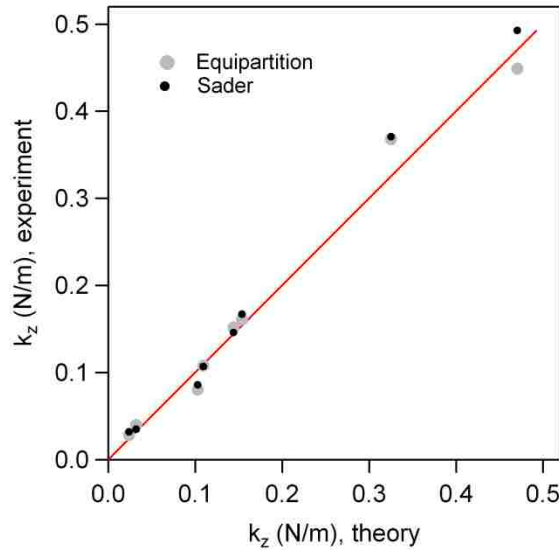


Figure 2.10. Correlation between experimentally determined spring constants and corresponding values calculated based on material properties and dimensions of the cantilevers.

2.6.4. Lateral sensitivity measured using stiction portion of friction loops

As an additional point of comparison, we also measured the lateral OLS from friction loop images on mica and silicon for several cantilevers. It was previously proposed that rapid scanning over a small area is capable of displaying stick-slip motion in the friction measurement. It was originally thought that if the slope of the turnaround

portion of the friction loop (due to stiction) was equivalent to the OLS_x (similar to the measurement of OLS_z). However, it was later determined that the stiffness of contact between the probe and the sample is comparable to the stiffness of the probe, thus, leading to inaccurate estimates of OLS_x .⁶⁶ The lateral OLS for both procedures were measured with the same optical alignment for each cantilever, thus eliminating differences due to the optical path. Figure 2.11 shows an example of a friction loop for probe 4 on mica. Table 2.9 summarizes the results OLS_x results measured by friction loops on mica. It is expected that the OLS from friction loops should underestimate the actual OLS of the cantilever.

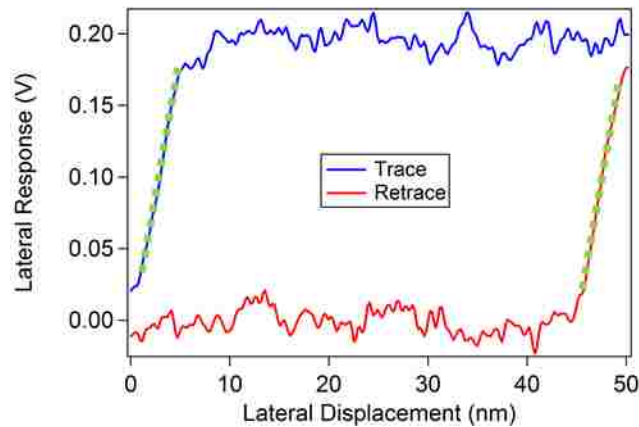


Figure 2.11. An example of a friction loop displaying the stick-slip turnaround point (fitted with a dashed green line) for a rectangular silicon cantilever on mica (probe 4).

Table 2.9. Comparison of OLS_x from friction loops and lateral thermal spectra.

Probe	A_{DC}^2 $10^{-14} \text{ V}^2/\text{Hz}$	Q	ν_0 kHz	k_{θ} , Sader nN m rad^{-1}	OLS_{Thermal} mV/nm	$OLS_{\text{Loop, Mica}}$ mV/nm
4	3.164	186.1	198.0	7.77	124.0	79.6
5	0.3562	326.8	897.7	7.78	108.7	60.1
6	4.823	163.8	279.6	5.30	142.8	69.7
8	0.05916	608.1	636.6	8.75	48.32	18.6

Chapter 3 Yield Strength of Glued Langmuir-Blodgett Films Determined by Friction Force Microscopy

*The work described in this chapter has been published in Wagner, K.; Wang, Y.; Regen, S.; Vezenov, D., Yield Strength of Glued Langmuir-Blodgett Films Determined by Friction Force Microscopy, *Physical Chemistry Chemical Physics*, submitted.*

3.1. Introduction

Since their discovery in the 1930's, Langmuir-Blodgett (LB) films have been the subject of many studies due to their capability to form thin organic layers on a variety of substrates.⁵¹ LB films have served as a low-cost solution to adeptly functionalize otherwise inert substrates for applications such as biosensors,^{48, 49} organic light-emitting diode devices,^{91, 92} thin film transistors,⁹³ organic photovoltaic cells,^{94, 95} lubricants for microelectromechanical devices (MEMS),⁴⁷ and permeation-selective barriers.⁹⁶ Originally proposed by Katherine Blodgett, LB films can also function as efficient filters for molecular gas phase separations⁵⁰ and display permeation selectivity to several generally inert gases such as He, N₂, and CO₂.⁹⁷ However, film quality and mechanical stability are critical parameters in the development of all such applications. It was previously shown that when poly(sodium 4-styrenesulfonate) (PSS, average molecular weight ~70,000) was substituted in place of alkali metal counterions at the central interface of the bilayers, the polyelectrolyte would act as a "glue" increasing the quality and stability of the film, while also providing unprecedented selectivity for gas separation.⁹⁸ Glued LB films displayed increased relative surface viscosities and surface pressure–area isotherms, as well as, film stability after rinsing with chloroform and storage in the atmosphere for days.^{50, 93} These observations, however, are indirect measurements of the LB film strength. Therefore, there exists a need for quantitative

characterization and qualitative ranking of the stability and the structural strength of the LB films. To confirm that the addition of a PSS interlayer strengthens a LB bilayer film, we performed a direct, mechanical test to measure the stability of such films.

LB bilayer films are created through a simple self-assembly deposition process. Figure 3.1a shows a cartoon of the formation of a bilayer film. First, an organized film of an amphiphilic surfactant is created using a LB trough. When a hydrophobic substrate is dipped through the film, a monolayer of surfactant is deposited on the substrate through hydrophobic interactions between the hydrocarbon chains and the substrate. During the up-trip, the second layer is deposited through charge interaction of the charged head groups. The charges are not drawn in Figure 3.1a, but the amphiphilic surfactant has multiple positive charges that are linked by anionic moieties in solution (either polyanions or single anions from metal salts). LB films of this nature may be applied to hydrophobic poly(1-trimethylsilyl-1-propyne) (PTMSP) membranes to act as filters for gas separations. Gases passing through such filters undergo separation based on molecular size, shape, hydrophobicity, or polarity depending on the molecular configuration of the LB layer.⁵⁰ It was proposed that, when poly(sodium 4-styrenesulfonate) (PSS, Figure 3.1b) was substituted in place of alkali metal counterions at the central interface of the bilayers. It was previously confirmed that PSS is at the center interface of the bilayer by variable angle x-ray photoelectron spectroscopy.⁹⁸ The addition of PSS is thought to improve film stability and gas selectivity by increased cross-linking within the film that creates larger molecular bundles and reduces the frequency of film defects.⁹⁹ It was also shown that cross-linking with a polyanion only improves the film quality in the surfactant is also polycationic.

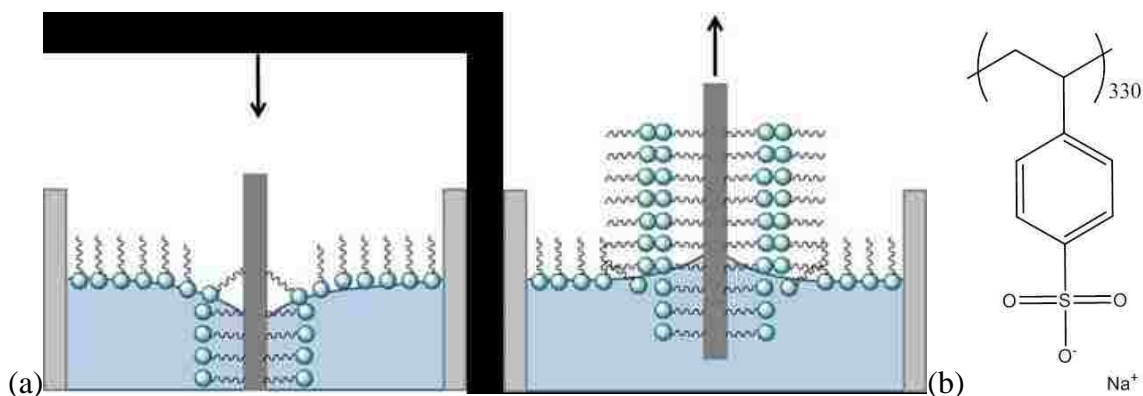


Figure 3.1. (a) Production of a Langmuir-Blodgett bilayer film. First, an organized layer of surfactant molecules are formed on the surface of water in a trough. As a hydrophobic substrate is dipped into the liquid, the hydrophobic tails of the surfactant interact with the substrate through hydrophobic and van der Waals interactions. Upon removal, the top layer is formed through ionic interactions through the charged head groups. Charges are not drawn in this figure. (b) Chemical structure of poly(sodium 4-styrenesulfonate) (PSS, average molecular weight of $\sim 70,000$ g/mol) that served as a poly-ionic glue.

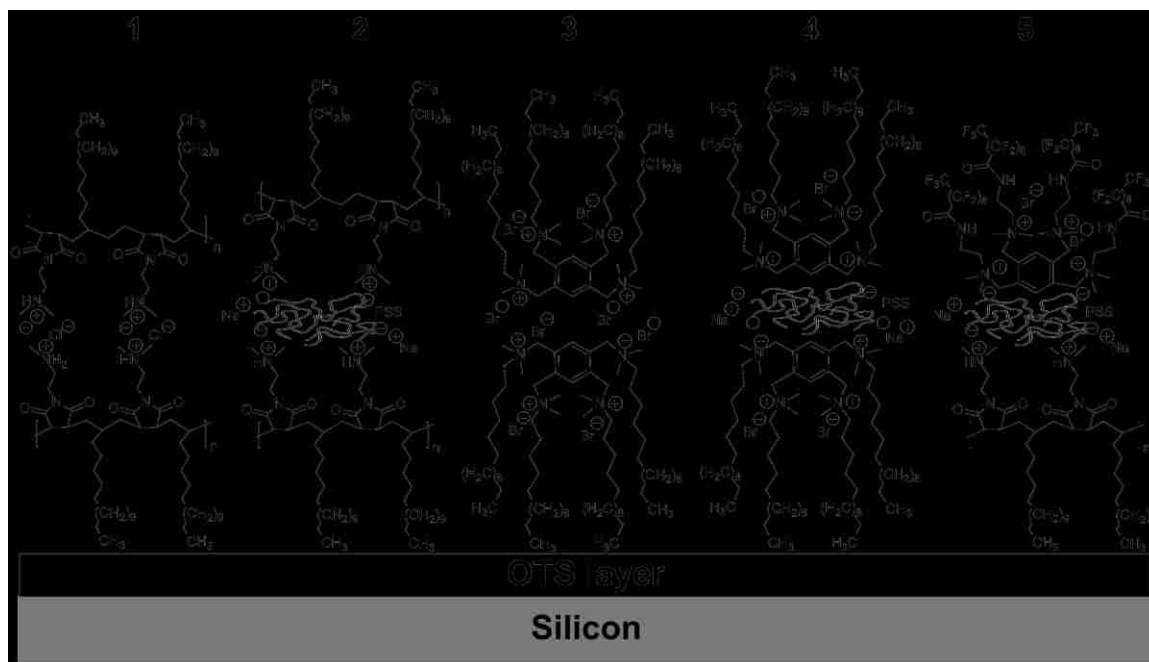


Figure 3.2. Chemical structures of the LB film bilayers prepared on OTS modified silicon wafers. **1** Bilayer of polymeric surfactant; **2** Glued bilayer of polymeric surfactant; **3** Amphiphilic bilayer; **4** Glued amphiphilic bilayer; and **5** Polymeric base layer with a PSS gluing layer and a perfluorinated amphiphilic capping layer. The degree of polymerization, n , of films 1, 2, and 5 exceeds 50. (film thicknesses are not drawn to scale)

Several current methods used to determine the strength of thin films include: force-distance curves,¹⁰⁰ repetitive atomic wear experiments,¹⁰¹ and nanoscratch experiments^{102, 103} (all performed using atomic force microscopy (AFM)), as well as experiments using surface forces apparatus^{104, 105} and theoretical simulations of friction.¹⁰⁶⁻¹⁰⁹ Extensive reviews are available on friction mechanisms in nanotribology.¹¹⁰ In all of the above approaches, a common, key observation is that irregular changes in the measured forces correspond to a structural transition that rearranges the organization of the film or leads to film failure. Friction force spectroscopy is a highly sensitive tool that can measure the forces that the LB films are capable of withstanding. The main drawback of the use of scanning probe based techniques for characterization of mechanical stability of ultrathin films is that the probe displacement (or true contact area) must be estimated or modeled indirectly.

We employed friction force spectroscopy experiments to determine the yield strength of several LB bilayer films formed on a hydrophobic silicon support (self-assembled monolayer of *n*-octadecyltrichlorosilane (OTS) on silicon). The bilayer films we selected for this experiment are displayed in Figure 3.2 and have shown permeation selectivity towards several inert gases.⁵⁰ LB films of this nature may be applied to hydrophobic poly(1-trimethylsilyl-1-propyne) (PTMSP) membranes to act as filters for gas separations. Gases passing through such filters undergo separation based on molecular size, shape, hydrophobicity, or polarity depending on the molecular configuration of the LB layer and overall gas separation selectivity decreases with the presence of film defects.⁵⁰ We measured the forces required to cause film failure and removal as an AFM probe was rastered across the sample over a single scan line. The

applied normal load was varied over each scan line during a damage cycle, allowing fast acquisition of friction *versus* load data with small, controllable load increments. We were able to damage the films in a controllable and reproducible manner by choosing an AFM cantilever of appropriate stiffness and obtained the yield strength of bilayer films from the analysis of friction *versus* load curves. The yield strength of the films are estimated using the conditions presented by the von Mises yield criterion.¹¹¹ To ensure consistency in our force calibration during our experiments, the same probe was used throughout a given series of films without optical realignment. While the experiments presented here address the yield strength of LB films only, we have found that this technique is generally applicable to both organic and inorganic ultrathin films. Recent reviews have also discussed the importance of mechanical stimulus to nanomaterials and nanosystems.¹¹²⁻¹¹⁴ While we do not discuss the gas separation performance of these LB films under strain, it would be interesting to measure the effects on the film gas separation selectivity with applied strain since film defects are known to play a role.

3.2. Methods

3.2.1 Preparation of LB Films^b

The glued LB bilayers were deposited onto OTS coated silicon wafers using a previously published procedure.^{50, 52, 97, 99, 115} Silicon wafers (WaferNet, Inc., San Jose, CA) were cut into 15 x 25 mm pieces and were immersed in concentrated H₂SO₄ and 30% H₂O₂ (70/30, v/v) at 70 °C for 4 h. Caution: “piranha solution” reacts violently with many organic materials and should be handled with great care. The wafers were then

^b Yao Wang produced the LB films and measured the film thickness by ellipsometry

rinsed with distilled water, dried under a stream of nitrogen. The resultant silicon wafer should have a SiO₂ film thickness of ~1.8 nm, as determined by ellipsometry. These wafers were then silylated immediately to avoid organic contamination by immersion in a 10 mM anhydrous hexane solution of n-octadecyltrichlorosilane (OTS) for 20 min at room temperature. The wafers were then rinsed with hexane and chloroform for 30 s. The ellipsometric film thickness of the OTS layer was $\sim 2.6 \pm 0.1$ nm and had an advancing contact angle of $\sim 110^\circ$. The silylated silicon wafer was placed onto the mechanical dipper as a substrate.

Typically, 50 μ L of a surfactant solution (1 mg/mL of chloroform) was spread onto a pure water subphase for preparation of unglued bilayers (or a subphase containing a 5 mM of PSS with an average molecular weight of 70,000 g/mol for preparation of glued bilayers), which was maintained at 25°C. After allowing the solvent to evaporate for 30 min, the film was compressed at a speed of 25 cm²/min to a proper surface pressure (typically, 30 dyn/cm). The surface pressure stabilizer on the film balance is then activated in order to allow the LB film to equilibrate for 30 to 60 min and to keep the monolayer at this pressure throughout the dipping process. The dipping speed (usually 2 mm/min) is set on the dipping mechanism controller and the substrate is lowered into the trough. While the substrate crosses through the air-water interface a monolayer is deposited onto the substrate. Once the substrate is completely submerged in the trough, the dipper is stopped, and the substrate remains submerged for approximately 3 minutes. The dipper mechanism is then reversed and the substrate is raised out of the subphase using the desired speed (usually 2 mm/min). When the substrate is raised from the liquid into air, a second monolayer is deposited onto the support. Thus, an

unglued/glued bilayer on the substrate is obtained. After transfer, the film must dry in ambient laboratory conditions for an additional two days.

3.2.2 Film Thickness Measurements by Ellipsometry

The procedure used to measure film thicknesses by ellipsometry was similar to those performed previously.^{50, 52, 97, 99, 115} Briefly, a Rudolph Auto-ELIII (Rudolph Instruments, Denville, NJ) single wavelength ($\lambda = 632.8$ nm) ellipsometer at an angle of incidence of 70 degrees was used to measure the film thicknesses. Measurements were taken at four different regions along the surface of each sample and the mean and the standard deviation were calculated. Film thicknesses were determined using the manufacturer's program (211 for a single layer, 221 for multiple layers). The refractive indices that were used to estimate the thickness of the OTS, LB layers, and silicon dioxide were 1.46, 1.50, and 1.465, respectively.

3.2.3 Film Yield Strength Determination Using Force Spectroscopy

Force spectroscopy experiments were carried out using an MFP-3D AFM (Asylum Research, Inc., Santa Barbara, CA) in contact mode with silicon nitride AFM probes integrated with V-shaped cantilevers (NP Series Probe, Veeco, Camarillo, CA) having a spring constant of ~ 0.4 N/m. The scan size was set at 5×5 μm with 256×256 data points and a scan rate of 1 Hz with a scan angle of 90 degrees (normal to the cantilever long axis). The slow axis scan was disabled during friction *versus* load experiments so that scanning occurred on a nominally single scan line. The precise tip location on the sample does vary slightly due to changes in the normal load and the 15°

inclination of the cantilever with respect to the sample.⁶⁷ The normal force was incremented automatically for each scan line using a programming code provided by Asylum Research. Lateral trace and retrace channels were captured and processed via a custom program written for Igor Pro 6.2 (Wavemetrics, Lake Oswego, OR) to produce friction *versus* load plots (by taking half of the difference between the lateral trace and retrace signals for each scan line). The average friction and standard deviation is determined for each scan line (*i.e.* single applied normal load). This process converts two friction force images (*i.e.* trace and retrace) into an averaged friction-load plot. Immediately before a film damage experiment, the set point voltage corresponding to zero normal force was measured by capturing a force curve and measuring the voltage far from the sample surface corresponding to zero applied load to account for any drift between scans. In addition, adhesion forces were measured prior to film damage from these force-distance curves over several locations on the sample.

3.2.4 Force Calibration

The normal force was calibrated by collecting force curves on a glass slide and fitting the linear portion of several extension curves to determine the detector sensitivity (44.2 nm/V). The normal spring constant was found from the thermal noise spectrum¹³ (0.411 nN/nm). The lateral sensitivity was determined using the wedge calibration method^{67, 116} (5.31 nN/mV) using a standard having features with triangular profiles (TGG01, MikroMasch, Tallin, Estonia). A full description of the lateral calibration is presented in the Section 2.6.2.

3.2.5 Determination of the Tip Radius

The tip radius was determined using an ultra-sharp silicon grating (TGT01, MicroMasch, Tallin, Estonia). The apex of the tip profile was fitted with the equation for a circle, as shown in the Section 3.5.3. The pyramidal silicon nitride tips were not symmetric, so an effective tip radius was determined, according to: $2/R_{\text{eff}} = (1/R_1 + 1/R_2)$. The effective tip radius was 130 nm. For consistency, several spikes were imaged and an average effective tip radius was determined.

3.3. Results and Discussion

3.3.1 Choosing Experimental Conditions for AFM Scratch Tests

To select a tip that would controllably remove the LB bilayers, we completed a series of simple nanolithography experiments on these films. We intended to achieve controllable removal of the film by finding an AFM probe that would create a lithographic trench at an applied load that falls within the dynamic range of the instrument, *i.e.* we would exclude probes that either could not produce lithographic trenches at any measurable applied load or did not provide sufficient range of stable, non-damaging forces. We performed a lithographic pattern that included several lines at increasing applied loads (set points) and then reimaged the area to observe film damage. In these nanolithography trials, we used AFM probes having cantilevers with normal spring constants, k_z , in the range of approximately 0.01 to 3 nN/nm. At the low end of this range, no damage was observed even at the highest possible settings for the set point (applied load). At the high end, *i.e.* for the stiff cantilevers, the damaged was observed

too early in the loading cycle. We selected a silicon nitride probe with $k_z \approx 0.4$ N/m as the most suitable probe for these experiments to determine yield strength.

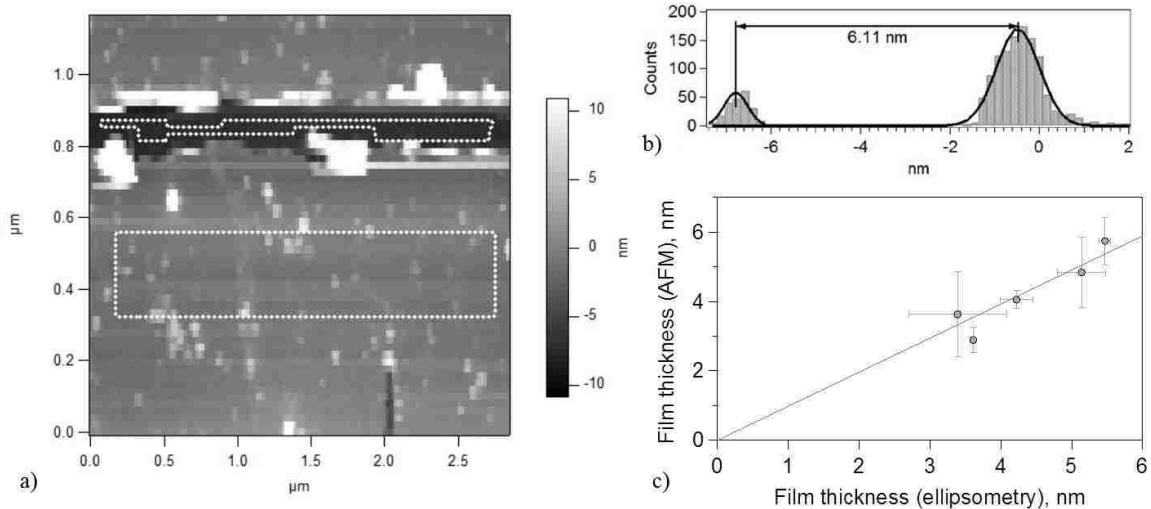


Figure 3.3. (a) Expanded view of a trench formed on film **5** with areas for use in step height calculations outlined by dotted lines. Areas around the scratch region where considerable debris from removal of the film is observed were avoided during film thickness measurements. (b) Histogram of the heights within the outlined regions. (c) Comparison of LB film thicknesses measured by AFM and ellipsometry. The errors for the AFM thicknesses are from the widths of the Gaussian fits (full width at half-maximum). The errors of the ellipsometry thicknesses are standard deviations from measurements at three different locations on the sample. The slope of the line fit is 0.97 ± 0.04 .

We compared the depth of the trenches produced at high normal loads (resulting in film removal) to film thickness measurements from ellipsometry. The film thicknesses measured by AFM were calculated by creating a histogram of the measured sample heights surrounding the trench (Figure 3.3). The thickness of the removed layer is the difference between the height of the top layer (away from the scratch pattern) and the height at the bottom of the trench as determined by fitting the histogram to Gaussian distributions. In all cases, we found that the entire bilayer film is removed during a yield experiment, thus, exposing the OTS substrate. We could not find an experimental

condition in which we could remove the LB film in a layer-by-layer fashion. Furthermore, our friction *versus* load plots do not display stable, intermediate regions suggesting layer-by-layer removal. We observed that the film thicknesses measured by AFM correlated closely with the thicknesses (Table 3.1) of the LB bilayers as measured by ellipsometry (Figure 3.3c). The slope of the line fit in Figure 3.3c is 0.97, showing an excellent agreement between the two methods, and demonstrating that the OTS monolayer remains intact after scratching experiments. Others have shown that OTS monolayers are not damaged with silicon probes at normal loads as great as 250 nN, much greater than the forces used here.¹¹⁷

Table 3.1. Applied normal and lateral forces at damage (L_c and F^* , respectively), adhesion forces (L_{ad}) measured from force curves, total normal load at damage, L^* (*i.e.* $L_c + L_{ad}$), and the film thickness, t_{AFM} and t_{ellip} , measured by imaging trenches via AFM and by ellipsometry, respectively.

Sample	L_c (nN)	L_{ad} (nN)	L^* (nN)	F^* (nN)	t_{AFM} (nm)	t_{ellip} (nm)
1	15.9 ± 1.3	12.9 ± 0.6	28.8 ± 1.5	1.8 ± 0.4	2.9 ± 0.4	3.6 ± 0.1
2	39.1 ± 3.6	9.8 ± 0.9	48.9 ± 3.7	5.9 ± 0.4	4.8 ± 1.0	5.1 ± 0.3
3	29.3 ± 2.5	8.4 ± 1.4	37.7 ± 2.8	3.6 ± 0.2	3.6 ± 1.2	3.4 ± 0.7
4	36.7 ± 0.5	10.9 ± 1.9	47.6 ± 2.0	5.2 ± 0.3	4.0 ± 0.3	4.2 ± 0.2
5	46.6 ± 5.0	9.3 ± 1.5	55.9 ± 5.3	22.9 ± 2.3	5.7 ± 0.7	5.5 ± 0.1

3.3.2 Friction *versus* Load Experiments on LB Bilayer Films

Friction *versus* load plots were produced by incrementing the applied normal force line-by-line during imaging over a fixed 5 μm line until film failure was observed (characterized by a sudden instability in friction forces). The experiments were chosen to focus on scanning a single line to reduce the scatter in data among trials performed on the

same sample. Deviations in results could be caused by small amounts of debris and variations in the film quality across the surface, since damage typically originates at defects.¹⁰¹ Friction *versus* load plots over an entire $5 \times 5 \mu\text{m}$ scanning area displayed a greater standard deviation of the friction force at a fixed load than friction at a nominally single line. Figure 3.4a displays a typical friction *versus* load plot for film 4, displaying three distinct regions. In Region A, the tip is sliding in contact with the top layer of the LB bilayer film, but is not deforming the film in an irreversible manner. In region B, discontinuities in the friction force corresponds to the tip plowing through the LB film at the point of film failure. In region C, stable friction is regained as a result of scanning on the OTS substrate. The described process is also drawn schematically in Figure 3.4b.

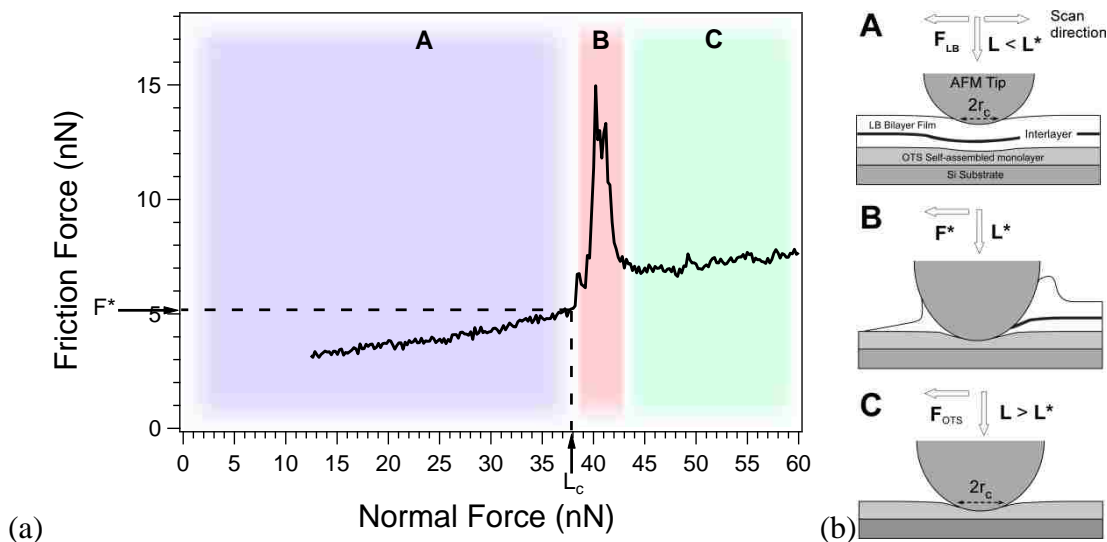


Figure 3.4. (a) A typical friction *versus* load curve for film 4. The three regions of deformation (labeled A, B, and C) are shown schematically in (b) (not drawn to scale). L is the total load (external load plus adhesion force). L_c and F^* are the normal and lateral forces, respectively, when the bilayer is damaged.

Any secondary structures in the peak observed in region B are likely due to initiation of multiple holes or small defects in the film, which grow until full film removal within a narrow range of the applied normal load. Inspection of the pseudo-2D images (friction *versus* scan line number or friction *versus* time) produced during the film removal indicates that the failure is initiated at a single point, which is then enlarged by the tip with occasional initiation of several more holes in the areas of intact film. These new defects also continue to grow in the course of increasing the load applied by the tip (see Section 3.5.5). In the case of film **4**, the slopes of friction *versus* load curve measured within regions A and C are expected to have a similar slope (friction coefficient), since the surface of both the LB film and OTS layer are terminated with methyl groups.¹¹⁸ We observed that distinctly different slopes are measured within these two regions if the terminal chemical functionalities of these layers are not the same, as in the case of film **5**, where different film friction coefficients are expected. Previously Subhalakshmi *et al.* demonstrated that the friction coefficient of a perfluorinated monolayer is more than twice the friction coefficient of its methyl terminated analog.¹¹⁹

Our friction *versus* load results are comparable to those observed in work by Kopta and Salmeron¹²⁰ on initiating wear of mica using an AFM probe. Sliding an AFM tip on mica displayed a stable region of wearless friction at low applied loads, followed by a critical point where an exponential increase of point-type defects led to rupture of Si-O bonds in a catastrophic manner and resulted in initiating the wear of the surface layer. The model that was proposed claimed that the production of defects was a consequence of an increased normal load that lowered the activation energy of bond breaking. The main difference between our system and wear on mica is that in our case

the substrate cannot be damaged by the tip (within the available dynamic range of the instrument). Thus, after an exponential increase in the friction force due to the damage of the top layer, the forces recover to form another stable region where no wear occurs.

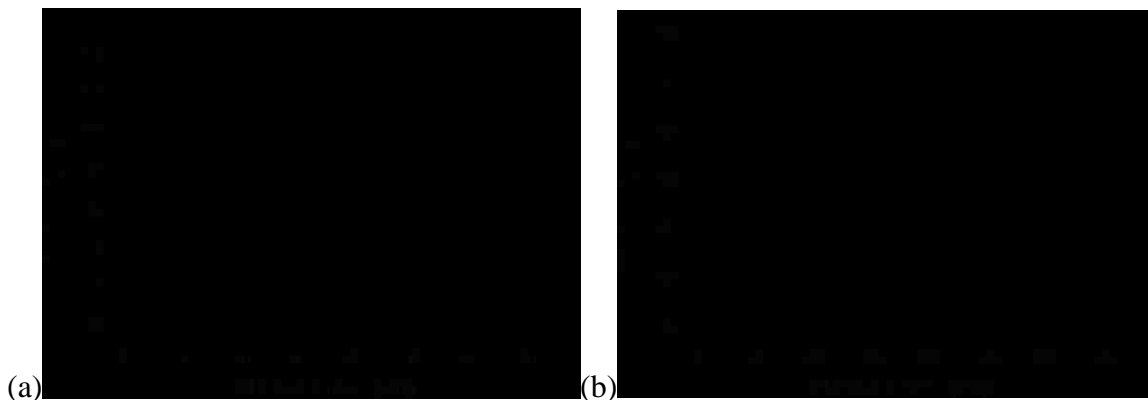


Figure 3.5. (a) Four friction *versus* load curves for film **3** displaying consistency between trials. Different line patterns correspond to a different location on the same sample. (b) Friction *versus* load curves comparing the friction coefficients of methyl and fluorinated capping layers for films **2** (dashed) and **5** (solid).

Removal of these films from the substrate obviously results in unavoidable tip contamination; however, we observed minimal differences between trials on the same sample. Figure 3.5a displays the consistency among several trials for film **3**. It is important to note that not only does film damage occur at similar forces, but regions A and C maintain a similar friction coefficient, indicating that sliding contact in regions A and C must exclude any trapped lubricating molecules. Furthermore, the adhesion forces of the films were measured by force-distance curves throughout the experiments at various locations and did not display large discrepancies in adhesion due to contamination.

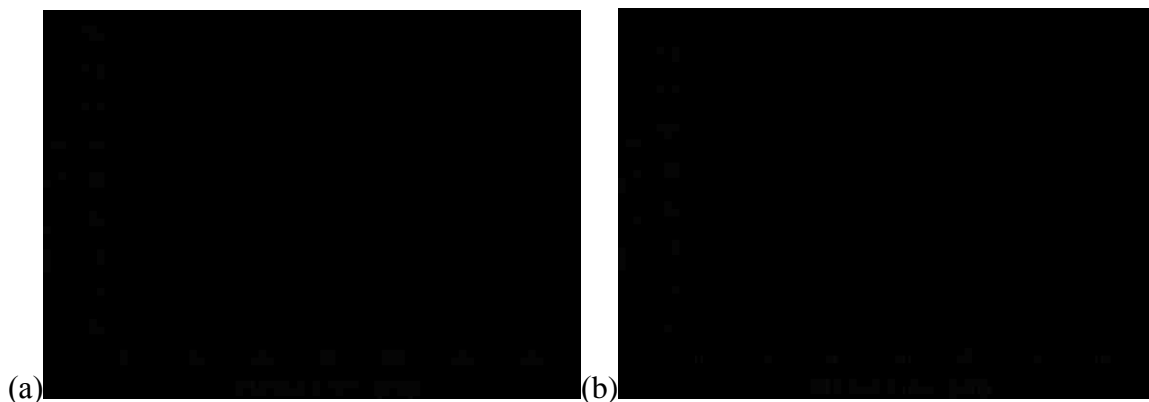


Figure 3.6. (a) Effect due to the addition of a PSS interlayer for film **1** (dashed) and **2** (solid). and (b) for film **3** (dashed) and **4** (solid).

It has been shown both experimentally and theoretically that the interfacial properties of organic films are affected by the nature of the terminal group and packing of the hydrocarbon chains in the monolayer.^{121, 122} To probe effects due to film functionality, we also completed friction *versus* load experiments on bilayer films using similar anchoring layers, but with a fluorinated capping layer. Figure 3.5b illustrates the differences in friction *versus* load curves between hydrocarbon and perfluorinated top layers (films **2** and **5**). As reported by others,⁴ the silicon nitride tip experiences a higher friction with a fluorinated surface than the methyl terminated surface as evidenced by the larger friction coefficient in region A. The friction *versus* load curve for the perfluorinated film does, however, recover a lower friction coefficient after removal of film **5**, indicative of the contact with a methyl terminated surface (*i.e.* OTS). Previous experiments have found that there is little or no correlation between surface roughness and friction force for LB films,¹⁰¹ suggesting that all differences in the measured friction forces are a direct result of film composition and structure. The values of rms surface roughness for all samples were within 2-3 nm over a $5 \times 5 \mu\text{m}$ area (see Section 3.5.2).

Wang *et al.* qualitatively displayed that the stability of the LB film after storage in atmospheric conditions depended on the number of hydrophobic contacts between the surfactant and the substrate as well as the nature of the anionic interlayer.⁹⁹ A greater number of hydrophobic contacts with the surface and cross-linking with PSS increased the film stability. The addition of PSS (average molecular weight $\sim 70,000$) increased the molecular area per repeat unit by almost a factor of two. Wang *et al.* hypothesized that cross-linking within the film increased film stability by reducing the probability of turnover and rearrangement within the film. To directly probe the effects of interlayer structure on the overall mechanical stability, we completed several friction *versus* load experiments on bilayer films where the only modification to the film was the composition of the interlayer. Figure 3.6a displays the resulting friction *versus* load curves for film **1** and **2** (addition of PSS interlayer) that are formed using a polymeric amphiphile. A dramatic, apparent effect of adding PSS is that the damage point for the glued LB film occurred at higher normal and frictional forces than for the non-stabilized LB film. The effect due to addition of PSS is not as pronounced for films **3** and **4**, which do not have cross-linked layers (Figure 3.6b). We expected that the weakest interface in our LB films would determine the mechanical stability of the system. In the case of the above LB bilayer films, this interface lies between the apolar substrate and anchor methyl groups of the deposited film, where only weak van der Waals forces exist. Surprisingly, strengthening of the internal structure of the LB bilayer by addition of PSS (*i.e.* at the internal interface where strong interfacial ionic bonding is already present) shows consistent improvement of the mechanical stability of these films, as witnessed by

increased damage forces listed in Table 3.1 (*i.e.* comparing film **1** and **2**, and film **3** and **4**).

Furthermore, the damage of films with a PSS interlayer (film **2** and **4**) occur at very similar forces (Figure 3.7). Films **2** and **4** should have different lateral mobilities of the individual chains in the LB film due to level of cross-linking within the bilayer surfactants. In the case of film **4**, only 4 hydrocarbon chains are linked together, whereas for film **2** there are about 50 such chains covalently linked together. In spite of the substantial differences in their lateral mobility, these LB bilayers fail at similar forces: the loads that are needed to provoke damage are almost the same for low and high degrees of polymerization in the surfactants (Table 3.1). However, comparing films **1** and **3**, it is surprising that cross-linking within the surfactant reduced the film stability. In the case of film **1**, it is possible that the probe may penetrate the film more easily due to an increased number of defects within the film (*i.e.* the larger molecular unit size of the surfactant may have more voids between units that may be easily rearranged). Previous nanowear experiments showed that a transition in wear behavior is only seen for polymers with considerably larger molecular weights (on the order of $M_w \sim 30,000$).¹²³ Others have also shown that mechanical properties of thiol and silane self-assembled monolayers (SAMs) remain mostly unchanged for various chain lengths for assembled layers with more than 10 carbon atoms in the backbone of the molecule.¹²⁴

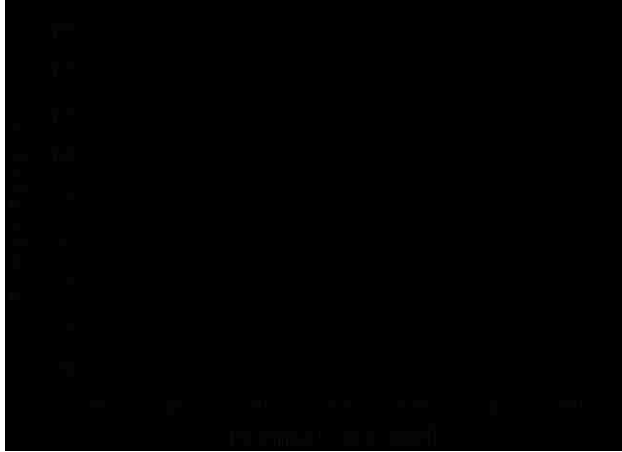


Figure 3.7. Comparison between glued bilayer films with and without cross-linked layers for film **2** (dashed) and **4** (solid).

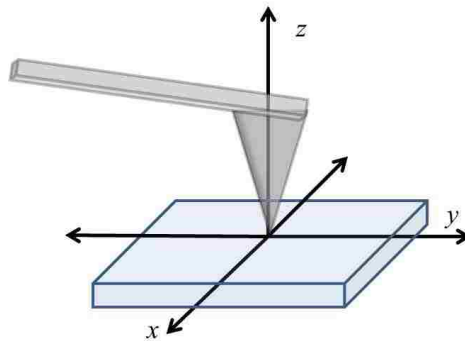


Figure 3.8. Orientation of probe with respect to the sample surface. The probe is scanned in the x -direction, therefore the cantilever is measuring forces and the x and z - directions. The calculation of the von Mises stress is simplified since there are only normal stresses in the z -direction and shear stress in the x - y plane.

3.3.3 Measurement of Yield Strength of LB Films

The yield strength can be considered as the maximum force experienced by the film, per unit area, at the point of initiation of failure. Due to the nature of our experiments, both the normal and lateral (shear) forces must be taken into consideration. In the theory of yielding materials, the von Mises yield criterion provides an estimate for the critical stress. The von Mises stress of a three-dimensional system, σ_{vm} , can be expressed by:¹¹¹

$$\sigma_{vm} = \frac{1}{\sqrt{2}} \sqrt{(\sigma_x - \sigma_y)^2 + (\sigma_x - \sigma_z)^2 + (\sigma_y - \sigma_z)^2 + 6(\tau_{xy}^2 + \tau_{yz}^2 + \tau_{xz}^2)} \quad (3.1)$$

σ corresponds to the normal stresses in each respective direction and τ corresponds to the shear stress in each plane. Since our sample is oriented so that the normal force is in the z direction and the shear force is applied in the xz plane (see Figure 3.8), the only components that will be nonzero are σ_z and τ_{xz} .¹²⁵ Therefore, the critical normal stress at yield is given by:¹²⁵

$$\sigma_{\max} = \frac{3L^*}{2\pi r_c^2} \quad (3.2)$$

r_c is the radius of contact and L^* is the load at film failure. Similarly, the critical shear stress is given by:

$$\tau_{\max} = \frac{3F^*}{2\pi r_c^2} \quad (3.3)$$

F^* is the friction force at film failure. Since our measured adhesion forces are not negligible with respect to the normal loads required to cause film damage, we cannot employ a Hertz contact mechanics model and should use a total critical load $L^* = L_c + L_{ad}$ (*i.e.* the applied normal load plus the adhesion force determined from force-distance curves).

Thin, soft films on a hard substrate display apparent mechanical behavior that is dependent upon the film thickness (*i.e.* as the film thickness decreases, the force required to reach a given indentation depth increases).³ For a complete, quantitative evaluation of the mechanical properties of these films one should utilize a complex compression model of a thin elastic film between two incompressible surfaces.^{3, 33} We chose to evaluate our data with the approach of classical contact mechanics, which, due to its simplifications,

provides for straightforward interpretation of all relevant parameters during the deformation. The downside of this simplification is that the final values of yield strength will likely have only an order of magnitude accuracy. Since our experiments are done with the same AFM probe and the films are structurally similar, we should still be able to make a direct comparison and ranking of the yield strength of these films determined in this approximate manner.

We fitted friction *versus* load data taken with the same AFM probe on a clean OTS substrate to a Carpick-Ogletree-Salmeron (COS)³² model to determine the most appropriate contact mechanics model to apply in our analysis. The COS model determines the transition region between Derjaguin-Muller-Toporov (DMT)³⁰ and Johnson-Kendal-Roberts (JKR)²⁹ models. We determined that COS transition parameter $\alpha=0.7$ (see Section 3.5.4) provided the best fits to experimental friction *versus* load curves on OTS samples. The value of this coefficient corresponds to the Tabor parameter of ~ 1.5 and suggests that our contact mechanics are more closely related to DMT theory.¹²⁶ From DMT theory, r_c is given by:²⁸

$$r_c = \sqrt{R\delta} \quad (3.4)$$

R is the tip radius and δ is the penetration depth of the tip:

$$\delta = \left(\frac{L + L_{ad}}{R^{1/2}K} \right)^{2/3} \quad (3.5)$$

K is the elastic modulus of contact between the tip and sample.

$$K = \frac{4}{3} \left(\frac{1 - \nu_f^2}{E_f} + \frac{1 - \nu_t^2}{E_t} \right)^{-1} \cong \frac{4}{3} \left(\frac{1 - \nu_f^2}{E_f} \right)^{-1} \quad (3.6)$$

Subscripts f and t signify the film or tip, respectively, E is the Young's modulus, and ν is the Poisson ratio. We assume E_t of 179 GPa,⁸⁷ resulting in $E_t \gg E_f$, and ν_f of 0.33 for the film.¹²⁷ Then, the von Mises yield criterion relates the critical normal and shear stresses to the penetration depth at film failure:

$$S_y = \frac{1}{\sqrt{2}} \sqrt{2 \left(\frac{3L^*}{2\pi R \delta} \right)^2 + 6 \left(\frac{3F^*}{2\pi R \delta} \right)^2} \quad (3.7)$$

One can develop a useful relationship for the yield strength of the films without making any estimates of δ or film moduli. With the use of Equation 3.5, the expression for S_y can be rewritten to exclude the film penetration depth. Then, the ratio $S_y/K^{2/3}$ is only dependent on the experimentally measured normal and lateral forces at the point of damage and the tip radius.

$$\frac{S_y}{K^{2/3}} = \frac{3}{2\pi} \frac{\sqrt{L^{*2} + 3F^{*2}}}{(L^* R)^{2/3}} \quad (3.8)$$

It was previously demonstrated that the yield strength is proportional to the Young's modulus of polymer materials.¹²⁸ Therefore, ideally, the calculated values of $S_y/K^{2/3}$ should be approximately constant among all LB films and indeed were observed them to fall in a relatively narrow range (Table 3.2), glued bilayers having slightly higher values than non-glued ones.

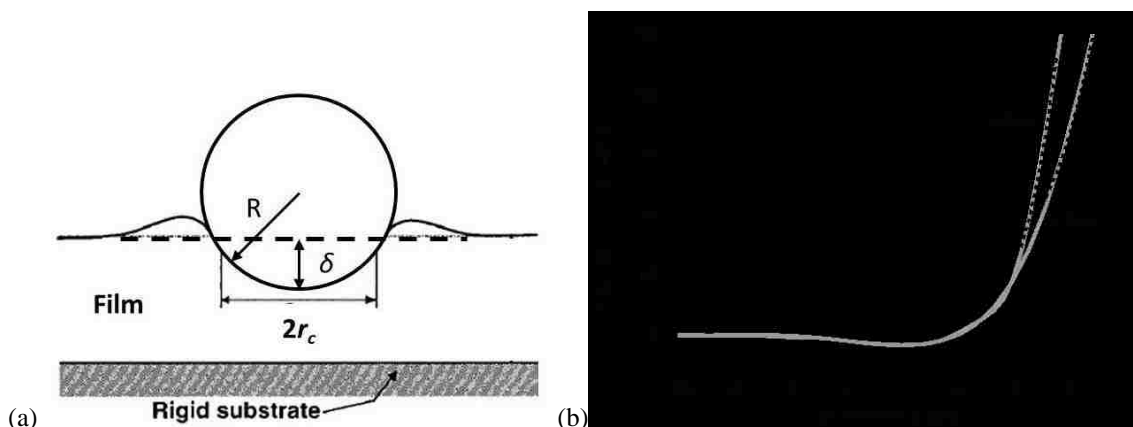


Figure 3.9. (a) Diagram of a probe with radius, R , indenting a distance, δ , into a thin film. The contact area, r_c , between the probe and film increase non-linearly with load. (b) Example of the quality of the fit to Equation 3.9 (dotted black line) for film **1** and **2**. Since the point of contact with the film is ambiguous, an offset to the indentation of ± 0.5 nm was required to provide good fits.

In order to calculate the yield strength of the films, we estimated the Young's modulus from fitting indentation curves (L versus δ) with the following equation expected for DMT deformation model (Figure 3.9).¹²⁹

$$L(\delta) + L_{ad} = \frac{E_f R^{1/2}}{3(1-\nu_f^2)} \delta^{3/2} \quad (3.9)$$

Figure 3.9a shows a cartoon of a spherical probe indenting a thin film. Since the tip used in these experiments had a asymmetric pyramidal shape, the calculation of film indentation is likely approximate. The values of Young's moduli are displayed in Table 3.2. There is a natural grouping of the film properties for films with and without PSS gluing layer. The Young's modulus of films with PSS is higher than the modulus of their analogs without PSS by a factor of two. This strengthening of the elastic modulus resulted in higher force tolerances in both the normal and shear directions. Overall, the measured Young's moduli of the films are similar to those of compliant organic polymers

such as polyethylene.¹²⁸ A theoretical calculation of the tensile yield stress of polymers at room temperature follows a relationship of $S \approx E_f/30$,¹³⁰ although some experiments show a relationship closer to $S \approx E_f/20$.¹²⁸ Clearly our nanoscratch experiments are not parallel with macroscopic tensile or compression test experiments, but we observed a similar scaling relationship of $S_y \approx E_f/10$. Furthermore, to ensure that the fitted Young's modulus values are appropriate, the indentation depth, δ , is calculated for each film (Table 3.2) - δ values should not exceed the measured films thicknesses in Table 3.1. Interestingly, films with a PSS interlayer have an indentation depth at damage of 50-60% of the total film thickness, while films without PSS have an indentation depth of 80-100% of the total film thickness. In both cases, it appears that irreversible film disintegration commences once the tip penetrates into the interlayer region.

As expected, the addition of PSS increased the overall strength of the films. Cross-linking within the top and bottom layers of the film did not result in major changes in the yield strength. The increase in the yield strength when PSS is added was considerable (~90% increase between film **1** and **2** and ~60% increase between film **3** and **4**). Furthermore, when the capping layer of the glued bilayer film was modified, its yield strength appeared to be similar to other glued films in spite of the substantial change in the frictional properties. It is interesting that strengthening the central interface of the film has such a large effect on the film strength since we would expect the weakest interface to lie between the film and the hydrophobic substrate. Because all of the LB films used in these experiments have macroscopically identical film/substrate interface, the measured changes in yield strength must be a result of strengthening the interactions between the bilayers within the films.

Table 3.2. The $S_y/K^{2/3}$ ratio, the Young's modulus of the film (E), yield strength (S_y), and the estimated indentation depth of the film at damage using E (δ^*_{calc}).

Sample	$S_y/K^{2/3}$ (Pa ^{1/3})	E (GPa)	δ^*_{calc} (nm)	S_y (MPa)
1	57 ± 2	0.50 ± 0.20	2.3 ± 0.2	47 ± 1
2	70 ± 4	0.97 ± 0.20	2.1 ± 0.3	89 ± 2
3	63 ± 3	0.48 ± 0.05	2.8 ± 0.2	51 ± 2
4	69 ± 2	1.0 ± 0.10	2.0 ± 0.2	89 ± 1
5	87 ± 6	0.86 ± 0.05	2.5 ± 0.2	100 ± 4

The measured yield strengths of these LB films are comparable to other nanoscale yield experiments carried out on protein films,¹²⁵ salivary films,¹²⁹ and polyethylenes.¹²⁸ Our nanoscale yield strength data also agree well with the mechanical properties of polymers measured macroscopically (low density polyethylenes <14 MPa, high density polyethylenes 18-32 MPa, and polyvinylidene chloride 69 MPa).¹³¹ It is also instructive to compare the yield strengths of these LB films having non-covalent attachment on solid surfaces to the critical shear stress needed to displace thiol monolayers from Au surfaces, reported to be two orders of magnitude higher – at 2.3 GPa,¹³² where a covalent S-Au bond would be broken. Overall, the primary uncertainties associated with quantitative characterization of the yield strength in ultrathin films using friction force microscopy as a tool for nanowear characterization is the proper calibration of the instrument and correct estimation of the film moduli.

3.4. Conclusions

We described friction *versus* load experiments that enabled us to discriminate between the yield strengths of several structurally-similar LB films. While our adopted model for contact mechanics is simplified for the actual sample geometry, a definitive ranking could be established between the above films. The measured yield strengths for LB films are in fair agreement with available data for organic polymers of comparable structure. We demonstrated that there are measureable differences in the forces required to initiate film damage and that the LB film is removed in the all-at-once rather than in a stepwise, layer-by-layer manner. The addition of a poly-ionic interlayer increased the overall film strength by almost a factor of two and, therefore, is a viable strategy to improve mechanical robustness of the LB bilayers in potential applications even when the interface between the LB film and solid support is unchanged. With carefully designed experiments, it would be interesting to measure how the strength and lateral mobility within these thin films directly affects their performance in gas separations, thus helping design films with improved performance. Further experiments on this class of LB films should focus on how external stimuli affect the film strength and performance. For example, similar films have displayed different gas permeation selectivity when hydrated.⁹⁸ Yield strength experiments at varying water vapor content could help shed more information on the overall performance of these films. Since gas permeation occurs through molecular sized holes and defects within the films, it would also be interesting to analyze the gas separation performance with strain applied to the films. Future research could focus on the effects of adding poly-ionic layers to thicker layer-by-layer films to

see if there is a scaling effect to strengthening the interlayer interfaces with total film thickness.

3.5 Appendix

3.5.1. Set Point Ramping Code.

The following programming code was used to increase the set point by a defined amount over each scan line of the image. The code was provided by Jason Bemis of Asylum Research, Santa Barbara, CA. The program runs within the Igor 6.03A (and newer) programming interface of MFP-3D controller interface.

```
td_WriteString("OutWave0StatusCallback","MainSetVarFunc(\"SetpointSetVar_0\",  
GV(\"DeflectionSetpointVolts\")+.1,\"\",\":Variables:MasterVariablesWave[%Deflection  
SetpointVolts]\")")
```

The portion of the code “**.1**” defines set point increment (in Volts, 0.1 V here) for each scan line of the image and may be changed by the user to produce the desired final load.

3.5.2. Surface Roughness.

The surface roughness was measured by AFM on an area of each sample free of abnormal debris or damage. The root mean square (rms) roughness was determined through the MFP-3D software for a 5 μm scan. Consistent with previous studies,¹⁰¹ friction force is independent of the roughness of the sample.

Table 3.3. Roughness values (5 μm \times 5 μm) for LB films measured by AFM.

Sample	RMS Roughness (nm)
1	2.4
2	1.7
3	1.7
4	2.4
5	2.8

3.5.3. Measurement of the Tip Radius

The tip radius was measured by imaging an ultra-sharp silicon grating calibration standard TGT01 (MicroMasch, Tallin, Estonia). Veeco NP series probes have an overall pyramidal shape, but are asymmetrical in shape, thus we determined the effective tip radius according to: $2/R_{\text{eff}} = 1/R_1 + 1/R_2$. The height image of the tip was examined using line profiles going through the apex of the tip in two orthogonal directions. The top section of each profile $h(x)$ was fitted with an equation for a sphere $h(x) = h_0 + \sqrt{R^2 - (x - x_0)^2}$ to find the radii R_x and R_y . Figure 3.10 shows a typical image of the silicon nitride tip formed by a sharp feature of the silicon grating along with the line profiles in the vertical and horizontal directions. The reported values of tip radii were measured on several different ultra-sharp silicon features (3-4) and the average tip radius was 130 nm.

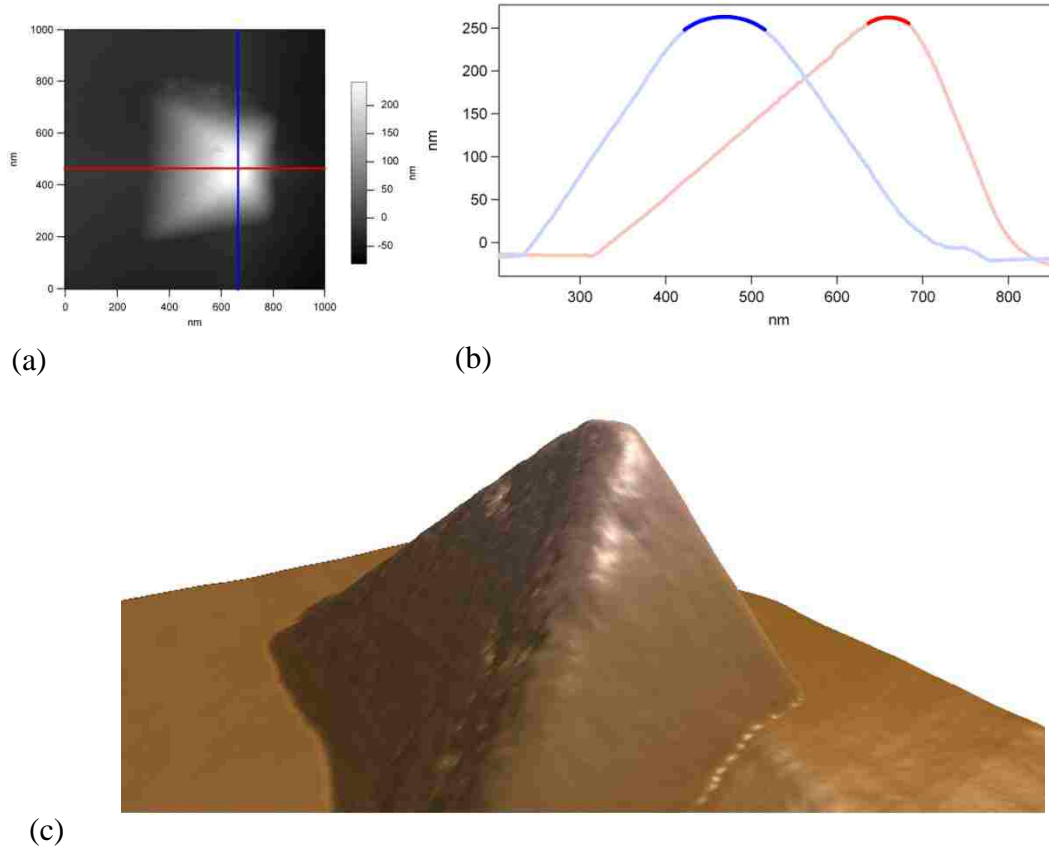


Figure 3.10. (a) Height image of an ultra-sharp spike on a TGT01 calibration grating, (b) Line profiles of the tip image fitted with a sphere equation (dark lines) at the apex of the peak, (c) 3-D shape of the tip.

3.5.4. Determination of the Tabor Parameter

The Tabor parameter,¹²⁶ μ_T , is used to quantify the transition between the DMT³⁰ and JKR²⁹ regimes for surface deformations and defined by:

$$\mu_T = \left(\frac{16RW^2}{9K^2z_0^3} \right)^{1/3} \quad (3.10)$$

z_0 is the equilibrium separation of the surfaces (typically ~ 0.1 nm), R is the radius of the probe (130 nm), K is the elastic modulus of the tip-sample interface (18.9 GPa), and $W = L_C / (1.5 - 2\pi R)$ is the work of adhesion (63-84 mJ/m² depending on the selected contact

mechanics model, using an adhesion force of 51.3 nN from the force curves on OTS).³² The Tabor parameter is calculated to be approximately 1.4 – 1.7. This value is in an intermediate region between the DMT and JKR model, but is more characteristic of the DMT model. The transition to the JKR model occurs when $\mu_T > 3$.¹²⁶

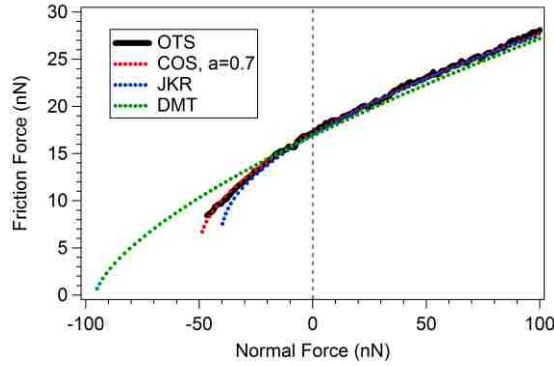


Figure 3.11. Fitting of a friction *versus* load curve of a silicon probe on an OTS surface with equations for the COS, DMT, and JKR models. The intermediate model with $\alpha=0.7$ provides the best fit to our data.

The Tabor parameter and the Maugis-Dugdale³⁴ parameter are approximately equivalent and may be replaced by a single transition parameter, α .³² For an intermediate fitting model the value of α varies between 0 and 1: where $\alpha=0$ corresponds to the DMT model and $\alpha=1$ represents the JKR model.³² It is also possible to fit the experimental data with the following equation to determine the extent to which our data follows the transition between DMT and JKR contact mechanics models.

$$F(L) = F_C \left(\frac{\alpha + \sqrt{1 - \frac{L}{L_C}}}{1 + \alpha} \right)^{4/3} \quad (3.11)$$

$F(L)$ is the friction force, F_C is the friction force at zero load, L is the applied load, and L_C is the adhesion force. Figure 3.11 shows the results of fitting the friction *versus* load curves on clean OTS with the intermediate, DMT, and JKR equations. The intermediate fit with $\alpha=0.7$ provides the best fit of our data and corresponds to μ_T of ~ 1 in reasonable agreement with the estimations made above.

3.5.5. Pseudo 2-D Height Images of Film Damage

Typically, our experimental friction *versus* load curves displayed damage regions with some level of secondary structure. This is likely purely a result of point defect failure in the film, followed by complete removal as the normal load is increased in successive scan lines. Below is an example height image of how damage usually initiates in a small area and propagates to complete film failure (Film 2). The localized damage point (arrows marked below) corresponds to the point in the friction *versus* load curves at the onset of damage (*i.e.* the terminus of stable friction behavior) where damage forces were measured for calculations.

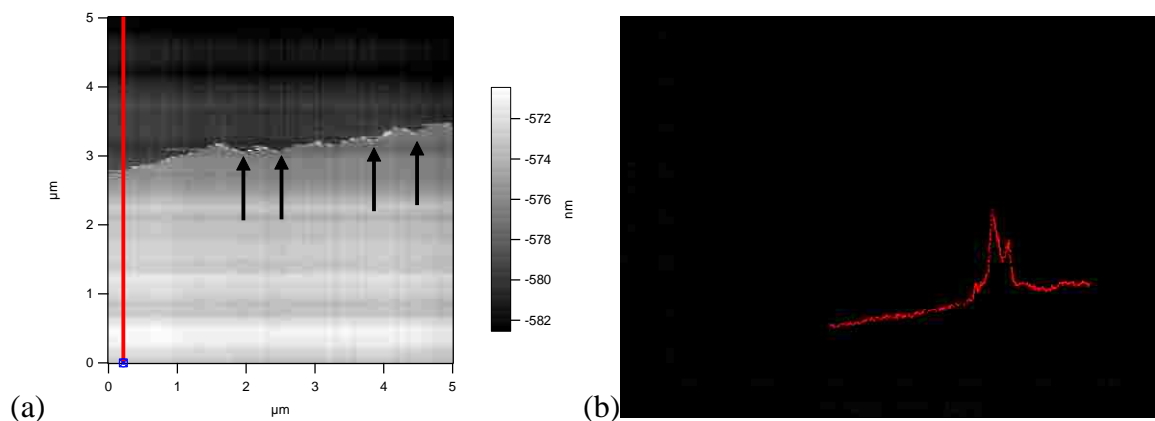


Figure 3.12. (a) Height image of continually increasing applied set point (set point increases from bottom of the image to the top). (b) Dotted line corresponds to calculated friction along the indicated line in the height image against the total average friction *versus* load curve (solid line).

3.5.6. Film Indentation Curves.

Figure 3.13 displays the indentation curves for all films. Each indentation curve is the average of at least 20 individual indentation curves.

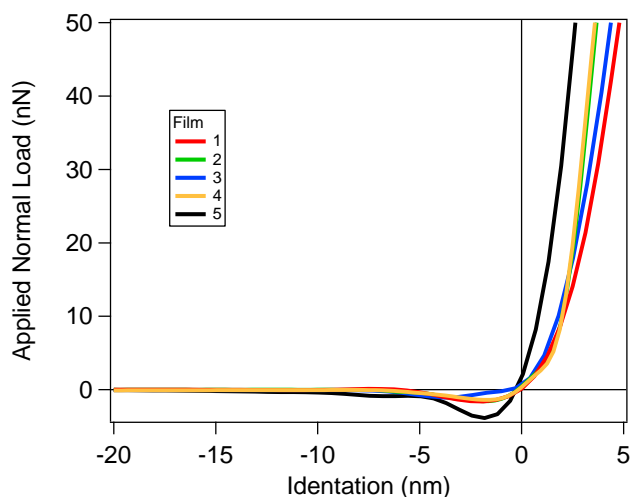


Figure 3.13. Averaged indentation curves for LB bilayer films.

3.5.7 Nanolithography Experiments

In order to determine an appropriate probe to use for the nanoscratch experiments, simple lithography experiments were carried out using several AFM probes with spring constants varying from approximately 0.01 - 3 N/m. In these experiments, horizontal lines were created in contact mode at several incrementing set points. The goal of this experiment was to find a tip with a spring constant that would damage the LB bilayer film at an applied normal load within the dynamic range of the instrument detector, but also cause no damage to the film at a finite normal load. In order to view damage of the film, the lithography area was imaged to identify trenches (*i.e.* removal of the film). Images of the LB films after lithography experiments with several probes of varying

stiffness are shown in Figure 3.14. We observed that a probe with an intermediate spring constant (3 N/m) caused damage even at low applied normal loads, and that probes with a small spring constant (0.01-0.1 N/m) were incapable of causing damage within the dynamic range of the instrument. We found that probes having a spring constant of approximately 0.4 N/m produced controllable damage to the LB bilayer films within the experimentally accessible normal loads in our experiment. We also observed that silicon nitride tips were more resilient than silicon tips – an important property for our experiments, since multiple samples are compared with a single probe with multiple (5 or more) trials on each sample.

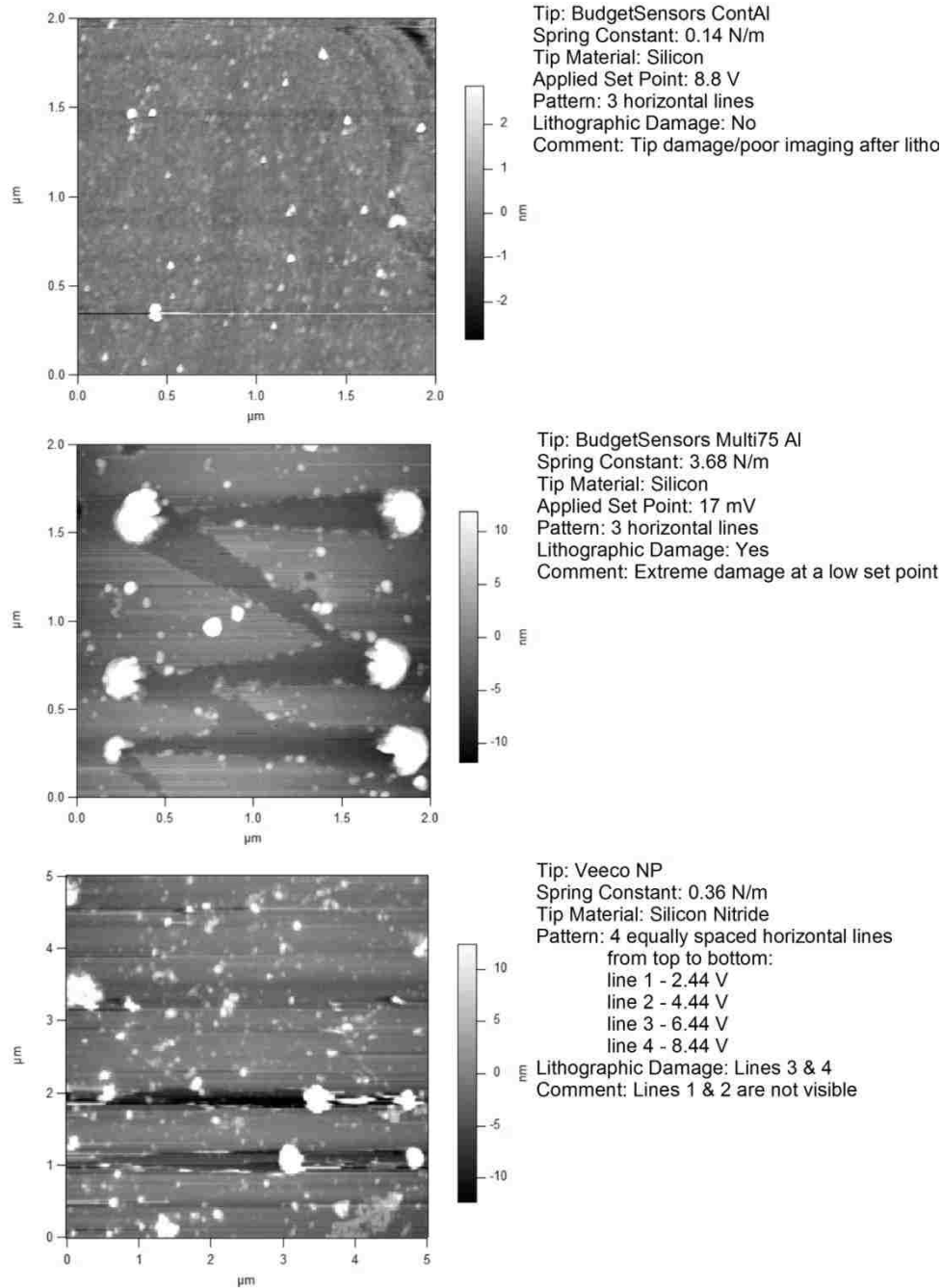


Figure 3.14. Lithography patterns (each pattern consists of separate, horizontal lines with increasing applied normal load) for three different AFM probes with spring constants ranging from 0.1 N/m to 3 N/m performed on Film 4. The Veeco silicon nitride contact mode probe produces damage at high applied normal loads, while showing no damage at low normal loads. The Budget Sensors Multi75 probe showed uncontrollable damage even at a low normal load and a Budget Sensors ContAl probe showed no damage even at high applied normal loads. Without calibration, the applied set point is proportional to applied normal load (the maximum experimentally accessible set point range is $\pm 10V$).

Chapter 4 Peeling Single Stranded DNA from Graphite to Model Interactions between DNA and Carbon Nanotubes

Most of the work described in this chapter has been published in Iliafar, S.; Wagner, K; Manohar, S.; Jagota, A.; Vezenov, D., Quantifying Interactions between DNA Oligomers and Graphite Surface Using Single Molecule Force Spectroscopy, J. Phys Chem C, 2012, 116 (26), 13896-13903.

4.1 Introduction

The interaction between biological molecules and nano- or macro-sized surfaces is a dynamic and commonly occurring process in nature, and if well understood, it can be used to develop novel biosensing technologies and therapeutics. The attachment of biomolecules to nanomaterial substrates such as gold nanoparticles and single walled carbon nanotubes (SWCNTs) greatly enhances their structural functionality, making it possible for these hybrids to be used in biological processes. The formation of stable dispersions of SWCNTs formed by helical wrapping of single-stranded DNA (ssDNA) around the tubes¹³³ makes SWCNTs highly compatible for *in vivo* systems and also provides a means for tube sorting and positioning.^{134, 135} CNT-DNA complexes have potential applications of broad biomedical impact, such as, transport of biomolecular agents into cells,¹³⁶⁻¹³⁸ optical sensing for biological systems,¹³⁹ rapid DNA sequencing,¹⁴⁰ and diagnosis and therapeutic treatment of diseases, such as cancer, through imaging and targeted drug delivery.^{136, 137, 141-146} Rational development of these applications will greatly benefit from quantitative understanding of the interactions that occur between the CNT and biomolecules.

It has previously been shown that single molecule force spectroscopy (SMFS) is an appropriate method to directly measure the force required to overcome the binding free energy between the DNA oligomers and a solid substrate.¹⁴⁷⁻¹⁵² For the SMFS

experiments, we assumed that the graphite substrate serves as an appropriate analog for SWCNTs used in bulk dispersion experiments.¹⁵³ Within the pyrimidine family, we were able to differentiate between 3'-poly(dT₅₀) and 3'-poly(dC₅₀) – with peeling forces of 85.3 ± 4.7 pN and 60.8 ± 5.5 pN, respectively (as a shorthand notation in this chapter, an oligomer naming convention will be used to indicate the point of attachment of the DNA to the force probe by listing the strand direction first and the number of bases in the oligomer chain is signified by a subscript).¹⁵⁴

Simulations have shown that the binding strength of homopolymers to graphite follow a different sequence: T>G>A>C,^{133, 155} than that of individual nucleotides obtained from solution studies: G>A>T>C,¹⁵⁶⁻¹⁵⁹ or of nucleobases and nucleosides determined by isothermal titration calorimetry: G>A>C>T.¹⁶⁰ Furthermore, guanine-rich DNA sequences are known to form G-quartets and, in some cases, they form quadruplex structures by the vertical stacking of G-quartets.¹⁶¹ It is interesting to see whether such structural features will be reflected in the SMFS measurements as they are the likely reason for sequence dependence of the binding strengths. Since purines are larger and chemically different from pyrimidines, it is interesting to use the SMFS technique to compare the interaction between homopolymer purines (polyadenine and polyguanine) and graphite with pyrimidines in order to understand differences between observed trends for monomers and predict the behavior for DNA oligomers in complexation with CNT. Since the interactions between DNA and graphite is assumed to be partially due to hydrophobic interactions, it is expected that the purines should have a stronger interaction with graphite due to the larger area of interaction of the homopolymer bases with the substrate.

Here, we report on the use of SMFS to measure the peeling forces of the purine homopolymers on graphite, 3'-poly(dA₅₀) and 5'-poly(dG₁₀₀), in order to complete a full ranking of the four homopolymer chains. The contribution of the hydrophobic interactions to peeling forces was also investigated by measurement of the peeling forces on self-assembled monolayers.

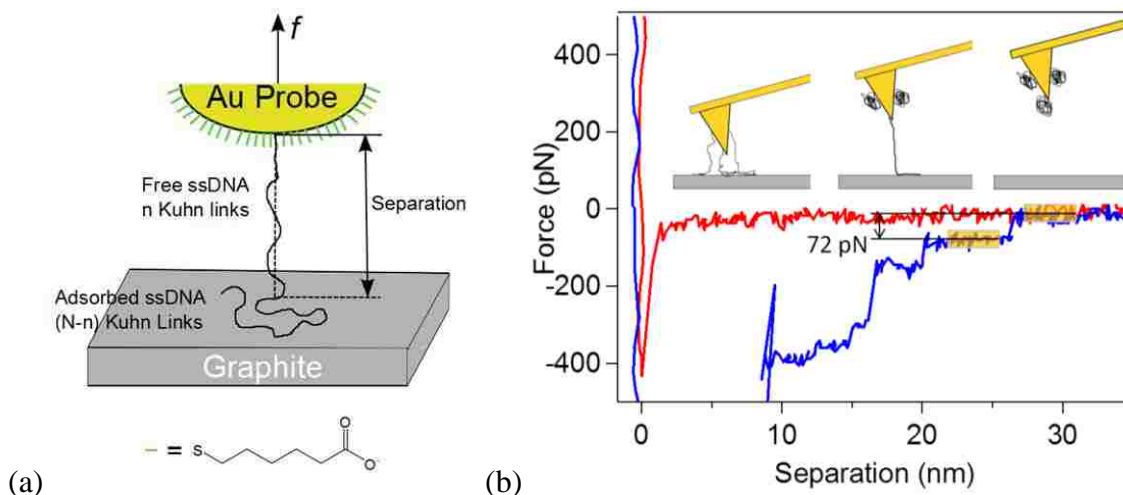


Figure 4.1. (a) Idealized cartoon (not drawn to scale) of frictionless peeling of a ssDNA homopolymer, attached to a gold coated force probe, from a graphite surface. Due to the frictionless nature of the substrate, the adsorbed bases slide freely on the surface and ssDNA detachment occurs perpendicular to the surface. (b) Typical force-distance curve for peeling 5'-poly(dT₁₀₀) ssDNA from the surface of graphite with illustration of oligomers adsorbed to the surface and steady-state peeling of a single oligomer. Orange boxes highlight areas that were used for averaging to determine the peeling force. Red curve is approach, blue is retraction.

4.2 Methods

4.2.1 Materials

Grade 2 highly ordered pyrolytic graphite was purchased from Structure Probe, Inc. (West Chester, PA). Disulfide-protected thiol-modified DNA was resuspended in Milli-Q deionized (DI) water upon receipt from Integrated DNA Technologies, Inc.

(Coralville, IA), aliquoted and stored at -20°C . The DNA molecules studied in this work were: 5'-poly(dT₅₀), 5'-poly(dT₁₀₀), 3'-poly(dA₅₀), and 5'-poly(dG₁₀₀). Tris(2-carboxyethyl)phosphine hydrochloride (TCEP), 98% purity, was used as-received from TCI America (Portland, OR). Mercaptohexanoic acid (MHA), 90% purity, was used as received from Sigma Aldrich (St. Louis, MO) and stored at -4°C . Mono- and di-basic sodium phosphate and sodium chloride in ultra-pure bio-grade were purchased from J.T. Baker (Phillipsburg, NJ).

4.2.2 Probe Functionalization

The AFM probes (ContGB gold coated AFM probes with normal spring constant $\sim 0.3\text{ N/m}$ from Budget Sensors, Inc., Sofia, Bulgaria) were cleaned by exposure to air plasma (using room air as source) for 1 minute on high power (PDC-001 plasma cleaner from Harrick Plasma, Ithaca, NY). After cleaning, gold coated tips were immediately immersed in ethanol to reduce any Au-oxides formed during cleaning. The terminal thiol group in the modified ssDNA was deprotected with 6 mM TCEP in the solution containing the DNA for 30 minutes. To attach thiol modified ssDNA to the Au coated AFM tips, the chip was placed in a 0.1-1 nM solution of ssDNA in a 10 mM phosphate buffer and 1 M ionic strength NaCl (pH ~ 7) for 1 hour. In order to fill in the remaining Au sites on the surface of the tip, the cantilever chip was then submerged in a 3-15 mM solution of MHA in ethanol for 1 hour. Each functionalization step was followed by washing with ethanol and drying with nitrogen gas. Empirically, optimized density of the DNA molecules on the AFM tip is a compromise between the needs of 1) having a high number of attached ssDNA molecules to increase the yield of tips displaying peeling and

2) ensuring low enough contact adhesion so that initial adhesive pull-off of the tip from the surface does not mask the peeling process that follows.

4.2.3 Monolayer Preparation

The surface of gold coated silicon wafer ($\sim 1 \text{ cm}^2$) was functionalized with thiol chemistry using dodecane thiol and mercaptoundecanoic acid. The gold coated wafer was freshly prepared by e-beam evaporation with a 50 nm thick gold layer and 15 nm thick chromium adhesion layer. Gold substrates were cleaned prior to use in air plasma for 1 minute followed by rinsing with ethanol. The gold substrates were submerged in 4% by volume solutions of dodecane thiol or mercaptoundecanoic acid in ethanol for 1 hour. Substrates were rinsed with ethanol and dried upon removal.

For experiments measuring the temperature dependence of hydrophobic adhesion forces, silicon wafers were functionalized with a Teflon (Teflon AF 2400, DuPont) thin film using a previously published procedure.¹⁶² Force curves were captured using a large radius AFM probe (LRCH, Team Nanotec, tip radius = 230nm) in water.

4.2.4 Force Calibration and Force Curve Capture^c

Force spectroscopy measurements were performed using an MFP-3D atomic force microscope (Asylum Research, Santa Barbara, CA). The graphite surface was freshly cleaved with Scotch[®] tape prior to each experiment and immediately placed in a fluid cell, which was then filled with approximately 3 mL of 10 mM phosphate buffer

^c Force curves of homopolymer oligomers on graphite were also recorded by Suresh Manohar and Sara Iliafar. Presented statistics of peeling forces include experiments completed by all of the above authors.

containing 100 mM NaCl. Probes were calibrated at the end of each experiment to avoid damaging the DNA or the gold coating under heavy compressive loading. The deflection sensitivity for each AFM cantilever in fluid was calibrated by determining the slope of the linear compliance region of the force-distance curves taken with the graphite sample. The most accurate calibration of the spring constant, however, is found in air, where the thermal spectrum of the cantilever is robustly represented by a simple harmonic oscillator model (Chapter 2.4.2).¹³ Therefore, the spring constant of the cantilever was determined at the end of each experiment in air by the thermal calibration method using the deflection sensitivity measured against glass in air.¹³

The DNA peeling forces were measured using a force-volume map over a $5\ \mu\text{m} \times 5\ \mu\text{m}$ area (with a 16×16 grid of force-distance curves) or by collecting individual force curves at several different locations on the sample. The force-volume map provides a fast, representative view of the interactions between DNA and graphite surface – accounting for any surface defects or steps between layers. Most force curves were recorded at a scan rate of 200 nm/s using a maximum compressive force of less than 1 nN. The maximum applied force was limited in order to protect the DNA from damage at high compressive loads. Analysis of the force-distance curves was performed using a custom code written in IGOR Pro (Wavemetrics, Eugene, OR). This code averages the force measured over a distance of at least 2 nm on both sides of the molecule detachment step and determines the peeling force by taking the difference.

In analyzing the force-displacement curves obtained from these force spectroscopy experiments, the force curves were only considered to be valid and suitable for further measurements if they possessed all of the following characteristics: 1) the

approach and retraction retraces overlapped for the non-contact region, 2) the separation distance of the last peeling step is smaller than that of the sequence's contour length unless the formation of secondary structures is possible, 3) the tip-surface adhesion is small enough that the peeling steps are not masked by initial pull-off force, and 4) the peeling region displays a flat plateau for at least 10 nm of separation to present a steady state peeling process. All forces are reported as mean values \pm 95 % confidence limit, resulting from averaging mean peeling forces from multiple experiments on a given sequence. The number of experiments used in this analysis is specified individually in each case.

4.3 Results and Discussion

4.3.1 Equilibrium Peeling Model^d

In the course of the tip retraction from the surface, force *versus* distance traces for tips modified with oligonucleotides displayed characteristic plateaus with abrupt force jumps to a progressively lower adhesive force. We interpreted this retraction behavior as steady state peeling that is occasionally interrupted by complete detachment of one or more molecules. Figure 4.1a shows an idealized example of such a peeling of a single DNA oligomer from a graphite surface. In this setup, the detachment of the oligomer occurs perpendicular to the substrate surface – a situation that occurs when the adsorbed bases slide freely on the graphite surface.¹⁶³ Figure 4.1b, displays a characteristic force-distance curve of the steady-state peeling process. Our previous SMFS studies of the pyrimidine homopolymer-graphite system have shown that the peeling force is

^d The equilibrium peeling model was derived by Anand Jagota and Dmitri Vezenov.

independent of the detachment rate (in the range of 100-1000 nm/s). Therefore, single molecule peeling proceeds in a quasi-equilibrium manner.¹⁵⁴

An equilibrium model for detachment of a laterally mobile freely jointed chain (FJC) from a flat surface gives the relationship between peeling force, f , and adhesion per unit length, γ , presented by Equation 4.1:¹⁶⁴

$$\Gamma = \ln \left[4\pi \frac{\sinh(F)}{F} \right] \quad (4.1)$$

$F = fb/k_B T$ and $\Gamma = \gamma b/k_B T$ are the dimensionless force and the dimensionless free energy of adhesion per Kuhn segment of length b , respectively. Given the known Kuhn length for single-stranded DNA (ssDNA) and its contour length per base (0.56 nm), one can calculate the binding energy per monomer from the experimentally measured peeling forces. A correction to the model accounting for enthalpic stretching of the backbone at high loads (>10 pN) can be made by using a Kuhn length elongated by a small fraction, f/κ , κ is segment elasticity of ssDNA:

$$F = \frac{fb \left(1 + \frac{f}{\kappa} \right)}{k_B T} \quad (4.2)$$

For the purpose of calculation of the average binding energies, we set the size of the monomer to the distance between phosphorus atoms in the phosphodiester backbone (taken to be 0.56 nm), and used the same Kuhn length and the same segment elasticity for all DNA oligomer compositions.¹⁶⁴ Therefore, using SMFS, the forces needed to peel a ssDNA molecule can be quantified for a variety of sequences and the corresponding average binding energies per base can be compared.

In Equation 4.1, the reference states for determining adhesion have some arbitrary characteristics. We effectively assumed a density of states of one per steradian with the normalization constant. The corresponding term for the adsorbed state was incorporated into the value of the free energy of adhesion per link. We may refine Equation 4.1 to define the free energy of adhesion in a slightly different manner that, we believe, is directly relevant to our experiments and to the thermodynamic quantity one would obtain in an analogous, thermally-driven process. Details of the derivation may be found in Iliafar *et al.*¹⁶⁵ The resulting corrected free energy of adhesion per link is given by equation 4.3.

$$\Gamma' = \Gamma - \ln \left[\frac{w_{3D}}{w_{2D}} \right] = \Gamma - \Delta \ln[w] = \ln \left[\frac{\sinh(F)}{F} \right] \quad (4.3)$$

The $\ln(w_{3D}/w_{2D})$ term in Equation 4.3 gives the minimum adhesion required to hold the chain adsorbed on the surface – a non-zero contribution, because there is an overall gain in the number of microstates (*i.e.* an increase in entropy) when the link goes from a 2D (adsorbed) to a 3D (in solution) state. The adhesion free energy per base is obtained directly from the force peeling data and is the desired property that also determines the thermally-established equilibria between the adsorbed and desorbed homopolymers with no externally applied force.

Alternatively, the relation between force and adhesion free energy can be derived from a worm like chain (WLC) model of a stretched DNA molecule.¹⁶⁶ In the worm like chain model of a polymer having contour length L_c , the force f is given in terms of extension, L , as

$$f = \frac{k_B T}{p} \left(\frac{L}{L_c} - \frac{1}{4} + \frac{1}{4(1-L/L_c)^2} \right) \quad (4.4)$$

p is the persistence length (half of the Kuhn length, or $b=2p$). Using Equation 4.4 to estimate fractional extension $\lambda=L/L_c$, given measured force f , the adhesion free energy (per unit length) can then be expressed as:

$$\frac{\gamma p}{k_B T} - \frac{1}{2} \ln \left[\frac{w_{3D}}{w_{2D}} \right] = \frac{\lambda^2 (3 - 4\lambda + 2\lambda^2)}{4(1-\lambda)^2}; \quad \lambda = \frac{L}{L_c} \quad (4.5)$$

In the worm like chain model, the steady state peeling force and adhesion are given parametrically as $f(\lambda)$ and $\gamma(\lambda)$ with fractional extension λ as a common parameter, thus allowing us to produce explicit numerical γ versus f dependence. A plot of dimensionless adhesion versus peeling force (Γ' versus F) combining both FJC and WLC models (setting $p=b/2$) indicates that adhesion per unit length for WLC polymer is lower by ~15% than adhesion for a FJC polymer in the range of peeling forces observed in our experiments. For consistency with previous work, and since the FJC model should describe ssDNA better than the WLC model (which is more appropriate for the double stranded form) we will continue to use the FJC model here in the interpretation of our force spectroscopy data. In our analysis, we will calculate the adhesion free energy in the sense defined by Equation 4.3 and reinterpret our previously published peeling force data accordingly.

The Kuhn length for single stranded DNA is 0.51-1.0 nm^{147, 154}; thus, we expect the behavior of the DNA strands longer than 20-30 nm (~35-50 bases) to be well represented by a freely jointed chain model. Indeed, the exact statistical mechanical treatment of the single-molecule peeling of a freely jointed chain under force control results in the appearance of a well-developed force plateau for molecules having 15-20

Kuhn segments or longer.¹⁵⁴ The plateau force does not depend on the number of segments according to the model.

The presence of salt decreases the repulsive forces between the negatively charged phosphate groups of the DNA backbone and results in coiling of the chain, improving validity of the free-joined chain approximation for our short (50-100 bases) DNA oligomers.¹⁵⁴ In our previous experiments on pyrimidines, in the absence of NaCl in dilute buffer solutions (ionic strength of 1 to 10 mM phosphate buffer), long range electrostatic repulsion was readily observed as the tip approached the surface, and the effective range of the repulsive forces could be reduced at higher salt concentrations. However, despite the changes in salt concentration, we still observed that the magnitude of the average peeling forces remain virtually unchanged. This observation is consistent with a notion that the peeling forces are due to dominance of non-electrostatic interactions such as van der Waals forces and hydrophobic interactions over the contributions resulting from the electrostatic/double layer interactions between the charged DNA backbone and the graphite surface.¹⁵⁴

4.3.2 DNA Chain Length and Directional Effects on Peeling

To complete our previous description of factors affecting the binding strength of homopolymers, we carried out additional experiments for polythymine using 5'-thiol modified DNA as opposed to 3'-modified DNA in order to study the effect of direction of ssDNA binding to the gold tip and corresponding direction of detachment from the solid. Peeling experiments were completed on 5'-poly(dT₁₀₀) and yielded 78.5 ± 5.0 pN average peeling force (17 experiments with a total of 884 force curves) which is similar to forces previously observed using 3'-poly(dT₅₀) functionalized tips (85.3 ± 4.7 pN).¹⁵⁴ Figure

4.1b shows a typical force-distance curve obtained for 5'-poly(dT₁₀₀) in pH 7 phosphate buffer with 100 mM NaCl. The only readily detected difference between 5'-poly(dT₁₀₀) and 3'-poly(dT₅₀) peeling was that the length of the peeling steps were as long as 45 nm for the case of the 5'-poly(dT₁₀₀). This is expected for a ssDNA molecule having a contour length of about 55 nm. The 5'-poly(dT₁₀₀) chains displayed a peeling force lower than previously reported for 3'-poly(dT₅₀) by Manohar *et al.*¹⁵⁴ According to Welch's t-test,¹⁶⁷ the peeling forces between 5'-poly(dT₁₀₀) and 3'-poly(dT₅₀) are statistically the same with a 95% confidence interval. The difference appears minor compared to the overall binding force. The lack of an effect on the directionality and chain length on the average peeling force supports our use of the freely jointed chain model. Previously, it was shown that the direction of attachment of the DNA also has no effect on the forces to unbind complementary DNA base pairs.²²

4.3.3 The Contribution of Hydrophobic Interactions to Peeling Forces

To support our interpretation of the dominant role of hydrophobic interactions between the DNA bases and the surface of graphite to peeling forces, we also carried out single molecule peeling experiments using 5'-poly(dT₁₀₀) and model surfaces at extreme ends of the hydrophobicity scale (hydrophobic methyl-terminated self assembled monolayer, dodecane thiol, and a hydrophilic surface self assembled monolayer, mercaptoundecanoic acid). When peeling experiments were carried out on the acid terminated monolayer using either DNA-modified or MHA-modified AFM probes, the force *versus* distance curves displayed pure repulsion and had no peeling (similar to our control experiments without DNA on the probe). On the contrary, when the same DNA-

modified AFM probes were used on a methyl terminated monolayer, steady-state peeling plateaus were observed with an average peeling force of 60.6 ± 5.9 pN (three experiments with a total of 164 force curves). The magnitude of the peeling force on a hydrophobic monolayer is evidence that the peeling forces of DNA on graphite must be dominated by hydrophobic interactions. The differences in the interaction strength between the DNA and monolayers must be a result of differences in the chemical nature of the substrate since both monolayers have similar chain lengths and are known to produce organized monolayers.

To further support the fact that the DNA peeling interaction on graphite is dominated by hydrophobic interactions, we carried out peeling experiments with 5'-poly(dT₁₀₀) on graphite at temperatures between 25-40°C. Within this temperature range, the peeling force remained approximately constant (Figure 4.2a). If the interaction between the peeling force of DNA and graphite is largely hydrophobic, we would not expect a large change in the peeling force with a change in temperature. At room temperature the hydrophobic effect is dominated by entropy due to the structuring of water near hydrophobic interfaces (*i.e.* graphite and DNA molecule). As the temperature of the solution is increased, the increase in the entropy of the system is balanced out by an increase in the molar enthalpy, resulting in very little change in the overall Gibb's free energy.¹⁶⁸ Therefore, the overall free energy of interaction between hydrophobic surfaces is nearly constant. Experimentally, this can easily be tested by measuring the adhesion forces on a teflon thin film as the temperature is increased (Figure 4.2c). The adhesion force between a silicon probe on a teflon thin film is nearly constant between 25-50°C. Other SMFS studies have determined that the hydration energy of polystyrene in water is

largely unchanged as the temperature increases from 20-80°C.¹⁶⁹ While DNA does not form a globular conformation on the surface of the graphite, similar peeling plateaus were observed for hydration of polystyrene. We can consider DNA in our peeling experiments as a single molecule polymer being rehydrated as it is pulled from the surface of graphite.

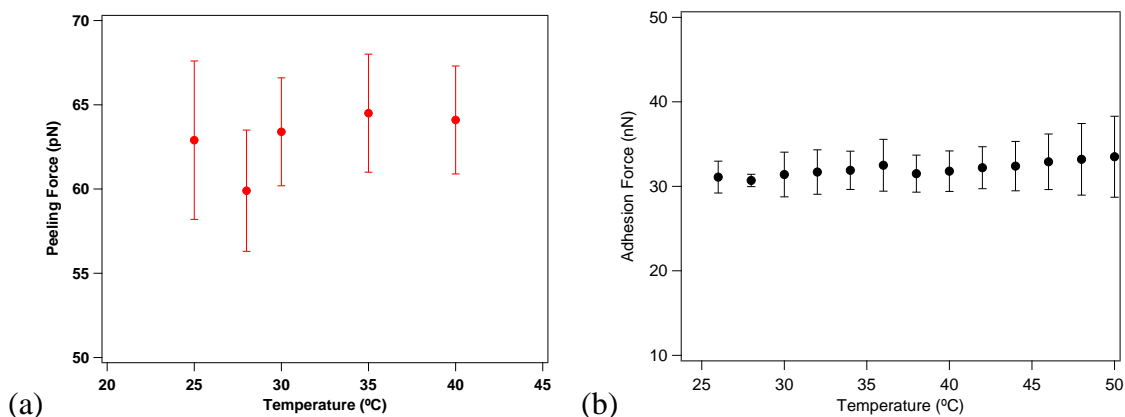


Figure 4.2. (a) Peeling forces of 5'-poly(dT₁₀₀) on graphite from 25 to 40°C. (b) Adhesion forces of a silicon probe and teflon thin film in water in the temperature range of 25 to 50°C. Error bars are the standard deviation of the forces.

4.3.4 Interaction Strength of Purines on Graphite

For the study of purine homopolymers, we investigated peeling forces for 3'-poly(dA₅₀) and 5'-poly(dG₁₀₀). We decided to use longer chains for polyguanine since a longer contour length increases the success rate of peeling. We found that using a longer chain (100mer *versus* 50mer) diminishes the effect of strong tip-surface contact adhesion, and makes identification and interpretation of plateaus due to DNA peeling a more robust process. The average plateau force for peeling 3'-poly(dA₅₀) from graphite was determined to be 76.6 ± 3.2 pN (25 experiments with a total of 1185 force curves). From comparison of the peeling forces of 5'-poly(dT₁₀₀) with that of 3'-poly(dA₅₀) – 78.5 pN *versus* 76.6 pN, it is clear that the effective strength of interactions with graphite fall

within the same range. Given the accuracy of cantilever spring constants obtained from the thermal calibration method ($\sim 10\text{-}20\%$ error)^{170, 171} and the typical width of the peeling force distribution in a given experiment (5-15 % of the mean), the binding energy of poly(dT) and poly(dA) cannot be distinguished from one another.

If one accepts the view of the dominant contribution of hydrophobic forces to the binding affinity between the bases and graphite, the closeness of the two values is surprising, since the maximum contact area between adenine and graphite is higher than between thymine and graphite. Indeed, affinity to graphite of individual bases scales according to the size of the respective heterocycles.¹⁵³ This discrepancy in binding between free and constrained bases is an indication of the possible influence of the DNA backbone on the conformation that an adsorbed base can adopt on a graphite surface. Constraints imposed by the backbone of purine homopolymers prevent conformational changes that would result in maximum contact areas and highest interaction energies between the bases and graphite surface.¹⁷²

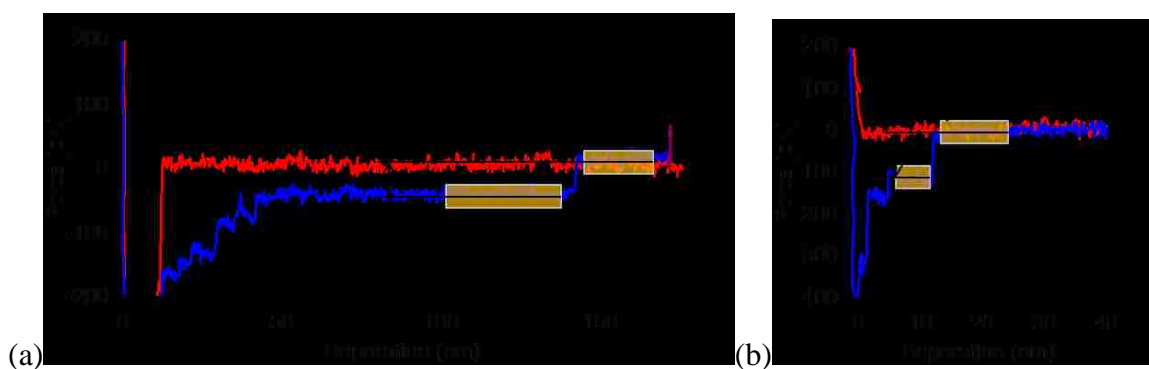


Figure 4.3. Force-distance curves obtained for probes functionalized with 5'-poly(dG₁₀₀) displaying peeling at separation longer than the oligomer contour length, (a), and short-ranged, high force peeling, (b). Orange boxes highlight areas that were used for averaging to determine the peeling force.

Force-distance curves for peeling 5'-poly(dG₁₀₀) from graphite consistently showed behavior different from what we observed for the other three homopolymers (Figure 4.3). In general, the peeling steps for polyguanine displayed large separations (greater than the contour length of the strand) with small peeling forces (<60 pN), or small separation of the last peeling step (less than half the contour length) with large peeling forces (>100 pN). Since polyguanine has a propensity to form secondary structures,¹⁶¹ we suggest that these features are caused by different modes of peeling or states of adsorbed polyguanine, leading to the variability in peeling force magnitude and the shape of force-distance curves.

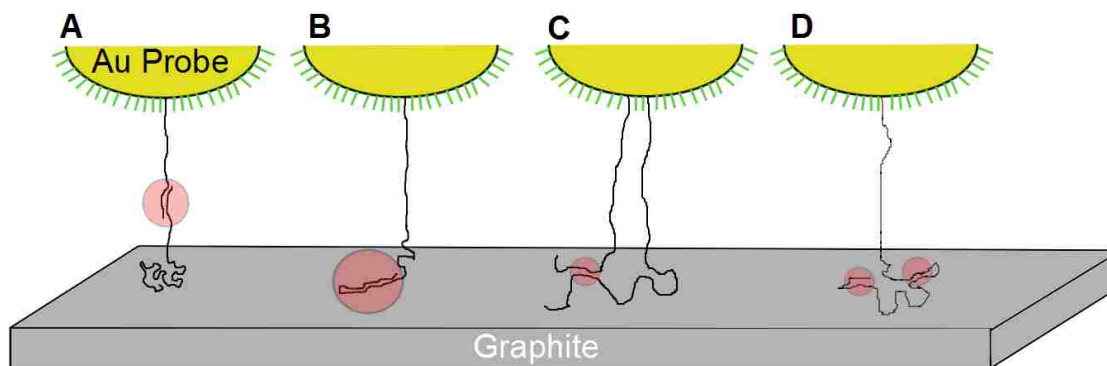


Figure 4.4. Proposed mechanisms to describe the possible reasons for observing: (A) force curves with small forces at separations larger than the ssDNA's contour length, (B) large forces at short separations, (C) and (D) both peeling and stretching of secondary structures. Red circles highlight areas of potential poly(dG) secondary structures.

We envision several modes of peeling for 5'-poly(dG₁₀₀) that are consistent with our observations and imply formation of stable secondary structures as outlined in Figure 4.4. For example, Figure 4.4A shows that formation of a stable dimer molecule would result in the final separation step being larger than the contour length of the individual homopolymer molecule. Strands with stable intrastrand secondary structure adsorbed onto the surface (Figure 4.4B) could explain observation of large peeling forces at much

smaller separation distances. Furthermore, it is proposed that the formation of inter- and intrastrand secondary structures at random locations along the chain led to strong adsorption of the polymer at these locations and formation of pinning points resulting in characteristic stretching behavior (Figure 4.4C and D, see appendix for example force curves). Figure 4.5a shows groupings in different modes of peeling in a force *versus* distance scatter plot for the peeling of 5'-poly(dG₁₀₀).

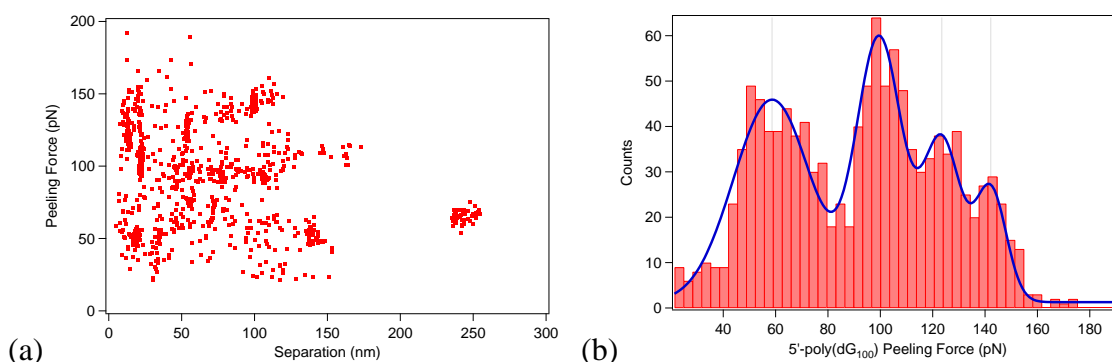


Figure 4.5. (a) Peeling force *versus* separation distance scatter plot for several probes functionalized with 5'-poly(dG₁₀₀) and (b) Histogram of the peeling forces for the same series of 5'-poly(dG₁₀₀) probes displaying several peeling regimes. We assume that the peak at 63.8 ± 14.3 pN corresponds to the steady-state peeling a single poly(dG) oligomer. Higher forces are due to peeling of poly(dG) secondary structures.

Simply averaging all the force steps obtained from the 5'-poly(dG₁₀₀) results in a large variation in peeling forces. However, compiling all the results into a histogram (Figure 4.5b), reveals several different peeling regimes. We interpreted the lowest peak (63.8 ± 14.3 pN, 17 experiments with a total of 1207 force curves) as the steady-state peeling force of a single 5'-poly(dG₁₀₀) oligomer absent of secondary structures, while the latter peaks are a result of secondary (intra- or interstrand) structures. As with the interaction strengths of poly(dT) and poly(dA), the average peeling force of 5'-poly(dG₁₀₀) and 3'-poly(dC₅₀) are of similar magnitude and are statistically

indistinguishable from each other within our experimental error. On the other hand, it is clear that the binding force of poly(dT) and Poly(dA) are larger than that of both poly(dG) and poly(dC).

Table 4.1. Summary of all SMFS measurements of binding affinity between DNA homopolymers and graphite (\pm 95% confidence). The calculated binding energy was determined using equation 4.3.

Sequence	Peeling force (pN)	Binding energy per nucleotide (k _B T)
<i>Pyrimidines</i>		
3'-poly(dT ₅₀) ³³	85.3 \pm 4.7	11.3 \pm 0.8
3'-poly(dC ₅₀) ³³	60.8 \pm 5.5	7.5 \pm 0.8
5'-poly(dT ₅₀)	73.4 \pm 5.5	9.4 \pm 0.9
5'-poly(dT ₁₀₀)	78.5 \pm 5.0	10.2 \pm 0.8
<i>Purines</i>		
3'-poly(dA ₅₀)	76.6 \pm 3.0	9.9 \pm 0.4
5'-poly(dG ₁₀₀)	63.8 \pm 1.3	7.9 \pm 0.2

4.4 Conclusions

In this paper, we report the direct measurement of the interaction forces for a complete set of homopolymer sequences between DNA and a graphite surface (Table 4.1). Herein, we found that the DNA chain length and its direction of attachment to a gold coated AFM tip have negligible effects on the peeling forces of homopolymers. The force required to detach 3'-poly(dA₅₀) from a graphite surface was measured to be 76.6 \pm 3.0 pN, while that of 5'-poly(dG₁₀₀) was found to be 63.8 \pm 14.3 pN. Moreover, the experiments with 5'-poly(dG₁₀₀)/MHA functionalized gold tips showed peeling and stretching behavior suggestive of the formation of secondary structures. Overall, the binding energies for all four bases are in the range of 8-11 k_BT. With these results, it is

clear that polythymine and polyadenine fall within the same range in terms of their binding strength, while polycytosine and polyguanine can also be coupled into a single group in terms of their binding affinity to graphite.

The binding energy does not scale with the size of the base as in the case of individual nucleobases or nucleosides, possibly indicating an important role of the restrictions placed by the phosphodiester backbone on conformations of the DNA bases on graphite. While there is a correlation between binding energy and non-polar molecular area (see appendix), we believe that this trend is likely coincidental given that for single bases both experiment and theory show good scaling with the total area of the base. Since we are measuring the difference in free energy of the bound and unbound states, these arguments imply that we ignore stacking of bases to each other in the unbound state (purine-purine stacking will be stronger than pyrimidine-pyrimidine stacking). No base stacking assumption in the desorbed state seems plausible given that the DNA backbone should be almost fully stretched under the high peeling forces (> 60 pN). Therefore, desorbed nucleobases cannot stack, because they will be too far apart. On the other hand, the stacking of the bases in the adsorbed state is plausible and would be consistent with the lower than expected binding energy for purines. To explore the possible contribution from this effect, one would likely have to rely on very detailed molecular mechanics calculations, but we note that simulations of ssDNA sequences on carbon nanotubes show very little propensity for base-base stacking.¹⁷³

The SMFS studies described here, where ssDNA is adsorbed onto a two-dimensional substrate, used basic homopolymer sequences that are not capable of forming special recognition 3D-structures when wrapped around a SWCNT, such as

poly(dTdAdTdT), poly(dGdT),¹⁷⁴ and others,³ that are found to play a significant role in ssDNA/CNT interactions when placed in bulk dispersions. In order to overcome this shortcoming, future experiments should be conducted to assess the role of different bases within the same strand. Rational design of secondary structures to probe their effect on the magnitude of the interaction forces is fully compatible with SMFS and can provide further quantification of the binding strength between various DNA motifs and solid surfaces. The potential drawback of using SMFS to uncover sequence dependent signatures due to recognition motifs is the relatively high (in the context of this system) variability of the typical force calibration methods employed with force microscopy. The problem may be alleviated by the design of the proper internal standard built into the oligomer sequence or by further improvements to force probe calibration. The role of the high curvature and size matching of the CNT on the magnitude of the binding forces between DNA and CNT remains unknown and can only be assessed with experiments on actual nanotubes.

4.5 Appendix

4.5.1 Correlation between binding free energy per base and non-polar molecular area.

We used ChemBio3D Ultra 12.0 program (PerkinElmer Informatics) to calculate molecular (van der Waals) area and polar molecular area for each nucleobase. The non-polar molecular area is then found as the difference between the two calculated areas.

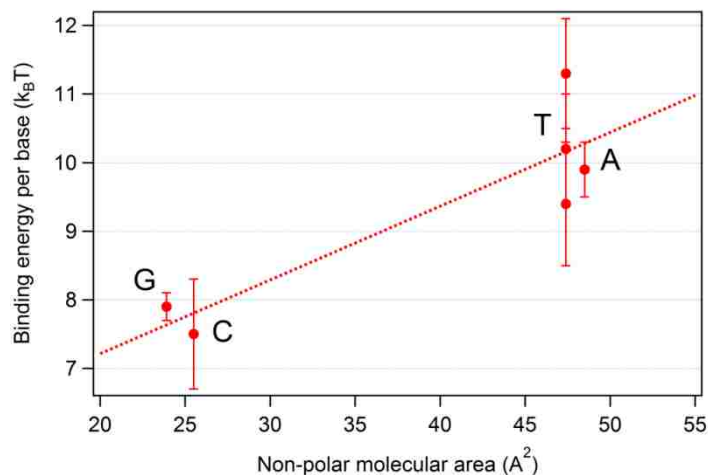


Figure 4.6. Dependence of binding free energy per nucleotide on non-polar molecular area of a nucleobase. The dotted line is a fit to the data.

4.5.2 Stretching Behavior of poly(dG)

Figure 4.7 displays representative peeling and stretching curves for 5'-poly(dG₁₀₀).

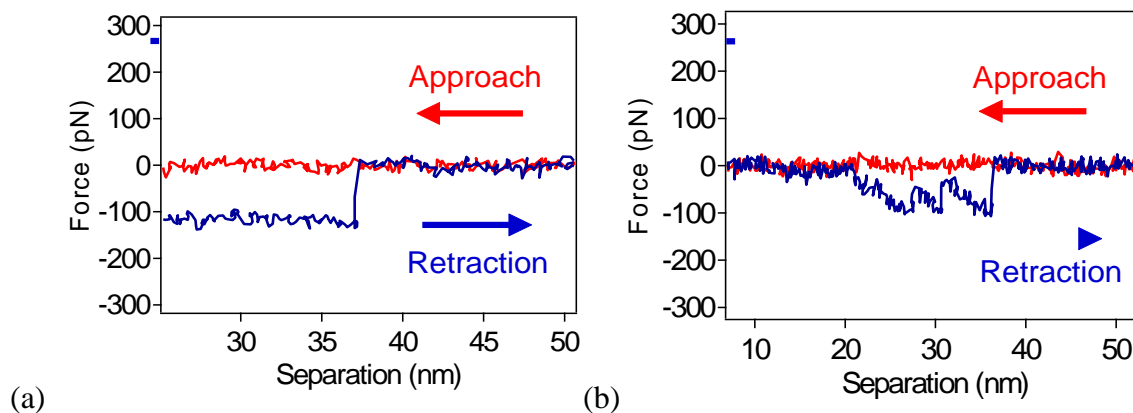


Figure 4.7. Typical force-distance curves obtained for probes functionalized with 5'-poly(dG₁₀₀) (200 nm/s retraction velocity, 10 mM phosphate buffer with 100 mM NaCl) showing peeling (a) and stretching (b).

Chapter 5 Measuring the Interaction Strength of DNA Oligomers on Suspended Carbon Nanotubes – A Comparison to 2D Substrates

5.1 Introduction

In Chapter 4 we determined that the interaction strength of the homopolymer oligomers with graphite can be ranked as: $T \geq A > G \approx C$. We also determined that the peeling force is independent on the length and direction of peeling of the oligomer. Overall, our experimental ranking is inconsistent with previous experiments on individual nucleobases and nucleosides as well as simulations on oligomers. The simulations have shown that the binding strength of homopolymers to graphite follow the ranking, $T > G > A > C$,^{133, 155} which is different than that of individual nucleotides obtained from solution studies, $G > A > T > C$,¹⁵⁶⁻¹⁵⁹ or of nucleobases and nucleosides determined by isothermal titration calorimetry, $G > A > C > T$.¹⁶⁰ For single base adsorption experiments, the interaction strength is correlated to the size of the base, while for our peeling experiments, the peeling forces did not scale with the size of the base. We hypothesize that the difference in the interaction strengths may be caused by constraints due to the phosphodiester backbone on the possible conformations DNA may adopt on a flat substrate (*i.e.* the bases cannot freely optimize pi stacking with the substrate).

In the case of poly(dT), we also determined that the peeling force must be largely dominated by hydrophobic interactions since the magnitude of the peeling forces on a hydrophobic monolayer was ~80% of the magnitude of peeling forces on graphite. In addition, the peeling forces on graphite were independent of temperature and ionic strength of the solution. Comparing the peeling forces between poly(dT) and poly(dC), where the bases differ by a single methyl group, we were able to individually distinguish

the peeling forces on graphite. Similarly, we could also distinguish the peeling forces between poly(dA) and poly(dG). However, we could not individually resolve the peeling forces of each base individually.

In previous experiments, a graphite substrate was used as a simple, analogous substrate to simulate the interactions that the DNA would experience with the surface of a carbon nanotube (CNT). Graphite should serve as a reasonable substitute for CNTs since the DNA only interacts with the top surface of graphite (effectively graphene) and CNTs are rolled up sheets of graphene. However, it has been shown through high resolution imaging⁴² and simulations⁴³⁻⁴⁶ that DNA wraps around the outside of a CNT in a helical fashion. Tu *et al.* have shown that ‘special’ sequences with simple pyrimidine repeats (T or C) with periodic purine insertions (G or A) can display structural recognition of CNTs.⁴⁴ These ‘special’ sequences are capable of forming stable 2-dimensional sheets (similar to a β -sheet) on flat surfaces such as graphite through hydrogen bonding. On 3-dimensional structures, such as a CNT, these stable sheets may be wrapped into a stable barrel structure (Figure 5.1). The helical DNA-CNT complex orients such that the bases interact with the surface of the CNT and the phosphate backbone is exposed to the solution. The flexibility of the backbone allows for bases to alternate sides of the backbone to maximize interactions.⁵⁵ The entropy loss due to the arranging of the backbone is much less than the interaction strength between the base and the CNT.⁵⁵ For recognition sequences, it is hypothesized that there is a single, stable barrel structure to pair with a given (n,m) CNT chirality. The simulation and suspension experiments from Tu *et al.* used multiple, short oligomers which is not experimentally feasible for single molecule force spectroscopy.

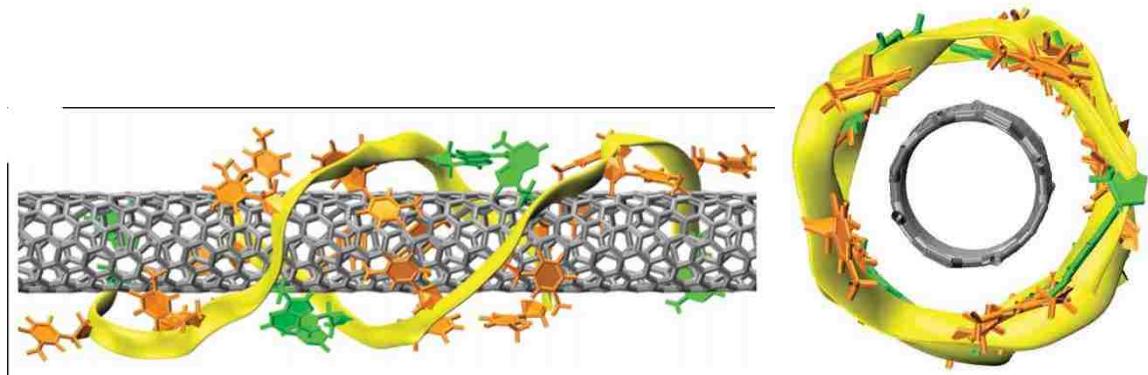


Figure 5.1. Simulation results displaying stable barrel formation of three hydrogen bonded anti-parallel ATTTATTTATTT strands on the surface of a (8,4) CNT.⁴⁴

Due to planar constraints, the oligomers cannot achieve the same 3-dimensional conformations on graphite as is possible on a CNT. An ideal experiment to measure the true interaction between DNA and CNTs would require a substrate where the DNA could freely interact with a CNT without interferences due to the supporting surface. Therefore, we need to produce a sample with freely suspended CNTs. Naturally, one can envision two possible methods to remove DNA from a CNT – *i.e.* application of either perpendicular or parallel forces with respect to the nanotube (Figure 5.2). There are also two conformations that the DNA can adopt in both cases: wrapped and co-axial alignment (the latter being similar to interactions on a graphite surface). There exists a variety of methods to prepare both samples in Figure 5.2, such as chemical vapor deposition,¹⁷⁵⁻¹⁷⁹ meniscus alignment,¹⁸⁰⁻¹⁸² self-assembly techniques through covalent or ionic attachment,¹⁸³⁻¹⁸⁵ and anchoring with biomolecules.^{186, 187} In the case of horizontally oriented tubes, lithographic processes are required to suspend the tubes. There are several important factors that are required for production of an ideal sample suitable for experiments on peeling DNA from CNTs: i) the surface of the CNT must be free of

surfactants or chemical modifications, ii) CNT chirality should be controlled, iii) CNTs must have a strong enough interaction with the substrate so that they are not removed from the substrate during fluid exchanges or through interactions with the AFM tip, and iv) there must be a high enough concentration of suspended CNTs to get statistically significant results.

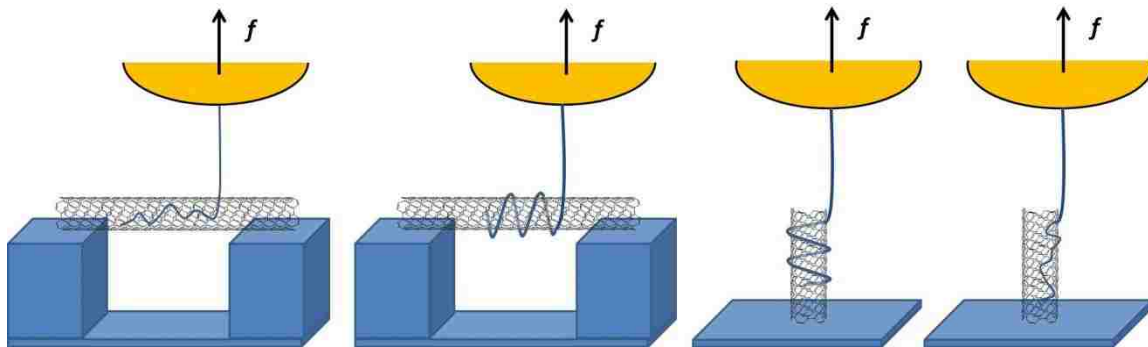


Figure 5.2. Schematic representation of perpendicular peeling of DNA from horizontally suspended CNTs (left) and parallel peeling from vertically oriented CNTs (right). Each peeling type may occur with or without wrapping around the CNT. Figures are not drawn to scale.

Noy and colleagues have completed experiments where oligomers were pulled out of vertically oriented CNT pores.¹⁸⁸ Their experiments produced seemingly inconsistent results to those described in Chapter 4 – the forces required to remove 3'-poly(dA)₆₀ was almost 5 times larger than the forces we measured on graphite and the interaction forces were dependent on the salt concentration. However, as with graphite, pulling DNA inside of a CNT pore is a frictionless process, or at least the friction forces are not experimentally measurable. One would expect that the external surface of the CNT would also produce frictionless sliding with DNA, so experiments with vertically oriented tubes may not be capable of disrupting unique intrastrand interactions (*i.e.* the oligomer may slide off of the surface of the CNT in a single wrapped conformation if there is

insufficiently strong interactions or attachment to the surface of the CNT). Therefore, we find it more interesting to analyze the perpendicular removal of DNA from horizontally suspended CNTs, where intrastrand hydrogen bonds must be broken during the course of the peeling process.

The literature describes several procedures to attach CNTs with chemically modified ends to a substrate by self-assembly.^{183, 186, 189-192} We were able to attach acid-modified CNTs to photolithographically patterned substrates to produce horizontally suspended CNTs for DNA removal. Due to the high resolution and robustness of the procedure, we will continue to use single molecule force spectroscopy to measure the peeling forces of oligomers from suspended CNTs. For oligomers in which intrastrand interactions are present, interesting features were observed during the retraction curves instead of smooth peeling plateaus. Once again, as a shorthand notation in this chapter, an oligomer naming convention is used where the point of attachment to the probe is listed first and the number of bases in the oligomer chain is signified by a subscript.

5.2 Methods

5.2.1 Probe Functionalization

AFM probes (ContGB gold coated AFM probes with normal spring constant ~ 0.3 N/m (Budget Sensors, Inc., Sofia, Bulgaria) were functionalized with the same procedure described in Section 4.2.2. Briefly, probes were cleaned in air plasma for 1 minute and then rinsed with ethanol and water. Then, probes were placed in a 0.1 nM solution of DNA in 10 mM phosphate buffer with 1 M NaCl (pH ~ 7) for 1 hour. The DNA was previously deprotected with 6 mM TCEP for 30 minutes. After removal from the DNA

solution, probes were rinsed with water and ethanol and placed in a 15 mM ethanolic solution of mercaptohexanoic acid (MHA). Probes were rinsed with ethanol and water and kept in 10 mM phosphate buffer until use.

5.2.2 Force Calibration and Force Curve Capture

Force spectroscopy measurements were performed using an MFP-3D atomic force microscope (Asylum Research, Santa Barbara, CA). The CNT substrate was placed in a fluid cell, which was then filled with approximately 3 mL of 10 mM phosphate buffer with 100 mM NaCl. Probes were calibrated at the end of each experiment to avoid damaging the DNA or the gold coating under heavy compressive loading. The deflection sensitivity for each AFM cantilever in fluid was calibrated by determining the slope of the linear compliance region of the force-distance curves taken with the graphite sample. The thermal spectrum was recorded in fluid and fit with a Lorentzian curve for calculation of the spring constant, as described in Chapter 2.¹⁹³

DNA peeling forces were measured using a force-volume map over a $10\ \mu\text{m} \times 10\ \mu\text{m}$ area (32×32 grid of force-distance curves) with a force rate of 200 nm/s and a maximum compressive load of $<5\ \text{nN}$. The maximum applied force was limited in order to protect the DNA from damage at high compressive loads. Force curves were also recorded with a tip dwell time at the sample surface for up to a second to allow more time for the DNA to reach an equilibrium orientation on the surface of the CNT. Analysis of the force-distance curves was performed using a custom code written in IGOR Pro (Wavemetrics, Eugene, OR). This code averages the force measured over a distance of at least 5 nm on both sides of the molecule detachment step and determines the peeling

force by taking the difference. Only force curves recorded over the trenches areas were considered for analysis of the peeling forces on suspended CNTs.

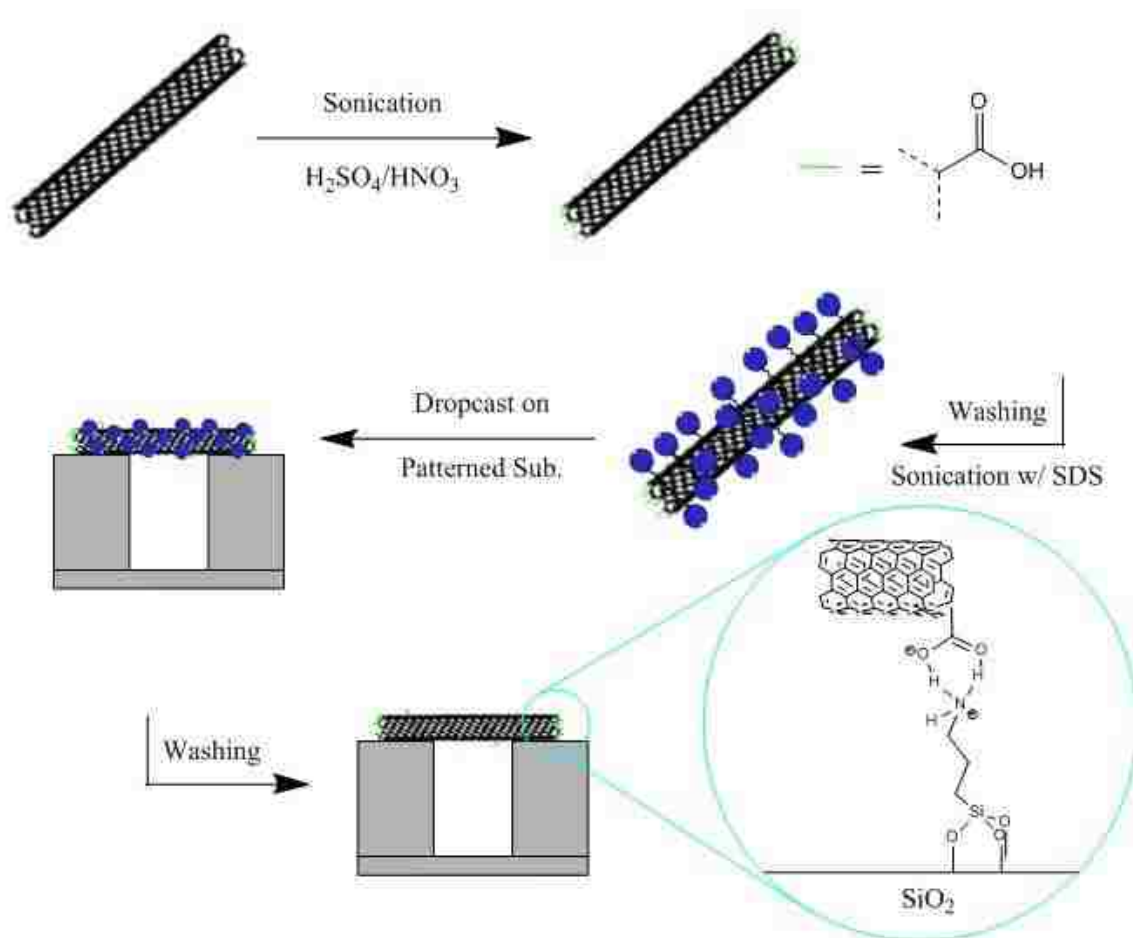


Figure 5.3. Chemical modification of CNT by sonication in strong acid. Acid-modified CNTs were suspended with SDS and applied to an APTES modified surface. The acid group at the terminus of the CNT produces an ionic bond (likely stabilized with hydrogen bonding) with the APTES surface. Figure not drawn to scale.

5.2.3. Preparation of Acid Modified Carbon Nanotubes

The CNTs were functionalized with a terminus acid group using a slightly modified procedure published by Liu *et al.*¹⁸³ Approximately 2 mg of CoMoCAT (6,5) CNTs (Sigma Aldrich, St. Louis, MO) were sonicated in a bath sonicator for 2 h in 4 mL

of a 3:1 mixture of concentrated sulfuric acid and 70% nitric acid. The solution was neutralized by washing by 3x times centrifugation at 21130 relative centrifugal force (rcf) for 1 minute with water. Under centrifugation, the carbon nanotubes (and byproducts) made a pellet at the bottom of the centrifuge tube and the clear supernatant was discarded. The pH of the solution after washing was ~6.

The washed CNTs were resuspended in 20 mL of water with 2 mg of sodium dodecyl sulfate (SDS) by sonication in a bath sonicator for 30 minutes. The suspension was centrifuged again at 21130 rcf for 1 minute and the clear, grey supernatant was kept for future experiments. The CNT suspension was stable for days. The addition of SDS not only helped to create a stable CNT suspension, but also helped to remove some of the byproducts from synthesis (*i.e.* catalyst and other carbonaceous material) and separate CNT bundles. The complete modification process of the CNTs is shown in Figure 5.3.

5.2.4. Substrate Preparation

Silicon wafers with a 300 nm thick thermally grown oxide (University Wafer, South Boston, MA) were patterned with 1 μm wide trenches separated by 2 μm using photolithography. SU-8 2000 photoresist (Micro Chem, Newton, MA) was applied to the substrate by a programmed spin coating process at 280 rpm for 20 seconds, 500 rpm for 10 seconds, and 4000 rpm for 30 seconds. Photoresist was prebaked at 65°C for 1 minute and 95°C for 10 minutes. Samples were patterned with a 10 second long UV exposure followed by a postbake at 65°C for 1 minute and 95°C for 10 minutes. The SU-8 was developed in SU-8 developer solution (Micro Chem, Newton, MA) for 1 minute followed by washing with isopropyl alcohol. The exposed oxide was etched using reactive ion

etching with a CF_4 gas at 250 mTorr for 4 minutes to remove all 300 nm of oxide (the etch rate of the silicon oxide is much faster than silicon, so the etching effectively stops once it reaches the silicon surface). The SU-8 was removed with piranha solution (70% concentrated sulfuric acid and 30% of 50% hydrogen peroxide by volume).

Substrates were functionalized with 3-aminopropyltriethoxy silane (APTES, Sigma Aldrich, St. Louis, MO) using a procedure previously described by Howarter *et al.*¹⁹⁴ The clean trench substrates were placed in a solution of 10% APTES by volume in toluene for 1 hour followed by rinsing with toluene, methanol, and water. The APTES surfaces were then placed in water for 24 hours to complete the hydrolysis of any unbound ethoxy groups. The APTES coated trench patterns were completely covered with the acid modified CNT suspension and were dried by evaporation at room temperature. The substrates were thoroughly rinsed (30 seconds of rinsing with a wash bottle) with water and ethanol to remove SDS from the CNT surface. The photolithography process is shown in Figure 5.4.

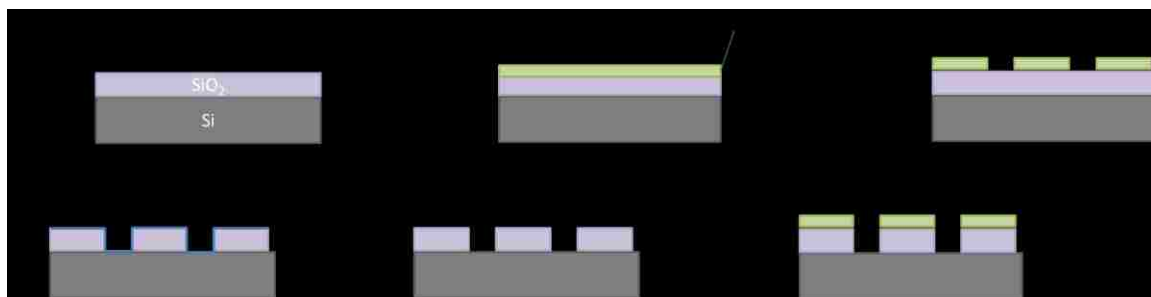


Figure 5.4. Photolithography procedure to produce 1 μm wide and ~ 300 nm deep trenches on thermally grown silicon oxide. Figure not drawn to scale.

5.3 Results and Discussion

5.3.1. Preparation of Suspended CNT Substrate

The process of functionalizing the open ends of CNTs with carboxylic acid groups etches the tubes from the ends and also attacks defect sites on the surface of the CNTs to cut the tubes and create new ends.^{22, 29} We shortened the sonication time from the described procedures to ensure long tubes that could span 1 μm wide trenches. It is important that the overall tube functionalization process does not modify the surface chemistry of the CNTs – especially considering that the primary interaction between DNA and CNTs is hydrophobic in nature and addition of hydrophilic acid groups would weaken the strength of the interaction. While there is likely a population of tubes with some defect sites with substituted acid groups where tube cutting was not completed (due to the reduced sonication time), literature suggests that the acid primarily attacks the tube ends.^{183, 190} After acid functionalization, the CNTs became more soluble in water and produced suspensions that were stable for minutes. Addition of SDS not only aided in producing a more stable CNT suspension, but also helped to break up bundles and separate CNTs from synthesis byproducts.

Overall, the attachment of acid modified CNTs is a versatile preparation method for future experiments. Modification of the sonication time can produce various lengths of tubes depending on the desired nature of the experiment. It has been shown that short, acid modified tubes can also be oriented vertically on the substrate surface for experiments with parallel peeling as described in Figure 5.2.^{184, 190, 195} Uniformity of the chirality of the CNT substrate may also be finely controlled by starting with a known commercial CNT sample or use of a chromatographically purified suspension. While

chemical vapor deposition growth of CNTs can largely produce a single tube diameter with careful control of the catalyst conditions,^{176, 177, 196-198} the described preparation can be completed with the same procedure simply by substitution of the starting selection of CNTs.

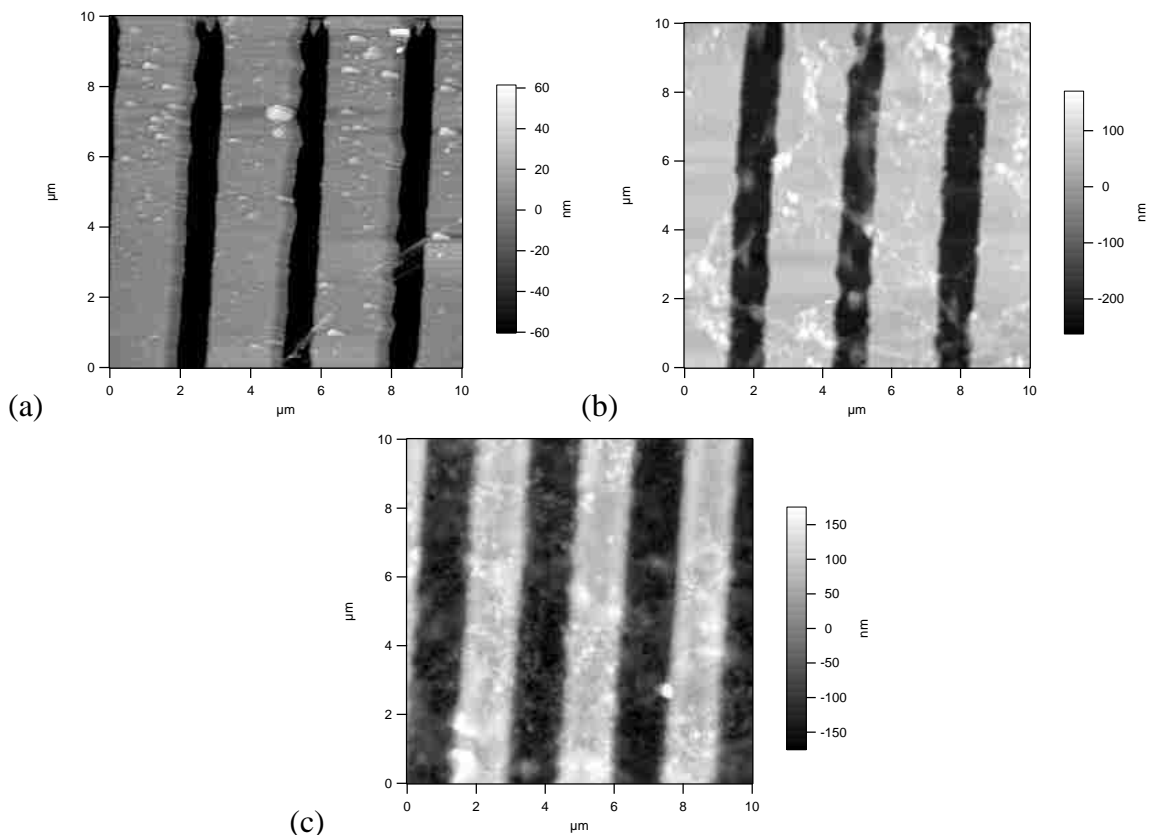


Figure 5.5. Varying substrate tube densities based on the deposition procedure, (a) soaking in CNT suspension for 2 hours, (b) dip coating from CNT suspension, and (c) drop casting of CNT suspension. Images were captured using tapping mode imaging in air. The blurriness in the images is likely due to the CNTs swinging due to contact from the probe during imaging.

The CNTs were successfully attached horizontally with their acid terminated ends pinned to patterned APTES substrates. The tubes remain anchored on the substrate surface after extensive washing with water and ethanol. Robustness under liquid

exchange is a requirement for these experiments, since the SDS must be removed from the surface of the CNTs for force spectroscopy experiments. If SDS remains on the surface of the tube, previous experiments have displayed that this surface chemistry will affect the interactions between DNA and the CNT surface.¹⁹⁹ Modified CNTs could be placed on the substrate surface in a variety of methods to alter the surface density, *i.e.* soaking, dip coating, or drop casting suspensions of various concentrations. Soaking the APTES substrate in the CNT suspension resulted in a very low density of CNTs on the sample surface. This low coverage is likely due to the fact that adsorption of the tubes from a stable suspension to a planar surface is a slow, unfavorable process.¹⁸⁴ Thus, methods such as dip coating and drop casting helped to directly drive tubes to the substrate surface resulting in an increase in CNT density. Experimentally, the surface density of CNTs is a tradeoff: while it would be ideal to have repeated force curves measured on the same CNT, due to the delicate nature of DNA attachment to the probe, imaging to locate a single tube is inaccessible. We have regularly observed detachment of the DNA from the surface of the probe after imaging or under compressive loads of several nanonewtons.

Figure 5.5 displays several AFM images of the suspended CNTs from the above preparation methods. Overall, it appears that the tubes are suspended over the trenches – other than the observation of the height image, the tubes seem blurry due to swinging when contacted by the AFM probe (thus making clear images difficult to obtain). Due to the preparation methods, it is also expected for the suspended tubes to have slack across the trenches.⁴⁰ Experimentally, this could cause peeling plateaus to exceed past the contour length of the DNA.

5.3.2. Oligomer Peeling on Suspended Tubes

Peeling of DNA from CNTs is conceptually more interesting and experimentally more challenging than our peeling experiments on graphite. By performing experiments directly on CNTs, we are able to directly probe the natural, 3-dimensional conformation of the DNA unwrapping from the surface of the CNT. Previously, we recorded force maps on the surface of graphite in order to obtain an appropriate average peeling force that was not skewed by surface defects or atomic steps in the surface of the graphite. Here, we are performing force maps in order to locate suspended CNTs. It is possible to reconstruct a height image of the substrate surface from force maps - Figure 5.6a shows a reconstructed height image where lithographic trenches may easily be identified. The tube deposition method needs to provide a high enough density in a 10 μm area that several suspended CNTs should be located within a force map. Force curves highlighted in Figure 5.6b displayed peeling plateaus. Notice that most force curves displaying peeling plateaus are generally not isolated and can be traced through a connected network, likely mapping the location of CNTs on the substrate surface.

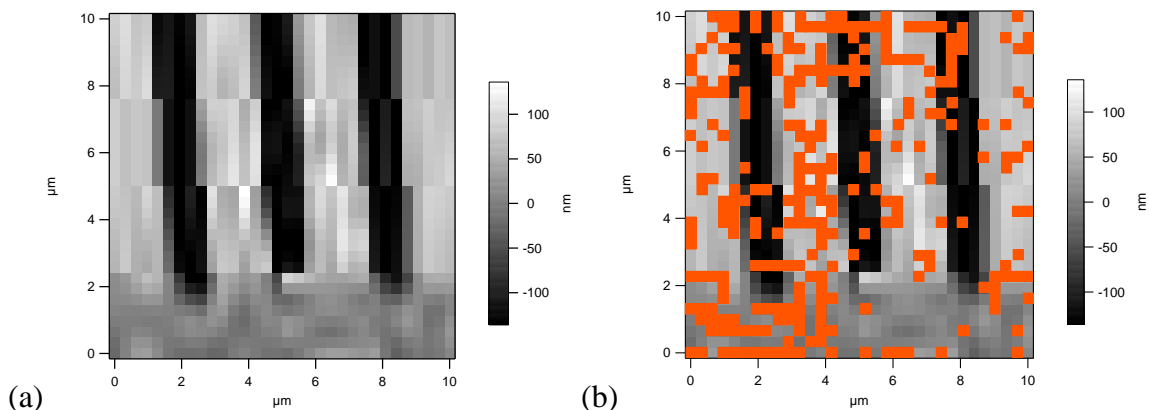


Figure 5.6. (a) Representative image of the reconstructed height from a 32x32 force map of 5'-poly(dG₁₀₀) peeling on a suspended CNT sample. (b) Areas highlighted in red indicate force curves with peeling plateaus. Note that peeling plateaus are typically not isolated. Some of the highlighted force curves did not display plateaus long enough to calculate the peeling force.

The features present in force curves recorded on suspended tubes still possess a steady-state peeling plateau similar to force curves measured on the flat graphite substrate described in Chapter 4. However, force curves of homopolymer oligomers on suspended CNTs typically show several interesting features that are not present in force curves on graphite: i) the approach section of the force curve shows different repulsive features or changes in slope likely due to interactions with swinging or bending of the CNTs, ii) the adhesion peak typically has added features or stretching likely due to complex multistrand interactions and tube slack, iii) oligomers with stable secondary structures or strong intrastrand interactions have periodic stretching upon retraction, and iv) since there may be slack within the suspended CNT, it is possible for the peeling plateaus to occur at lengths longer than the contour length of the DNA. The slack within the CNT can be visualized by stretching in the retraction curve if there is considerable adhesion between the probe and the CNT (see appendix).⁴⁰ Due to the shape of the extension curves, it

appears that the probe is likely sliding off the side of the suspended CNTs and reaching the bottom of the trench, which is evident by sudden changes in the slope of the extension curve. This assumption seems reasonable considering the diameter of the CNT (~1 nm), the size of the AFM tip (~30 nm), and the spatial resolution of the force map (~300 nm) – the chances of the probe landing centered over a single CNT are low.

In order to verify that the measured peeling forces were originating from DNA-CNT interactions, two control experiments were performed. First, a probe functionalized with MHA was used to complete force maps on the suspended CNT sample (Figure 5.7a). No peeling forces were observed with an MHA probe, but adhesion and interactions due to the suspended CNTs (*i.e.* changes in slope during extension portion of force curve) were observed. It is expected to see adhesion between the negatively charged MHA monolayer and positively charged APTES monolayer. Secondly, to verify that peeling events were not occurring due to interactions with the APTES monolayer or residual SDS, force maps were recorded using 5'-poly(dT₁₀₀) on a trench sample treated with APTES and a 0.1% SDS solution (Figure 5.7b). This produced a trench sample under the same conditions as those used for peeling experiments without the presence of CNTs. Stretching curves were observed on the APTES sample similar to those observed previously.²⁵ It appears that residual SDS is removed from the substrate surface after rinsing with water.

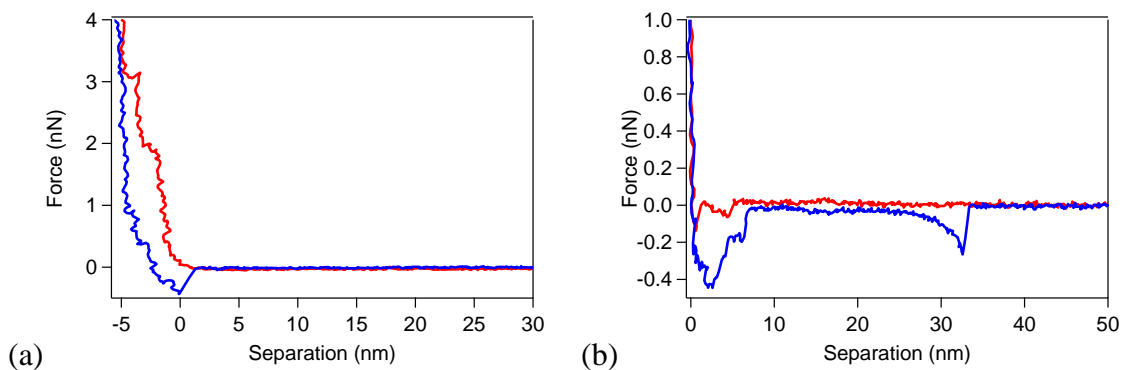


Figure 5.7. Representative force curves displaying (a) MHA coated probe interacting with a suspended CNT sample and (b) 3'-poly(dT₁₀₀) stretching on an APTES surface treated with SDS. Red curve is extension and blue curve is retraction.

Figure 5.8 shows example force curves of 5'-poly(dG₁₀₀) and 5'-poly(dT₁₀₀) on suspended CNTs and Table 5.1 reports the average peeling forces for all four homopolymer bases on suspended CNTs. On graphite, we found that the strength of interaction between the homopolymer oligomers and graphite ranked $T \geq A > G \approx C$. We can see that the peeling forces have a slightly different ranking and lower values than the peeling forces on graphite reported in Chapter 4. Overall, the magnitude of the peeling forces on suspended tubes is not surprising when compared to those on graphite – the surface of the CNT is likely still a frictionless interface where the tube may easily slide and reorient. If there are no strong intrastrand interactions present within the oligomer or if the DNA does not have a wrapped configuration (Figure 5.2), we should expect peeling forces comparable to those on graphite. Thus, peeling on suspended CNTs may serve as a more valuable tool to probe the important secondary structures found in ‘special’ sequences, where complementarity may be important to providing additional stabilization to DNA-CNT complexes.

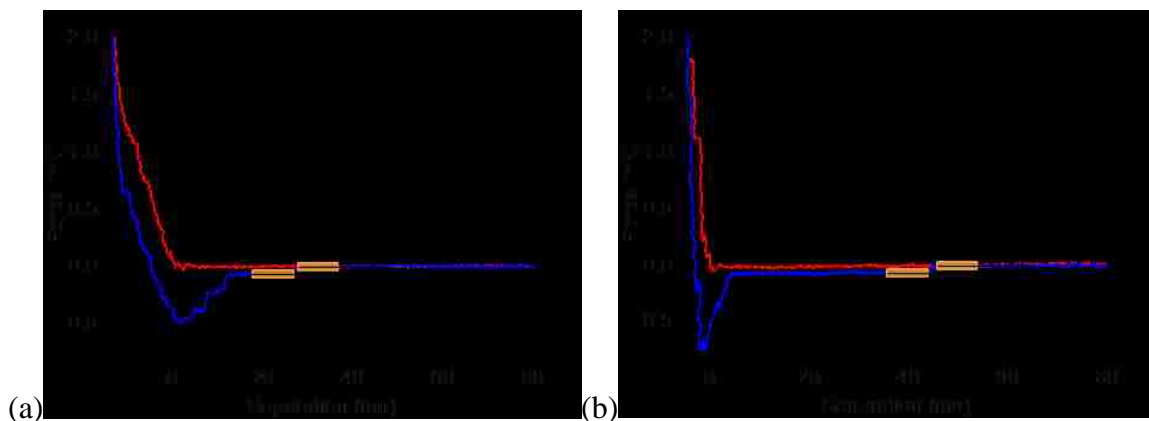


Figure 5.8. Example force curves of (a) 5'-poly(G₁₀₀) and (b) 5'-poly(dT₁₀₀) peeling on suspended CNTs. Extension curves display variability due to interactions with swinging CNTs. Red curve is extension and blue curve is retraction.

On suspended CNTs, we are now able to differentiate between poly(dC) and poly(dG). However, within error, poly(dA), poly(dT), and poly(dG) are almost indistinguishable. The magnitude of the peeling forces of all of the bases on CNTs decreased by 10-40% when compared to graphite. Noy and coworkers observed a strong dependence on the interaction force of DNA inside a CNT pore due to the salt concentration (a 35% decrease in pulling work per base with an increase in salt concentration from 0.1 to 1 M NaCl and a pulling work differing by a factor of 2.5 when going from pure water to 1 M NaCl) – it is possible that the difference in interaction strength could be due to the salt present in these experiments.¹⁸⁸ The errors associated with the peeling forces are also slightly larger than those associated with peeling on graphite – this observation could be attributed to a distribution of CNT diameters (*i.e.* small bundles) and simulations also suggest partial desorption of bases⁵⁵ on the surface of the CNT (although it is expected that DNA may achieve a variety of conformations on the surface of the CNT with similar interaction strengths).⁴⁶ Previously, poly(dG) had a wide distribution of peeling forces on graphite due to secondary peeling modes. For

experiments peeling from CNTs, poly(dG) appears to have a single peeling mode suggesting that a preferential conformation may be achieved on the surface of the CNT.

Table 5.1. Summary of mean homopolymer oligomer peeling forces on suspended CNTs. Reported error is the standard deviation.

Sequence	Peeling force (pN)	# Experiments	# Force Curves
<i>Pyrimidines</i>			
3'-poly(dT₅₀)	63.9 ± 10.7	1	68
5'-poly(dT₁₀₀)	62.8 ± 5.3	1	23
3'-poly(dC₅₀)	36.8 ± 7.1	1	44
<i>Purines</i>			
3'-poly(dA₅₀)	67.8 ± 10.5	1	33
5'-poly(dG₁₀₀)	62.2 ± 16.5	3	100

Molecular dynamics simulations suggest that the DNA wrapping process reaches an equilibrium state in a picosecond timeframe,^{45, 46, 55} suggesting that the DNA should reach its preferred conformation during the short time (milliseconds) in contact during acquisition of force curves. To investigate the effect of time for DNA to reach an equilibrium configuration, experiments were carried out where the probe was allowed to dwell at the substrate surface for 1 second to allow additional time for the DNA to wrap around the CNT surface. Force curves for 3'-poly(dT₅₀) with a dwell time of 1 second had a peeling force of 64.5 ± 5.9 pN, showing good agreement with standard (*i.e.* no dwell) peeling experiments for 3'-poly(dT₅₀). We also find that the length and direction of attachment of the oligomers to the probe has no effect on the peeling forces in the case of poly(dT), similar to our previous results on graphite.

The peeling forces displayed in Table 5.1 are a result of DNA-CNT interactions or wrapping and show different forces when compared to peeling forces measured on the

flat areas in between the photolithographic trenches. Force curves measured on the flat areas still can display stable regions of peeling, which is not surprising since the presence of CNTs on the surface provide a hydrophobic interface. In Chapter 4, we have shown that poly(dT) still shows strong peeling forces on hydrophobic monolayers. Force curves for 5'-poly(dG₁₀₀) measured on flat areas displayed an average peeling force of 42.8 ± 12.0 pN – approximately 25% smaller than the peeling forces for 5'-poly(dG₁₀₀) over trench areas. This difference in peeling forces suggests that poly(dG) can achieve a mode of interaction not achievable on the flat surface. If we consider the peeling forces of 5'-poly(dG₁₀₀) on the flat areas, we observe the same ranking of peeling forces as graphite (*i.e.* poly(dG) \approx poly(dC)). For 3'-poly(dT₅₀), where it is assumed that secondary structure is not important to the DNA-CNT interactions, we observed similar peeling forces on the flat areas (66.0 ± 6.1 pN).

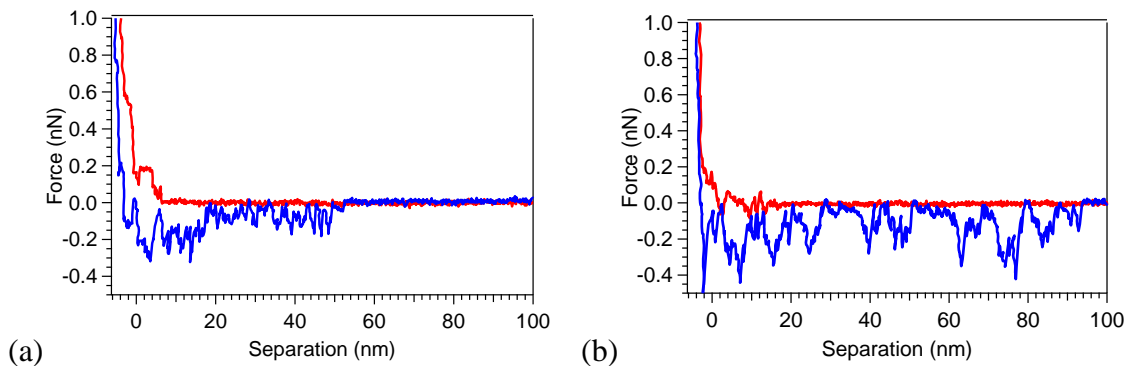


Figure 5.9. Examples of complex, periodic features during retraction in force curves for 5'-poly(dTdTdT)₂₀. Red curve is extension and blue curve is retraction.

Finally, interesting features were observed for oligomers where strong intrastrand interactions are possible - sequences such as poly(dG) and poly(dTdTdT). Figure 5.9 displays examples of force curves with periodic stretching features during retraction from

the surface. 5'-poly(dTAdTdT)₂₀ reproducibly shows highly periodic stretching peaks over trench areas – likely due to its ability to create stable hydrogen bonding between bases. In some cases, poly(dTAdTdT) still produces stable peeling plateaus (68 pN) equivalent to peeling forces of poly(dT) or poly(dA). Stretching features like those in Figure 5.9 were not observed for poly(dTAdTdT) on graphite where stable peeling similar to poly(dT) and poly(dA) occurred (Figure 5.10), suggesting that these experiments offer 3-dimensional configurations that are not accessible on planar substrates. Suresh Manohar previously studied the peeling forces of 5'-poly(dTAdTdT)₂₀ on graphite and determined an average peeling force of 81.7 ± 4.6 pN (in close agreement with peeling forces for poly(dT) and poly(dA), see Chapter 4) on graphite from 2 experiments with 750 force curves. Suresh observed an initial adhesion peak that was typically over 5 nN, which is possibly due strong interactions due to β -sheet motif structures created by base stacking.

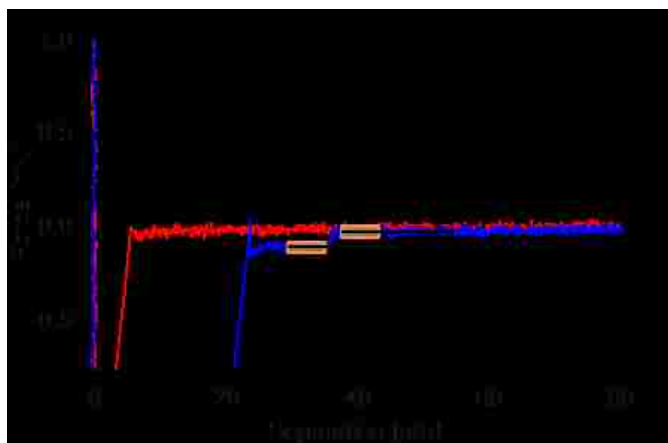


Figure 5.10. Typical force curve for 5'-poly(dTAdTdT)₂₀ peeling on graphite. The large adhesion peak was excluded to show details of the peeling plateau. Red curve is extension and blue curve is retraction. Force curve was recorded by Suresh Manohar.

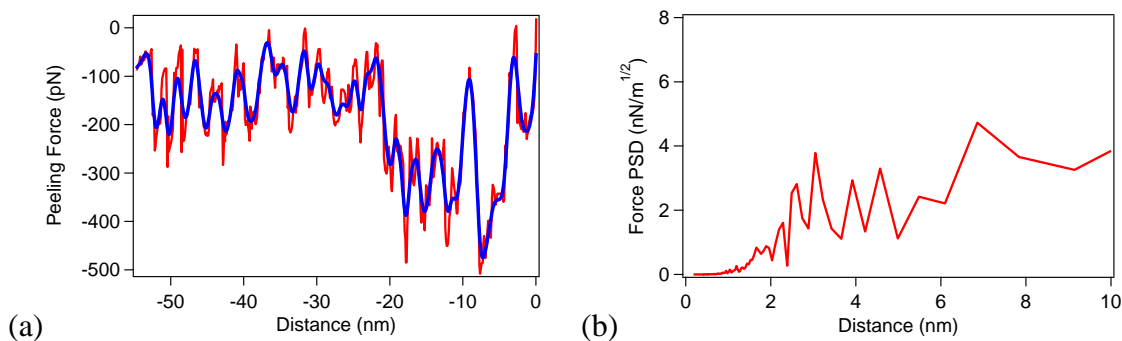


Figure 5.11. (a) Isolated force *versus* distance data from the retraction region of force distance curve displayed in Figure 5.9a. Blue line is a smoothed curve to eliminate noise for FFT analysis. (b) Magnitude power spectrum density (PSD) of the stretching forces displays several peeling modes.

If poly(dTdAdTdT) is indeed helically wrapping around the outside of the CNT, considering the contour length and CNT diameter, it should be possible to create up to 18 wraps around the outside of the CNT. It would be interesting to measure the frequency of the stretching peaks in order to correlate the stretching forces with the breaking of a specific interaction within the strand. The retraction curve from Figure 5.9a was analyzed with a fast Fourier transform (FFT) to find common stretching distances. Figure 5.11 displays the FFT results for the force curve displayed in Figure 5.9a. In many cases, it is difficult to identify clear stretching modes due to the presence of noise and the general irregularity of the peaks, which may be reduced with smoothing. Figure 5.11b shows clear groupings in the stretching distances. Interestingly, the shorter stretching modes are in the range of 2.25-4.5 nm, which is close to the perimeter of a (6,5) CNT (diameter is 0.8 nm, perimeter 2.51 nm). It is possible that the stretching is created by breaking of dT-dA base pairs as the chain is unwrapped from the CNT. However, the observed stretching peaks are typically in the range of 50-400 pN, much stronger than the unzipping force for a dT-dA base pair (9 pN),^{200, 201} but are fairly comparable to non-equilibrium melting

transitions (150-250 pN).^{200, 202} The overall magnitude of these interactions could be a result of breaking Watson-Crick base pairs coupled with strong DNA-CNT interactions which may greatly stabilize the complex. Future experiments to examine this interesting observation are required to further prove that these interactions are caused by unzipping or removal 3-dimensional β -barrel structures created by ‘special’ sequences. Experiments utilizing varied force rates and a stiffer cantilever with less noise may elucidate more clear interactions of the DNA removal from the CNT.

5.4 Conclusions

We have completed peeling experiments for homopolymer oligomers on suspended CNTs produced by a simple self-assembly technique. The peeling forces of homopolymer oligomers on suspended CNTs were lower than those measured on graphite. However, periodic stretching features were observed for oligomers when strong intrastrand interactions were present. If oligomers do not have strong intrastrand interactions, the interaction force on graphite is a good measure of the interaction strength on CNTs. Preliminary results suggest that this procedure will provide more interesting information on the propensity of ‘special’ sequences to interact with specific tube chiralities (which may easily be substituted with the above preparation procedure).

Further experiments should investigate other special sequences as well as experiments where the salt concentration is modified. While we did not observe a dependence of the peeling forces of oligomers on graphite with salt concentration, this is in contradiction to the work from Noy and coworkers where they observed a strong effect due to the salt concentration for experiments pulling DNA from a CNT pore. It is

possible that the salt concentration could be the cause for the reduced peeling forces compared to graphite.

5.5 Appendix

5.5.1 Measurement of Slack in Suspended CNTs

Minot *et al.* have previously completed strain experiments on suspended CNTs with load applied to the center of the CNT by an AFM probe.⁴⁰ The method to prepare suspended CNTs required etching the substrate from underneath pinned CNTs lying flat on the substrate surface. Even though the tubes were flat on the substrate before etching, they still claimed that the suspended CNTs had slack due to longitudinal deformation. Minot *et al.* measured CNTs with 10-20 nm of slack. This slack was displayed by stretching features during retraction of force curves. In our experiments, we do not have an experimental setup where high attraction between the CNT and probe exist, but we were still able to observe stretching (likely due to tubes) with an MHA functionalized AFM probe (Figure 5.12).

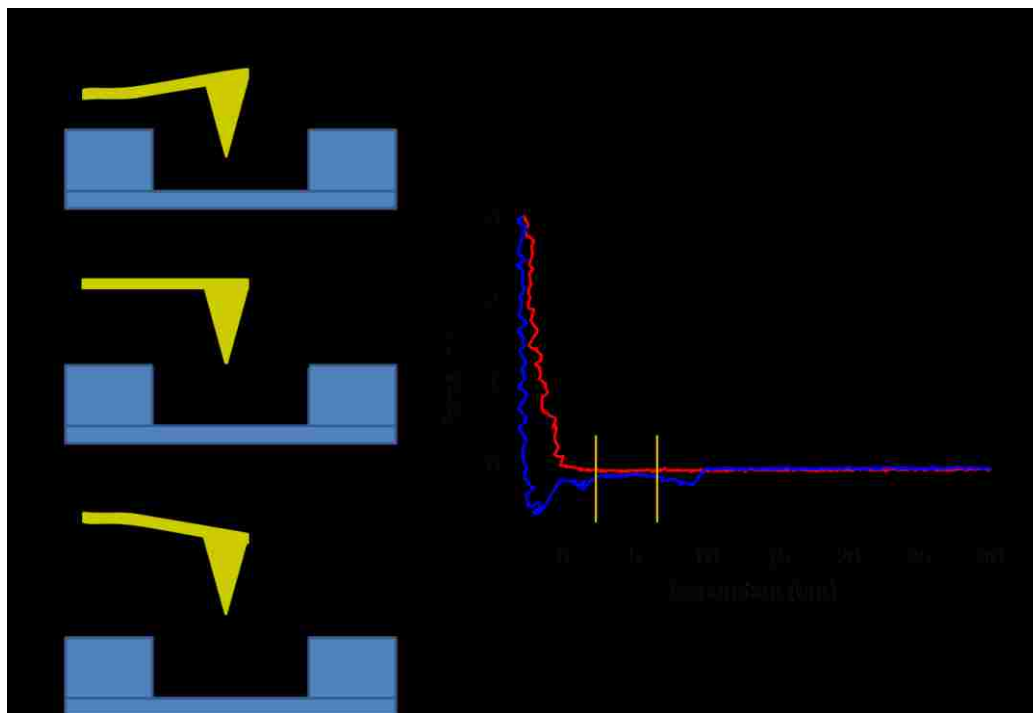


Figure 5.12. An example of a force curve displaying stretching features during retraction with visualization of the associated AFM cantilever response and CNT bending. The stretching peak is due to taking up of slack within the suspended CNT and eventual removal. The red curve is extension and the blue curve is retraction. Cartoon is not drawn to scale.

References

1. Noy, A., *Handbook of Molecular Force Spectroscopy*. Springer: 2008.
2. Butt, H. J.; Cappella, B.; Kappl, M., *Surf. Sci. Rep.* **2005**, *59* (1-6), 1-152.
3. Dimitriadis, E. K.; Horkay, F.; Maresca, J., *et al.*, *Biophys. J.* **2002**, *82*, 2798-2810.
4. Houston, J. E.; Doelling, C. M.; Vanderlick, T. K., *et al.*, *Langmuir* **2005**, *21* (9), 3926-3932.
5. Vezenov, D. V.; Noy, A.; Lieber, C. M., *J. Adhes. Sci. Technol.* **2003**, *17* (10), 1385-1401.
6. Noy, A.; Vezenov, D.; Lieber, C. M., *Annu. Rev. Mater. Sci.* **1997**, *27*, 381-421.
7. Barrena, E.; Kopta, S.; Ogletree, D. F., *et al.*, *Phys. Rev. Lett.* **1999**, *82* (14), 2880-2883.
8. Carpick, R. W.; Ogletree, D. F.; Salmeron, M., *Appl. Phys. Lett.* **1997**, *70* (12), 1548-1550.
9. Fuierer, R., *Asylum Research Procedural Operation Manulette*. 2009.
10. Sader, J. E.; Chon, J. W. M.; Mulvaney, P., *Rev. Sci. Instrum.* **1999**, *70* (10), 3967-3969.
11. Poggi, M. A.; Mcfarland, A. W.; Colton, J. S., *et al.*, *Anal. Chem.* **2006**, *77* (4), 1192-1195.
12. Cleveland, J. P.; Manne, S.; Bocek, D., *et al.*, *Rev. Sci. Instrum.* **1993**, *64* (2), 403-405.
13. Hutter, J. L.; Bechhoefer, J., *Review of Scientific Instruments* **1993**, *64* (7), 1868
14. Munz, M., *Journal of Physics D-Applied Physics* **2010**, *43* (6).
15. Palacio, M. L. B.; Bhushan, B., *CRC CR REV SOL STATE* **2010**, *35*, 73-104.
16. Bell, G. I., *Science* **1978**, *200* (4342), 618-627.
17. Evans, E.; Ritchie, K., *Biophys. J.* **1997**, *72*, 1541-1555.
18. Hanke, F.; Kreuzer, H. J., *Biointerphases* **2006**, *1* (1), 11-17.
19. Schmidt, S. Dynamic Force Spectroscopy of the Silicon-Carbon Bond. University of Applied Sciences, Munich, 2008.
20. Fernandez, J. M.; Li, H., *Science* **2004**, *303*, 1674-1678.

21. Schlierf, M.; Li, H.; Fernandez, J. M., *Proc Natl Acad Sci U S A* **2004**, *101* (19), 7299-7304.
22. Strunz, T.; Oroszlan, K.; Schafer, R., *et al.*, *Proc Natl Acad Sci U S A* **1999**, *96*, 11277-11282.
23. Beyer, M.; Clausen-Schaumann, H., *Chem. Rev.* **2005**, *105* (8), 2921-2948.
24. Manohar, S.; Jagota, A., *Physical Review E* **2010**, *81*.
25. Manohar, S.; Mantz, A. R.; Bancroft, K. E., *et al.*, *Nano Lett.* **2008**, *8* (12), 4365-4372.
26. Iliafar, S.; Vezenov, D.; Jagota, A., *Langmuir* **2013**, *29*, 1435-1445.
27. Ruan, J. A.; Bhushan, B., *Journal of Tribology-Transactions of the Asme* **1994**, *116* (2), 378-388.
28. Wang, M., *Journal of the Mechanics and Physics of Solids* **2004**, *52* (10), 2329-2354.
29. Johnson, K. L.; Kendall, K.; Roberts, A. D., *D. Proc. R. Soc. London A* **1971**, *324*.
30. Derjaguin, B. V.; Muller, V. M.; Toporov, Y. P., *J. Colloid Interface Sci.* **1975**, *53*.
31. Grierson, D. S.; Flater, E. E.; Carpick, R. W., *J. Adhesion Sci. Technol.* **2005**, *19* (3-5), 291-311.
32. Carpick, R. W.; Ogletree, D. F.; Salmeron, M., *J. Colloid Interface Sci.* **1999**, *211* (2), 395-400.
33. Reedy, E. D., *J. Mater. Res.* **2011**, *21* (10), 2660-2668.
34. Maugis, D., *Journal of Colloid Interface Science* **1992**, *150* (1), 243-269.
35. Iijima, S., *Nature* **1991**, *354*, 56-58.
36. Dresselhaus, M. S.; Dresselhaus, G.; Avouris, P., *Carbon nanotubes: Synthesis, structure, properties, and applications*. Springer: New York, 2010.
37. Belin, T.; Epron, F., *Mater. Sci. Eng., B* **2005**, *119*, 105-118.
38. Hodge, S. A.; Bayazit, M. K.; Coleman, K. S., *et al.*, *Chem. Soc. Rev.* **2012**, *41* (12), 4409-4429.
39. Hertel, T.; Martel, R.; Avouris, P., *J. Phys. Chem. B* **1998**, *102* (6), 910-915.
40. Minot, E.; Yaish, Y.; Sazonova, V., *et al.*, *Phys. Rev. Lett.* **2003**, *90* (15).

41. Kuzumaki, T.; Mitsuda, Y., *Appl. Phys. Lett.* **2004**, 85 (7), 1250-1252.
42. Zheng, M.; Jagota, A.; Strano, M. S., *et al.*, *Science* **2003**, 302, 1545-1548.
43. Zheng, M.; Jagota, A.; Semke, E. D., *et al.*, *Nature Materials* **2003**, 2 (5), 338-342.
44. Tu, X.; Manohar, S.; Jagota, A., *et al.*, *Nature* **2009**, 460 (7252), 250-253.
45. Roxbury, D.; Manohar, S.; Jagota, A., *journal of physical chemistry C* **2010**, 114, 13267-13276.
46. Roxbury, D.; Mittal, J.; Jagota, A., *Nano Lett.* **2012**, 12 (3), 1464-9.
47. Forrest, S. R., *Nature* **2004**, 428 (6986), 911-918.
48. Ng, S. C.; Zhou, X. C.; Chen, Z. K., *et al.*, *Langmuir* **1998**, 14 (7), 1748-1752.
49. Rella, R.; Siciliano, P.; Valli, L., *et al.*, *Sensors and Actuators B-Chemical* **1998**, 48 (1-3), 328-332.
50. Mccullough, D. H.; Grygorash, R.; Hsu, J. T., *et al.*, *J. Am. Chem. Soc.* **2007**, 129 (27), 8663-8667.
51. Blodgett, K. J., *J. Am. Chem. Soc.* **1934**, 65, 495.
52. Mccullough, D. H.; Janout, V.; Li, J. W., *et al.*, *J. Am. Chem. Soc.* **2004**, 126 (32), 9916-9917.
53. Heller, D. A.; Jeng, E. S.; Yeung, T. K., *et al.*, *Science* **2006**, 311 (5760), 508-511.
54. Feazell, R. P.; Nakayama-Ratchford, N.; Dai, H., *et al.*, *J. Am. Chem. Soc.* **2007**, 129 (27), 8438-8439.
55. Manohar, S.; Tang, T.; Jagota, A., *Journal of Physical Chemistry C* **2007**, 111 (48), 17835-17845.
56. Vezenov, D. V.; Noy, A.; Ashby, P., *J. Adhesion Sci. Technol.* **2005**, 19 (3-5), 313-364.
57. Lee, C.; Li, Q.; Kalb, W., *et al.*, *Science* **2010**, 328, 76-80.
58. Gao, G. T.; Cannara, R. J.; Carpick, R. W., *et al.*, *Langmuir* **2007**, 23 (10), 5394-5405.
59. Van Der Vegte, E. W.; Subbotin, A.; Hadziioannou, G., *et al.*, *Langmuir* **2000**, 16 (7), 3249-3256.

60. Xiao, X. D.; Hu, J.; Charych, D. H., *et al.*, *Langmuir* **1996**, *12* (2), 235-237.
61. Bhushan, B.; Sundararajan, S., *Acta Mater* **1998**, *46* (11), 3793-3804.
62. Asay, D. B.; Dugger, M. T.; Ohlhausen, J. A., *et al.*, *Langmuir* **2008**, *24* (1), 155-159.
63. Hsiao, E.; Kim, D.; Kim, S. H., *Langmuir* **2009**, *25* (17), 9814-9823.
64. Liu, H. W.; Bhushan, B., *Ultramicroscopy* **2003**, *97* (1-4), 321-340.
65. Walters, D. A.; Cleveland, J. P.; Thomson, N. H., *et al.*, *Rev. Sci. Instrum.* **1996**, *67* (10), 3583-3590.
66. Lantz, M. A.; O'shea, S. J.; Hoole, A. C. F., *et al.*, *Appl. Phys. Lett.* **1997**, *70* (8), 970-972.
67. Ogletree, D. F.; Carpick, R. W.; Salmeron, M., *Rev. Sci. Instrum.* **1996**, *67* (9), 3298-3306.
68. Varenberg, M.; Etsion, I.; Halperin, G., *Rev. Sci. Instrum.* **2003**, *74* (7), 3362-3367.
69. Walters, D. A.; Cleveland, J. P.; Thomson, N. H., *et al.*, *Rev. Sci. Instrum.* **1996**, *67* (10), 3583-3590.
70. Butt, H. J.; Jaschke, M., *Nanotechnology* **1995**, *6*, 1-7.
71. Van Eysden, C. A.; Sader, J. E., *J. Appl. Phys.* **2007**, *101* (4).
72. Higgins, M. J.; Proksch, R.; Sader, J. E., *et al.*, *Rev. Sci. Instrum.* **2006**, *77* (1), 013701.
73. Attard, P.; Pettersson, T. R.; Rutland, M. W., *Rev. Sci. Instrum.* **2006**, *77* (11), 116110.
74. Green, C. P.; Lioe, H.; Cleveland, J. P., *et al.*, *Rev. Sci. Instrum.* **2004**, *75* (6), 1988-1996.
75. Proksch, R.; Schaffer, T. E.; Cleveland, J. P., *et al.*, *Nanotechnology* **2004**, *15* (9), 1344-1350.
76. Pirzer, T.; Hugel, T., *Rev. Sci. Instrum.* **2009**, *80* (3), 035110.
77. Naeem, S.; Liu, Y.; Nie, H. Y., *et al.*, *J. Appl. Phys.* **2008**, *104* (11).
78. Song, Y.; Bhushan, B., Modeling of Tip-Cantilever Dynamics in Atomic Force Microscopy. In *Applied Scanning Probe Methods V*, Bhushan, B.; Kawata, S.; Fuchs, H., Eds. Springer: Berlin, 2007; pp 149-223.

79. Kiracofe, D.; Raman, A., *J. Appl. Phys.* **2010**, *107* (3), 033506.
80. Maali, A.; Hurth, C.; Boisgard, R., *et al.*, *J. Appl. Phys.* **2005**, *97* (7), 074907.
81. Bellon, L., *J. Appl. Phys.* **2008**, *104* (10), 104906.
82. Kennedy, S. J.; Cole, D. G.; Clark, R. L., *Rev. Sci. Instrum.* **2009**, *80* (12), 125103.
83. Cole, D. G., *Meas. Sci. Technol.* **2008**, *19* (12), 125101.
84. Burnham, N. A.; Chen, X.; Hodges, C. S., *et al.*, *Nanotechnology* **2003**, *14* (1), 1-6.
85. Cook, S. M.; Schaffer, T. E.; Chynoweth, K. M., *et al.*, *Nanotechnology* **2006**, *17*, 2135-2145.
86. Poggi, M. A.; Mcfarland, A. W.; Colton, J. S., *et al.*, *Anal. Chem.* **2006**, *77* (4), 1192-1195.
87. Hazel, J. L.; Tsukruk, V. V., *Thin Solid Films* **1999**, *339* (1-2), 249-257.
88. Maali, A.; Hurth, C.; Boisgard, R., *et al.*, *J. Appl. Phys.* **2005**, *97* (7).
89. Tocha, E.; Schonherr, H.; Vancso, G. J., *Langmuir* **2006**, *22*, 2340-2350.
90. Tocha, E.; Song, J.; Schonherr, H., *et al.*, *Langmuir* **2007**, *23* (13), 7078-7082.
91. Lee, H. S.; Kim, D. S.; Park, J. W., *et al.*, *Thin Solid Films* **2006**, *499* (1-2), 402-405.
92. Osterbacka, R.; Pal, A. J.; Stubb, H., *Thin Solid Films* **1998**, *329*, 668-670.
93. Mccullough, D. H.; Grygorash, R.; Regen, S. L., *Langmuir* **2007**, *23* (19), 9606-9610.
94. He, X. Z.; Zhou, Y. L.; Wang, L. X., *et al.*, *Dyes and Pigments* **1998**, *39* (4), 231-241.
95. Higo, T.; Ikehara, T.; Irokawa, K., *et al.*, *Japanese Journal of Applied Physics Part 1-Regular Papers Brief Communications & Review Papers* **2005**, *44* (7B), 5871-5874.
96. Blodgett, K. J. *Film Structure and Method of Preparation.* 1940.
97. Yan, X.; Janout, V.; Hsu, J. T., *et al.*, *J. Am. Chem. Soc.* **2003**, *125* (27), 8094-8095.
98. Mccullough, D. H.; Regen, S. L., *Chem. Commun.* **2004**, (24), 2787-2791.

99. Wang, Y.; Janout, V.; Regen, S. L., *Macromolecules* **2008**, *41* (3), 497-500.
100. Garcia-Manyes, S.; Domenech, O.; Sanz, F., *et al.*, *Biochimica Et Biophysica Acta-Biomembranes* **2007**, *1768* (5), 1190-1198.
101. Bhushan, B.; Kulkarni, A. V.; Koinkar, V. N., *et al.*, *Langmuir* **1995**, *11* (8), 3189-3198.
102. Oncins, G.; Torrent-Burgues, J.; Sanz, F., *Tribology Letters* **2006**, *21* (3), 175-184.
103. Lee, K. M.; Polycarpou, A. A., *J. Mater. Res.* **2006**, *21* (9), 2304-2313.
104. Schneider, J.; Dori, Y.; Tirrell, M., *et al.*, *Thin Solid Films* **1998**, *329*, 772-777.
105. Tsarkova, L. A.; Protsenko, P. V.; Klein, J., *Colloid J.* **2004**, *66* (1), 84-94.
106. He, G.; Muser, M. H.; Robbins, M. O., *Science* **1999**, *284* (5420), 1650-1652.
107. Gerde, E.; Marder, M., *Nature* **2001**, *413* (6853), 285-288.
108. Lorenz, C. D.; Webb, E. B.; Stevens, M. J., *et al.*, *Tribology Letters* **2005**, *19* (2), 93-99.
109. Chandross, M.; Lorenz, C. D.; Stevens, M. J., *et al.*, *Langmuir* **2008**, *24* (4), 1240-1246.
110. Nosonovsky, M.; Bhushan, B., *Materials Science & Engineering R-Reports* **2007**, *58* (3-5), 162-193.
111. Wang, L. Y.; Yin, Z. F.; Zhang, J., *et al.*, *Wear* **2000**, *237*, 155-162.
112. Ariga, K.; Mori, T.; Hill, J. P., *Soft Matter* **2012**, *8*, 15-20.
113. Ariga, K.; Mori, T.; Hill, J. P., *Adv. Mater.* **2012**, *24*, 158-176.
114. Ariga, K.; Ito, H.; Hill, J. P., *et al.*, *Chem. Soc. Rev.* **2012**, *41* (17), 5800-5835.
115. Li, J. W.; Janout, V.; Regen, S. L., *Langmuir* **2006**, *22* (26), 11224-11229.
116. Tocha, E.; Schonherr, H.; Vancso, G. J., *Langmuir* **2006**, *22* (5), 2340-2350.
117. Flater, E. E.; Ashurst, W. R.; Carpick, R. W., *Langmuir* **2007**, *23* (18), 9242-9252.
118. Noy, A.; Vezenov, D. V.; Lieber, C. M., *Annu. Rev. Mater. Sci.* **1997**, *27*, 381-421.

119. Subhalakshmi, K.; Devaprakasam, D.; Math, S., *et al.*, *Tribology Letters* **2008**, *31* (1), 1-11.
120. Kopta, S.; Salmeron, M., *J. Chem. Phys.* **2000**, *113* (18), 8249-8252.
121. Kim, H. I.; Boiadjev, V.; Houston, J. E., *et al.*, *Tribology Letters* **2001**, *10* (1-2), 97-101.
122. Chandross, M.; Grest, G. S.; Stevens, M. J., *Langmuir* **2002**, *18* (22), 8392-8399.
123. Dinelli, F.; Leggett, G. J.; Shipway, P. H., *Nanotechnology* **2005**, *16* (6), 675-682.
124. Lio, A.; Charych, D. H.; Salmeron, M., *J. Phys. Chem. B* **1997**, *101* (19), 3800-3805.
125. Sotres, J.; Barrantes, A.; Arnebrant, T., *Langmuir* **2011**, *27* (15), 9439-9448.
126. Greenwood, J. A., *Proceedings of the Royal Society of London Series a-Mathematical Physical and Engineering Sciences* **1997**, *453* (1961), 1277-1297.
127. Radmacher, M.; Fritz, M.; Cleveland, J. P., *et al.*, *Langmuir* **1994**, *10* (10), 3809-3814.
128. Flores, A.; Balta Calleja, F. J.; Attenburrow, G. E., *et al.*, *Polymer* **2000**, *41*, 5431-5435.
129. Sotres, J.; Lindh, L.; Arnebrant, T., *Langmuir* **2011**, *27* (22), 13692-13700.
130. Struik, L. C. E., *J. Non-Cryst. Solids* **1991**, *131*, 395-407.
131. Mark, J. E., *Polymer Data Handbook*. Oxford University Press, Inc.: 1999.
132. Lio, A.; Morant, C.; Ogletree, D. F., *et al.*, *J. Phys. Chem. B* **1997**, *101* (24), 4767-4773.
133. Zheng, M.; Jagota, A.; Semke, E. D., *et al.*, *Nature Materials* **2003**, *2* (5), 338-342.
134. Zheng, M. J., A.; Strano, M. S.; Santos, A. P.; Barone, P.; Grace Chou, S.; Diner, B. A.; Dresselhaus, M. S.; Mclean, R. S.; Onoa, G. B.; Samsonidze, G. G.; Semke, E. D.; Usrey, M.; Walls, D. J., *Science* **2003**, *302* (5650), 1545-1548
135. Tu, X.; Manohar, S.; Jagota, A., *et al.*, *Nature* **2009**, *460*, 250-253.
136. Feazell, R. P.; Nakayama-Ratchford, N.; Dai, H., *et al.*, *Journal of the American Chemical Society* **2007**, *129* (27), 8438-8439.
137. Kam, N. W. S.; Dai, H., *Journal of the American Chemical Society* **2005**, *127* (16), 6021-6026.

138. Kam, N. W. S.; Jessop, T. C.; Wender, P. A., *et al.*, *Journal of the American Chemical Society* **2004**, *126* (22), 6850-6851.
139. Heller, D. A.; Jeng, E. S.; Yeung, T. K., *et al.*, *Science* **2006**, *311* (5760), 508-511.
140. Meng, S.; Maragakis, P.; Papaloukas, C., *et al.*, *Nano Letters* **2007**, *7* (1), 45-50.
141. Bianco, A.; Prato, M., *Advanced Materials; WILEY-VCH Verlag* **2003**, *15* (20), 1765-1768.
142. Kam, N. W. S.; Liu, Z.; Dai, H., *Journal of the American Chemical Society* **2005**, *127* (36), 12492-12493
143. Kam, N. W. S.; M., O. C.; A., W. J., *et al.*, *PNAS* **2005**, *102* (33), 11600-11605.
144. Liu, Z.; Li, X.; Tabakman, S. M., *et al.*, *Journal of the American Chemical Society* **2008**, *130* (41), 13540-13541
145. Liu, Z.; Winters, M.; Holodniy, M., *et al.*, *Angew Chem Inter* **2007**, *Ed 46*, 2023–2027.
146. Prato, M.; Kostarelos, K.; Bianco, A., *Accounts of Chemical Research* **2008**, *41* (1), 60-68.
147. Noy, A., *Handbook of Molecular Force Spectroscopy*. Springer: New York, 2008.
148. Noy, A.; Vezenov, D. V.; Kayyem, J. F., *et al.*, *Chemistry & Biology* **1997**, *4* (7), 519-527.
149. Krautbauer, R.; Rief, M.; Gaub, H. E., *Nano Letters* **2003**, *3* (4), 493-496
150. Ozkaya, B.; Ozcan, O.; Thissen, P., *et al.*, *Langmuir* **2010** *26* (11), 8155-8160.
151. Sonnenberg, L.; Billon, L.; Gaub, H. E., *Macromolecules* **2008**, *41* (10), 3688-3691
152. Scherer, A.; Zhou, C.; Michaelis, J., *et al.*, *Macromolecules* **2005**, *38* (23), 9821-9825
153. Roxbury, D.; Tu, X.; Zheng, M., *et al.*, *Langmuir* **2011**, *27* (13), 8282-8293.
154. Manohar, S.; Mantz, A. R.; Bancroft, K. E., *et al.*, *Nano Letters* **2008**, *8* (12), 4365-4372.
155. Manohar, S.; Tang, T.; Jagota, A., *Journal of Physical Chemistry C* **2007**, *111* (48), 17835-17845.

156. Ikeda, A.; Hamano, T.; Hayashi, K., *et al.*, *Organic Letters* **2006**, 8 (6), 1153-1156.
157. Sowerby, S. J.; Cohn, C. A.; Heckl, W. M., *et al.*, *Proceedings of the National Academy of Sciences of the United States of America* **2001**, 98 (3), 820-822.
158. Sowerby, S. J.; Morth, C. M.; Holm, N. G., *Astrobiology* **2001**, 1 (4), 481-487.
159. Saenger, W., *Springer-Verlag* **1984**, ISBN 0387907610
160. Varghese, N.; Mogera, U.; Govindaraj, A., *et al.*, *Chemphyschem : a European journal of chemical physics and physical chemistry* **2009**, 10 (1), 206-10.
161. Szilagyi, A.; Bonn, G. K.; Guttman, A., *Journal of Chromatography, A* **2007**, 1161 (1-2), 15-21.
162. Teflon AF Amorphous Fluoropolymer. http://www2.dupont.com/Teflon_Industrial/en_US/assets/downloads/h44015.pdf.
163. Kühner, F.; Erdmann, M.; Sonnenberg, L., *et al.*, *Langmuir* **2006**, 22 (26), 11180-11186.
164. Manohar, S.; Mantz, A. R.; Bancroft, K. E., *et al.*, *Nano Lett.* **2008**, 8 (12), 4365-4372.
165. Iliafar, S.; Wagner, K.; Manohar, S., *et al.*, *The Journal of Physical Chemistry C* **2012**, 116 (26), 13896-13903.
166. Keten, S.; Buehler, M. J., *Phys. Rev. Lett.* **2008**, 100, 198301.
167. Harris, D. C., *Quantitative Chemical Analysis*. Sixth Edition ed.; New York, 2002.
168. Dill, K. A.; Bromberg, S., *Molecular Driving Forces: Statistical Thermodynamics in Chemistry and Biology*. New York, 2003.
169. Li, I. T. S.; Walker, G. C., *PNAS* **2011**, 108 (40), 16527-16532.
170. Wagner, K.; Cheng, P.; Vezenov, D. V., *Langmuir* **2011**, 27 (8), 4635-4644
171. Kennedy, S. J.; Cole, D. G.; Clark, R. L., *Review of Scientific Instruments* **2009**, 80 (12), 125103.
172. Packer, M. J.; Hunter, C. A., *Journal of Molecular Biology* **1998**, 280 (3), 407-420.
173. Roxbury, D.; Mittal, J.; Jagota, A., *Nano Lett.* **2012**, 12 (3), 1464-1469.

174. Roxbury, D.; Manohar, S.; Jagota, A., *The Journal of Physical Chemistry C* **2010**, *114* (31), 13267-13276.
175. Fu, Y.; Carlberg, B.; Lindahl, N., *et al.*, *Adv. Mater.* **2012**, *24* (12), 1576-81.
176. Hong, B. H.; Lee, J. Y.; Beetz, T., *et al.*, *J. Am. Chem. Soc.* **2005**, *127*, 15336-15337.
177. Kong, J.; Soh, H. T.; Cassell, A. M., *et al.*, *Nature* **1998**, *395* (878-881).
178. Marcus, M. S.; Simmons, J. M.; Baker, S. E., *et al.*, *Nano Lett.* **2009**, *9* (5), 1806-1811.
179. Jung, Y. J.; Homma, Y.; Ogino, T., *et al.*, *J. Phys. Chem. B* **2003**, *107*, 6859-6864.
180. Khripin, C. Y.; Zheng, M.; Jagota, A., *J. Colloid Interface Sci.* **2009**, *330* (2), 255-265.
181. Shimonda, H.; Oh, S. J.; Geng, Z., *et al.*, *Adv. Mater.* **2002**, *14* (12), 899-901.
182. Tsukruk, V.; Ko, H.; Peleshanko, S., *Phys. Rev. Lett.* **2004**, *92* (6).
183. Liu, J.; Rinzler, A.; Dai, H., *et al.*, *Science* **1998**, *280* (5367), 1253-1256.
184. Chen, Z.; Yang, Y.; Wu, Z., *et al.*, *J. Phys. Chem. B* **2005**, *109*, 5473-5477.
185. Choi, K. H.; Bourgoin, J. P.; Auvray, S., *et al.*, *Surf. Sci.* **2000**, *462*, 195-202.
186. Druzhinina, T.; Hoepfener, S.; Schubert, U. S., *Adv. Mater.* **2011**, *23* (8), 953-70.
187. Ma, Y.; Wang, B.; Wu, Y., *et al.*, *Carbon* **2011**, *49* (13), 4098-4110.
188. Lulevich, V.; Kim, S.; Grigoropoulos, C. P., *et al.*, *Nano Lett.* **2011**, *11* (3), 1171-6.
189. Liu, J.; Rinzler, A.; Dai, H., *et al.*, *Science* **1998**, *280*, 1253-1256.
190. Nan, X.; Gu, Z.; Liu, Z., *J. Colloid Interface Sci.* **2002**, *245* (2), 311-8.
191. Kim, H. R.; Park, S.; Jung, C., *et al.*, *Chem. Commun.* **2010**, *46* (35), 6584-6.
192. Ellis, A. V.; Vijayamohanan, K.; Goswami, R., *et al.*, *Nano Lett.* **2003**, *3* (3), 279-282.
193. Wagner, K.; Cheng, P.; Vezenov, D., *Langmuir* **2011**, *27* (8), 4635-4644.
194. Howarter, J.; Youngblood, J., *Langmuir* **2006**, *22* (26), 11142-11147.

195. Liu, Z.; Shen, Z.; Zhu, T., *et al.*, *Langmuir* **2000**, *16* (8), 3569-3573.
196. In, J. B.; Grigoropoulos, C. P.; Chernov, A. A., *et al.*, *Appl. Phys. Lett.* **2011**, *98* (15), 153102.
197. Liao, X. Z.; Serquis, A.; Jia, Q. X., *et al.*, *Appl. Phys. Lett.* **2003**, *82* (16), 2694.
198. Santangelo, S.; Messina, G.; Faggio, G., *et al.*, *The European Physical Journal Applied Physics* **2008**, *44* (2), 171-180.
199. Roxbury, D.; Tu, X.; Zheng, M., *et al.*, *Langmuir* **2011**, *27* (13), 8282-8293.
200. Rief, M.; Claussen-Schaumann, H.; Gaub, H. E., *Nature* **1999**, *6* (4), 346-349.
201. Woodside, M. T.; Behnke-Parks, W. M.; Larizadeh, K., *et al.*, *Proc Natl Acad Sci U S A* **2006**, *103* (16), 6190-5.
202. Cocco, S.; Monasson, R.; Marko, J., *Physical Review E* **2002**, *65* (4).

Curriculum Vitae

KYLE WAGNER

kcw206@gmail.com

5047 Rebecca Fell Dr. Doylestown, PA 18902

Phone: (484) 332-5041

Objective:

Obtain a research or postdoctoral position in the field of surface science, microscopy, nanoparticle synthesis, or microfabrication.

Qualifications:

- Expert in atomic force microscopy – advanced imaging modes and force spectroscopy
- Nanoparticle synthesis, microfabrication, optical and scanning electron microscopy, and carbon nanotube synthesis and processing

Education:

Expected Graduation: **Lehigh University**, Bethlehem, PA

Spring 2013 Ph.D Candidate, Chemistry

Advisor: Dmitri Vezenov

2008 M.S., Chemistry

2006 **Kutztown University**, Kutztown, PA

B.S. in Chemistry, Minor in Mathematics

Technical Skills:

- *Imaging Techniques*: atomic force microscopy and force spectroscopy, scanning electron microscopy, optical microscopy, optical interferometry, microtomy
- *Synthesis*: quantum dots, metal nanoparticles, carbon nanotubes
- *Fabrication*: clean room experience, photolithography, dry and wet etching techniques, thermal and e-beam metal deposition, oxide and nitride film growth
- *Thin Film Characterization*: Variable angle spectroscopic ellipsometry, static and dynamic surface contact angle, tensiometry
- *Analytical Techniques*: absorbance and fluorescence spectroscopy, cyclic voltammetry, HPLC, GC-MS, FT-IR, NMR, capillary electrophoresis, dynamic light scattering
- *Basic coding and programming*

Publications:

Wagner, K.; Wang, Y.; Regen, S.; Vezenov, D., “Yield Strength of Structurally Similar Langmuir-Blodgett Films Determined by Force Spectroscopy”, *Physical Chemistry Chemical Physics*, submitted.

Wagner, K.; Jagota, A.; Vezenov, D., “Measuring the Interaction Strength of Single-Stranded DNA on Suspended Carbon Nanotubes - a Comparison to 2-D Substrates” *In Preparation*.

Iliafar, S.; **Wagner, K.;** Manohar, S.; Jagota, A.; and Vezenov, D., “Quantifying Interactions Between DNA Oligomers and a Graphite Surface Using Single Molecule Force Spectroscopy”, *J. Phys. Chem C.*, **2012**, 116 (26) 13896-13903.

Wagner, K.; Cheng, P.; Vezenov, D., "Non-contact Method for Calibration of Lateral Forces in Scanning Force Microscopy", *Langmuir* **2011**, 27 (8) 4635-4644.

Gan, Q.; Gao, Y.; **Wagner, K.;** Vezenov, D.; Ding, Y.; Bartoli, F., “Experimental verification of the "rainbow" trapping effect in adiabatic plasmonic gratings" *PNAS* **2011**, 108 (13) 5169-5172.

Wagner, K.; Wang, Y.; Regen, S.; Vezenov, D., “Yield Strength of Structurally Similar Langmuir-Blodgett Films Determined by Friction Force Microscopy“, *Polymer Preprints*, 2008.

Presentations:

Wagner, K.; Iliafar, S.; Jagota, A.; Vezenov, D. (2012, September 21). *Quantifying Interactions between DNA Oligomers and Graphite Using Single Molecule Force Spectroscopy*. Poster Presented at the BPS Regional Network Meeting, Bethlehem, PA.

Wagner, K.; Wang, Y.; Regen, S.; Vezenov, D. (2008, August 19). *Yield Strength of Structurally Similar Langmuir-Blodgett Films Determined by Force Spectroscopy*. Poster Presented at the 236th ACS National Meeting, Philadelphia, PA.

Fellowships & Awards:

-
- College of Arts and Sciences Fellowship (Lehigh University, 2010)
 - Dean’s Fellowship (Lehigh University, 2009)
 - Nicole Reinhart Memorial Scholarship (Kutztown University, 2002)
 - Kutztown Area Chamber of Commerce Scholarship (Kutztown University, 2002)
 - Arrow International Scholarship (Kutztown University, 2002)

Teaching Experience:

- **Physical Chemistry Lecture Teaching Assistant** August 2012-December 2012
Served as a teaching assistant to an upper level undergraduate/graduate physical chemistry lecture. Duties included grading homework, quizzes, and exams, creating answer keys, and assisting students in the course.

- **Physical Chemistry Lab Teaching Assistant** August 2011-May 2012
Instructed a Junior/Senior level physical chemistry lab. Experiments covered material on statistical and error analysis, partial molar volume, and optical rotation measurement of polymer

transitions. Teaching responsibilities included experiment preparation, instrument maintenance, and grading lab reports.

- **General Chemistry Lab Teaching Assistant** August 2006-May 2009
Instructed a Freshman level introductory chemistry lab covering classical experiments on reduction-oxidation chemistry, the ideal gas law, molecular structure, unit conversion and physical properties, and Hess' Law. Laboratory safety was also a major emphasis of learning as this was the first time many students worked with hazardous chemicals. Teaching responsibilities included grading lab assignments and lecture exams, holding regular office hours, and proctoring exams.

Work Experience:

Microscopy Lab Intern Summer 2004 & 2005

Arkema, King of Prussia, PA

I primarily performed atomic force microscopy and scanning electron microscopy imaging on materials such as impact modified plastics, latex solutions, fuel cell membranes, and coated glasses. My job duties included sample preparation, instrument maintenance and calibration, and data processing.

Outreach:

Da Vinci Science Center, Allentown, PA 2011-2012

Helped develop an interactive museum exhibit demonstrating our DNA/Nanotube experiments at a local science museum.